DESIGN AND EVALUATION OF POLYMERIC NANOMATERIALS FOR *IN VITRO* AND *IN VIVO* IMAGING APPLICATIONS

A Thesis
Submitted to the Graduate Faculty
of the
North Dakota State University
of Agriculture and Applied Science

By

Anil Vishvanath Wagh

In Partial Fulfillment of the Requirements
for the Degree of
DOCTOR OF PHILOSOPHY

Major Department:
Pharmaceutical Sciences

June 2013

Fargo, North Dakota

North Dakota State University

Graduate School

Title

Design and Evaluation of Polymeric Nanomaterials for In vitro and In vivo Imaging Applications

By

Anil Wagh

The Supervisory Committee certifies that this ***disquisition*** complies with North Dakota State University's regulations and meets the accepted standards for the degree of

DOCTOR OF PHILOSOPHY

SUPERVISORY COMMITTEE:

Dr. Benedict Law
Chair

Dr. Sanku Mallik

Dr. Estelle Leclerc

Dr. Jayaraman Sivaguru

Approved:

08/30/2013	Dr. Jagdish Singh
Date	Department Chair

ABSTRACT

One of the most versatile and safe material used in medicine is polymer-based nanomaterials. This dissertation describes the use of several formulations of polymeric nanomaterials for *in vitro* and *in vivo* optical imaging applications. In the first phase of this work, the particles assembled from diblock copolymers of poly(D,L-lactic-*co*-glycolic acid) and polyethylene glycol were used as a carrier for diagnostic agents. In chapter 2, the polymeric nanoparticles with a large Stokes shift of >100 nm were employed for *in vivo* imaging. The large Stokes shift was achieved through fluorescence resonance energy transfer (FRET) by encapsulating the donor (1,1'-dioctadecyl-3,3,3',3'-tetramethylindodicarbocyanine) and acceptor (1,1'-dioctadecyl-3,3,3',3'-tetramethylindotricarbocyanine) fluorophores inside a single nanoparticle. These nanoparticles were then systematically explored to optimize the fluorophore loading and the maximum energy transfer efficiency. The animal studies further demonstrated that these nanoparticles could have far-reaching applications for *in vivo* imaging. In chapter 3, we further extended the study by doping the combinations of four different fluorophores, DiO, Dil, DiD, and DiR to synthesize particles that exhibited distinct emission signatures ranging from the visible to near-infrared wavelength region. This work presents first instance of nanoparticles encapsulated with four different energy transfer fluorophores inside a single particle. The optimized multicolor nanoparticles could simultaneously emit fluorescence at three different wavelengths (at 570, 669, and 779 nm) upon a single excitation (at 485 nm). Furthermore, particles with single, double, and triple emissions could be synthesized by changing the combination and doping ratio of the fluorophores. We further demonstrated that this technology could be applied to multicolor and multiplex imaging.

Various physiological mechanisms are responsible for nanomaterial interaction and clearance from the blood circulation. The objective of chapter 4 was to investigate the biocompatibility, pharmacokinetics, and biodistribution of peptide-based nanofiber (NFP). *In vitro* studies suggested that NFP is non-toxic, hemocompatible and only showed a minimum uptake by the isolated macrophages. Upon systemic injection into mice, NFP could be delivered to the tumor in a short period of time and also eliminated rapidly by renal clearance. Overall, our results suggested that NFP is a biocompatible, safe, and effective carrier for tumoral delivery.

ACKNOWLEDGEMENTS

Firstly, I would like to thank my thesis advisor, Dr. Benedict Law. I appreciate that he gave me the valuable opportunity to come to the North Dakota State University and to his lab for my Ph.D studies. I also appreciate that he allowed me to work on diverse projects which I like very much. During all those years in my study and research as a graduate student, I learned a lot from him. He taught me how to become a real scientist and solve the problems. His patience and wisdom impressed me very much. Instead of blaming, he always encouraged and helped me when I was not doing well on the experiments, papers and presentations. I really appreciate his support and advice from my heart. Without him, I could not achieve so much today. Secondly, I would like to express my sincere gratitude to Dr. Estelle Leclerc and Dr. Sanku Mallik, who gave me opportunities to work in collaboration with their laboratory. I also appreciate them for their patience and confidence in me and for so many valuable discussions on the experiments. They not only gave me opportunities to work on collaborative projects but also guided me as thesis committee members. Thirdly, I would like to thank Dr. Jayaram Shivguru from the Department of Chemistry and Biochemistry at North Dakota State University, Fargo, who was kind enough to act as a thesis guide. I would also like to thank Dr. Scott Payne, who helped during my TEM study. Many thanks to Dr. Jagdish Singh, Chair and professor at Department of Pharmaceutical Sciences at North Dakota State University for all guidance and support throughout my graduate studies.

A huge thanks for my wife Rupali and my family for their constant support and encouragement throughout my graduate studies. In addition, thanks to the all the friends including Neha, Rhishi, Venkata, Mayura, Sathish for their support. Many thanks to the North Dakota EPSCoR DDA Program for providing a financial support for my graduate studies.

TABLE OF CONTENTS

LIST OF TABLES

LIST OF FIGURES

Figure Page

LIST OF ABBREVATIONS

PET…….	Positron emission tomography
SPECT……	Single-photon emission computed tomography
MRI……	Magnetic resonance imaging
NADPH……..	Nicotinamide adenine dinucleotide phosphate
ICG…….	Indocyanine green
SNR……	Signal-to-noise ratio
MPS……	Mononuclear phagocytic system
EPR…….	Enhanced permeability and retention
TEOS……..	Tetra orthosilicate
AFP…….	Alpha fetoprotein
PMMA……	Poly(methyl methacrylate)
PEG…….	Polyethylene glycol
PVA……	Polyvinyl alcohol
HCG……	Human chorionic gonadotropin
CCPM…….	Core cross-linked polymeric micelle
CPNPs…….	Calcium phosphate nanoparticles
BHQ……	Black hole quencher
TBET……..	Through bond energy transfer
R6G…….	Rhodamine 6G
PGA…….	Polyglycolic acid
PLA…….	Polylactic acid
DMF……	Dimethylformamide

EDC…….	1-ethyl-3-(3-dimethylaminopropyl) carbodiimide
NHS…….	*N*-hydroxysuccinimide
DIEA……	*N*,*N*-diisopropylethylamine
BSA…….	Bovine serum albumin
MTS…….	(3-(4,5-dimethylthiazol-2-yl)-5-(3-carboxymethoxyphenyl)-2-(4-sulfophenyl)-2H-tetrazolium)
ROI……..	Region of interest
NMR……	Nuclear magnetic resonance
DiO……..	3,3'-dioctadecyloxacarbocyanine
Dil……	1,1'-dioctadecyl-3,3,3',3'-tetramethylindocarbocyanine
RAGE……..	Receptor for advanced glycation endproducts
HER2……...	Human epidermal growth factor receptor 2
FITC…….	Fluorescein isothiocyanate
TRITC…….	Tetramethylrhodamine isothiocyanate
TMR…….	Tetramethylrhodamine
RITC……	Rhodamine B isothiocyanate
Cy…….	Cyanine
RuBPY…….	Tris(bipyridine)ruthenium(II) dichloride
BODIPY……...	Tris(1,10-phenanthroline)ruthenium(II) chloride hydrate
NBD……..	Boron-dipyrromethene (BODIPY), 4-chloro-7-nitrobenzo-2-oxa-1,3-diazol
DiD……...	1,1'-dioctadecyl-3,3,3',3'-tetramethylindodicarbocyanine
DiR……..	1,1'-dioctadecyl-3,3,3',3'-tetramethylindotricarbocyanine
Si-NPs……..	Silica nanoparticles

CPNPs…….	Calcium phosphate nanoparticles
BBB……	Brain blood barrier
AuNC……..	Gold nanocrystal
QD……...	Quantum dot
MNP……	Magnetic Fe_3O_4 nanoparticles
EPR……..	Enhanced permeability and retention
FDA…….	Food and drug administration
RES……..	Reticuloendothelial system
NFP……..	Nanofiber
2D…….	2-dimensional
3D…….	3-dimensional
ASTM……...	American Society for Testing and Materials
SCID…….	Severe combined immunodeficiency
QD……	Quantum dots
MWCT……..	Multi-walled carbon nanotubes
PS……..	Polystyrene nanoparticles
PLGA……	Pegylated poly(D,L-lactic-*co*-glycolic acid) nanoparticles
AU……	Gold nanoparticles
AUC…….	Area under the curve
MRT…….	Mean residence time
$t_{1/2}$…….	Half-life
NIR……...	Near-infrared

CHAPTER 1. INTRODUCTION

1.1. Optical imaging

Optical imaging has emerged as a powerful tool capable of non-invasively detecting and visualizing biological processes at the molecular level [1]. In general, the method utilizes the light of UV-visible and near-infrared (NIR) wavelengths to characterize the optical properties of tissues [2]. The interaction of photons with tissue mainly results in the following phenomenon such as the absorption of light [3], the scattering of light [4], or the generation of fluorescence emission [5]. These optical properties have been exploited individually for the structural and functional characterization of biological tissue for the last five decades [6]. In comparison to other imaging modalities, optical imaging offer several advantages such as 1) avoiding the use of ionizing radiations, 2) use of simple optical instrumentation and thus cost effective, 3) high sensitivity, 4) minimal cell damage, 5) the ease of handling and use, 6) simultaneous identification of multiple biological events [7], and 7) real time monitoring [8]. Furthermore, it can be easily used in complementation with the other imaging modalities such as positron emission tomography (PET) [9], single-photon emission computed tomography (SPECT) [10], and magnetic resonance imaging (MRI) [11, 12]. However, the major limitation of the optical imaging is the penetration depth of light inside the living tissue [13, 14]. Because of the involvement of numbers of absorption and scattering events, the penetration depth inside the tissue is highly dependent on the wavelength of light. The photons of the UV-visible wavelength region (200-650 nm) are strongly absorbed by tissue chromophores, resulting in small penetration depth of few micrometer to millimeters inside the tissue. This allows only superficial assessment of the spectral properties of the tissues. On the other hand, the light of NIR wavelength region (650-900 nm) penetrates deeply inside the tissue because of the reduced tissue

absorption, scattering, and autofluorescence **(Figure 1)** [15]. Therefore, NIR imaging is mostly suitable for *in vivo* imaging applications especially in deep-tissue level.

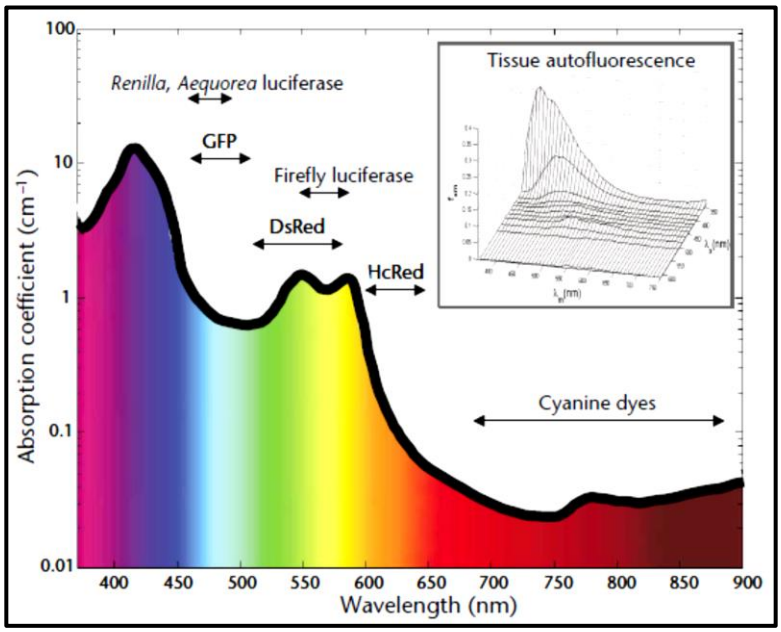

Figure 1. The absorption coefficient of the biological tissue at different wavelengths. The optical properties of different endogenous and exogenous fluorophores. The figure is adapted from reference [13].

1.1.1. Endogenous contrast agents

The light absorption by tissue generally originates from a variety of biological molecules such as hemoglobin, water, melanin, porphyrin, amino acids (tryptophan and tyrosine), proteins (collagen and elastin), and coenzymes (reduced nicotinamide adenine dinucleotide) [16]. Most of endogenous molecules also exhibit a characteristic fluorescence emission which is called tissue autofluorescence. These endogenous fluorophores have been used for the assessment of the metabolic status of biological tissues [16]. In some instances, the changes in the intrinsic fluorescence due to specific morphologic and biochemical alternations can be used as a biomarker for the disease detection. For example, the changes in levels of collagen and nicotinamide adenine dinucleotide phosphate (NAD(P)H) were used for the detection of

epithelial precancerous tissues (dysplastic) in cervix and esophagus [17]. Similarly, the cases of advanced ulcerated squamous cell carcinoma were identified by protoporphyrin, a red fluorescent product formed in the tumor tissue [18, 19]. Although there are a number of successful reports on the use of endogenous fluorophores as a contrast agent **(Table 1)**, their application is mainly limited by their low brightness (determined by the extinction coefficient and quantum yield), high absorption and scattering of the illuminated light by the tissue, and only subtle differences in the spectral properties between the normal and diseased tissue. This lead to the discovery and use of the exogenous contrast agents.

Table 1. Endogenous tissue fluorophores used in medical diagnosis.

Fluorophore	***λmax (nm)***	***Disease Diagnosed***	***Reference***
NAD(P)H and Collagen	340, 380	Dysplasia in cervix and esophagus	[17]
Collagen and Elastin	350, 476	Atherosclerotic plaques	[20]
Collagen	380	Mammary tumor	[21]
Collagen	380	Obesity	[22]
Collagen	390	Malignant tissue	[23]
NADH and Porphyrin	397, 610	Dysplasia in Barrett's esophagus	[24]
Lipofuscin granules	450	Aging	[25, 26]
Collagen, Elastin, and NADH	460	Neoplastic gynecological tissues	[27]
Flavins	500	Malignant tissue	[28]
Protoporphyrin and Porphyrin	610	Advanced ulcerated squamous cell carcinoma	[18, 19]

1.1.2. Exogenous contrast agents

1.1.2.1. Non-specific contrast agents

To address the limitations of the endogenous molecules, numerous types of exogenous optical contrast agents have been developed in the past few years [29]. The exogenous contrast agents principally provide the opportunity of generation of disease specific signal within tissue, thus enabling the display of the physiological and molecular conditions. These agents either

introduce a distinct absorption or fluorescence emission in the tissue and in some cases also help to visualize the changes in the optical properties of the native tissue. The examples of the most commonly used fluorophores are fluorescein [30, 31], indocyanine green [32, 33], cresyl violet [34], isosulfan blue [35], methylene blue [36, 37], and porphyrins [38] **(Table 2)**. These fluorophores possess very unique absorption and emission properties and can be efficiently delivered *via* topical as well as intravenous route because of their extremely low molecular weight (<1 KDa). However, they are non-specific in nature and therefore have tendency to localize in intracellular and extracellular space based on their size and charge distribution.

Table 2. Exogenous contrast agents and their current medical applications.

Fluorophore	***Application***	***Reference***
Indocyanine green	Neurosurgery	[39, 40]
	Coronary bypass angiography	[41, 42]
	Vascular surgery	[43]
	Sentinel lymph node mapping	[44, 45]
	Lymphography	[46]
	Liver surgery and laparoscopy	[47, 48]
	Laparoscopic cholecystectomy	[49]
	Reconstructive microsurgery	[50]
	Muscle perfusion	[51]
	Rheumatoid arthritis	[52]
Methylene blue	Identification of ureter	[53]
	Extra hepatic bile ducts identification	[54]
	Coronary angiography	[55]
	Detection of neuroendocrine tumors	[56]
Fluorescein	Retinal angiography	[57]

Indocyanine green (ICG) is the first fluorophore that is approved by the food and drug administration (FDA) for the human use. ICG is a carbocyanine fluorophore with a characteristic absorption and emission in NIR wavelength region. It is used in ophthalmic angiography [58, 59], hepatic function test [60, 61], and cardiac physiology test [62]. For the ophthalmic angiography, fluorescein with absorption and emission in visible region is a more popular choice, as it is visible without any electronic camera [57]. Recently, ICG was used for a first-in-

human clinical trial for image guided intraoperative sentinel lymph node mapping in breast cancer patients [63]. The large therapeutic index (LD_{50} of 50-80 mg/kg for animal models) of ICG further potentiate its application in the medical diagnosis **(Table 2)** [64]. Methylene blue is another NIR fluorophore used clinically for the imaging of the ureters [53] and bile ducts [54]. Other medical applications of non-specific exogenous contrast agents are illustrated in **Table 2**.

1.1.3. Limitation of non-specific contrast agents

There are some major drawbacks associated with non-specific contrast agents. First is their lack of tissue specificity, which results in high background signal and thus poor signal-to-noise ratio (SNR). Secondly, most of the fluorophores have the tendency to undergo aggregation upon storage [65] and binding to serum proteins in the blood stream [66] owing to their hydrophobic nature. Lastly, exogenous fluorophores are known to undergo photobleaching [67] as well as thermal degradations [68].

1.1.4. Targeted contrast agents

One way to improve the specificity of any contrast agent is by use of targeted ligands. Among all, monoclonal antibodies are the most widely used targeting ligand for achieving the molecular specificity [69]. The fluorophores can be simply attached to antibodies *via* covalent or non-covalent conjugation. Because of the high selectivity and affinity of targeting ligands towards the specific receptors, optical mapping can be done with only low doses (nanomolar) of the imaging agent. This specificity results in high signal-to-noise in target organ. The first report of antibody conjugated fluorophores was demonstrated for the detection of human squamous cell carcinoma in nude mice in 1994 [70] and since then numerous targeted imaging probes have

been developed [29]. However, monoclonal antibodies as a targeting molecule can be detrimental especially from imaging stand point of view because of their long plasma half-life ($t_{1/2}$) and immunogenicity [71]. Furthermore, a large hydrodynamic size of the antibody may also prevent the intratumoral uptake and homogeneous distribution in the tumor. Alternatively, small targeting ligands such as affibodies (small antibody fragments) [72], peptides [73], and aptamers [74] have been used to overcome these shortcomings. Even though the ligand assists in achieving the molecular specificity, the fluorophores are still susceptible to photodegradation owing to their contact with the surrounding environment [75]. Additionally, the maximum number of fluorophores that can be loaded on a single targeting ligand can be limited (1-5 fluorophores per ligand). This is mainly because high loading can have unfavorable effects on the avidity and the biological activity of the ligand [76]. Also increases in the number of fluorophores per ligand may significantly decreases the total fluorescence emission intensity (brightness) due to the self-quenching [77].

1.2. Nanoparticles as an imaging probe

An alternate way to overcome the limitations of the exogenous fluorophores is by doping them into/onto the nanoparticles. According to the U.S. National Nanotechnology Initiative (www.nano.gov), nanomaterials is any material with at least one dimension in the range of approximately 1 to 100 nm. Materials within this nanometer sized range can exhibit unique physicochemical and biological properties that are significantly different from the properties of bulk materials. Importantly, these unique physicochemical properties such as size, shape, surface charge, surface functionality, and composition of nanomaterials play a major role in their interactions with the biological system (nano-bio interface) [78-80]. Depending on the nature of

nano-bio interfaces, the biodistribution, biocompatibility, and toxicity of nanomaterials can be largely affected [81]. One example is the effect of size on the *in vivo* tissue distribution of nanoparticles inside the body [82]. When injected intravenously, the ultra-small nanoparticles (3-5 nm) are predominantly eliminated by the kidney while the larger nanoparticles (>10-20 nm) can be largely retained by the cells of mononuclear phagocytic system (MPS) present in the liver and spleen [83-85]. Depending on the particle size, nanoparticles may undergo the selective vascular escape from the blood stream *via* fenestration (small opening) of endothelial barriers. For instance, in certain disease conditions such as cancer [86], atherosclerosis [87, 88], and rheumatoid arthritis [89], the anatomical and pathophysiological changes results in the formation of discontinuous fenestration of 200-800 nm. This unique tumor vascular phenomenon that allows the selective passage of the nanoparticles is called the enhanced permeability and retention (EPR) effect [90]. These disease specific pathological changes have been extensively studied for nanomaterial mediated delivery of therapeutic and diagnostic molecules [91].

Fluorophore-doped nanoparticles are a new generation of nanomaterial based fluorescent probes that were developed recently for *in vitro* and *in vivo* applications [92, 93]. Compared to other nanoparticle based contrast agents, these particles can be generated simply by doping organic/inorganic fluorophores into/onto optical inert matrix. The photophysical behavior of fluorophores is highly dependent on their local distribution inside the particles [94, 95]. Because of the entrapment of hundreds to thousands of fluorophores inside a single particle, high brighter optical signal is generated as compared to a single fluorophore. Moreover, by controlling the loading density (number of fluorophores per particle), the brightness (product of quantum yield and extinction coefficient) can be enhanced to make ultrasensitive nanoparticles for imaging [96, 97]. The encapsulation of fluorophores into nanoparticles also enhances the photo- and thermo-

stability as well as reduces their interactions with the outside environment thorough matrix shielding protection [98].

Among all, silica nanoparticles are the most commonly used platform because of their straightforward synthesis and availability of rich surface chemistry [99, 100]. Most importantly, silica is a chemically inert and optical transparent material which makes it as an excellent matrix for encapsulation of the fluorophores. Silica nanoparticles are generally synthesized by hydrolysis followed by condensation polymerization reaction with tetra orthosilicate (TEOS) catalyzed in presence of liquid ammonia in following two ways [101]. The first method is called sol-gel method or Stober synthesis in which ammonia induces hydrolysis of TEOS in presence of water and ethanol. The second method is microemulsification, in which the polymerization reaction takes place in hydrophilic core of reverse micelles (W/O emulsion). Size of nanoparticles can be controlled by monitoring the reaction parameters such as ammonia concentration or water to surfactant ratio. The fluorophores can be incorporated into silica nanoparticles *via* ionic interaction [102], entrapment [103, 104], or covalent conjugation [105, 106]. For example, positively charged Tris(bipyridine)ruthenium(II) dichloride (RuBPY) molecules were successfully entrapped inside negatively charged silica particles by electrostatic attraction during the microemulsification method [107]. These particles were subsequently used for studying the *in vivo* biodistribution and urinary excretion by optical imaging. In another study, dual-fluorophores doped silica nanoparticles were reported as a theranostic platform, in which an optical contrast agent i.e. IR-780 was covalently conjugated within the silica framework and a photo-thermal agent i.e. Si-Naphthalocyanine was physically encapsulated inside the cylindrical pores [108]. Likewise, numerous types of organic/inorganic fluorophores have been successfully doped into the silica nanoparticles (Table 3). Fluorescent silica

nanoparticles modified with targeting ligands have been applied in many areas of bioanalysis. For instance, RuBPY-doped Si-NPs modified with mouse anti-human CD 10 antibody were used for the identification of human leukemia cells [109]. Similarly, fluorescence anisotropy based immunoagglutination assay for the recognition and detection of alpha fetoprotein (AFP), a biomarker of hepatocellular carcinoma and germ cell tumors [110], has been developed by conjugating anti-AFP antibody to methylene blue doped Si-NPs [111]. Additionally, Si-NPs have been also adapted for cellular imaging, multiplexing analysis, DNA hybridization, and nucleic acid analysis [99, 100]. Although different types of targets such as proteins, cells, and bacteria have been successfully identified by silica nanoparticles at *in vitro* and *ex vivo* levels, their use for *in vivo* imaging can be limited by their low aqueous solubility and that they can possibly trigger local inflammation by formation of reactive oxygen species and free radicals [112, 113].

Polymer based nanoparticles is another type of optically inert material that is relatively non-toxic and biodegradable [114, 115]. In general, the fluorophores diffuse into the polymeric matrix and get physically entrapped inside the core through hydrophobic interactions. Beside this approach, fluorophores can be doped inside nanoparticles by ionic interactions [116] and covalent bonding [117]. Depending on the polymer of interest, the nanoparticles can be synthesized by following three methods: 1) emulsion polymerization, 2) nanoprecipitation, and 3) emulsification. The most commonly used polymer matrices are polystyrene [118], poly(methyl methacrylate) (PMMA) [95], and poly(D,L-lactic-*co*-glycolic acid) (PLGA) [119]. These polymeric matrices are extremely hydrophobic in nature and therefore the resulting nanoparticles tend to aggregate through non-covalent interactions. The particles can be stabilized by using water soluble stabilizer such as polyethylene glycol (PEG), polyvinyl alcohol (PVA),

and polyamines [120, 121]. The stabilizer may be added at the time of synthesis or during a coating step after the particle formation.

Fluorophore-doped polymeric nanoparticles serve as excellent optical probe for various biological applications **(Table 3)**. For example, fluorescein doped PMMA nanoparticles were used as a fluorescent nanosensor in a fluoroimmunoassay for the detection of human chorionic gonadotropin (HCG) [122]. In another study, a NIR optical imaging probe based on core cross-linked polymeric micelle (CCPM) was developed by using Cy7 fluorophores and amine-terminated amphiphilic block co-polymer [123]. Approximately 21 molecules of Cy7 fluorophores were successfully entrapped in a single particle. After intravenous injection, optical imaging showed a gradual increase in tumor uptake (up to 120 h) suggesting potential of CCPMs for detection of solid tumors. Similarly, *in vitro* and *in vivo* NIR imaging of breast cancer cells was also demonstrated using folic acid conjugated PLGA-lipid hybrid nanoparticles doped with indocyanine green [119]. Despite of the successful imaging applications and excellent safety profile, polymeric nanoparticles are prone to leakage in blood circulation [98]. Various approaches such as covalent conjugation of fluorophores to nanoparticles matrix [117], transforming the solubility and size of the fluorophores, creating the electrostatic attraction between the matrix and fluorophores [116] have been attempted to overcome these shortcomings. These methods are helpful to certain extent but also possess some inherent limitations.

Table 3. Fluorophore-doped nanoparticles.

Nanomaterial	*Fluorophore*	*Mode of doping*	*Reference*
Silica Nanoparticles	FITC	Covalent	[124-126]
	TRITC	Covalent	[127]
	TMR	Electrostatic	[128]
	Rhodamine 6G	Entrapment	[129]
	RITC	Covalent	[130]
	Rhodamine B	Covalent	[106]
	Dansyl chloride	Covalent	[94]
	Methylene blue	Entrapment	[131]
	RuBPY	Entrapment	[96, 107]
	NIR-1 and NIR-2	Covalent	[97]
	Indocyanine green	Electrostatic	[132]
	DY776	Covalent	[133]
	Cy5	Covalent	[134]
	$Ru(Phen)_3Cl_2$	Entrapment	[135]
Iron oxide NPs	Cy5.5	Covalent	[136]
	FITC and Cy5.5	Covalent	[137]
Polymeric NPs	Sulforhodamine and fluorescein	Cross-linking	[138]
	Alexa 488	Cross-linking	[139]
	Indocyanine green	Cross-linking	[98]
	Indocyanine green	Entrapment	[140]
	Cy7	Entrapment	[123]
	RuBPY	Entrapment & Electrostatic	[95]
	Sulforhodamine	Entrapment	[141]
	RuBPY, Fluorescein, Rhodamine 6G, Rhodamine B	Entrapment & Electrostatic	[116]
	BODIPY	Entrapment	[118]
	Indocyanine green	Entrapment	[119]
	RITC and NBD	Entrapment	[142]
	Fluorescein	Entrapment	[122]
	Cy5	Covalent	[117]
Hyaluronic acid NPs	Indocyanine green	Covalent	[143]
CPNPs	Cy3	Entrapment	[144, 145]
	Indocyanine green	Entrapment	[146, 147]
Lipid NPs	Porphyrin	Entrapment	[148]
	Indocyanine green	Entrapment	[149]
	DiD and DiR	Entrapment	[150]

Abbreviations: Fluorescein isothiocyanate (FITC), tetramethylrhodamine isothiocyanate (TRITC), tetramethylrhodamine (TMR), rhodamine B isothiocyanate (RITC), cyanine (Cy), Tris(bipyridine)ruthenium(II) dichloride (RuBPY), Tris(1,10-phenanthroline)ruthenium(II) chloride hydrate ($Ru(Phen)_3Cl_2$), boron-dipyrromethene (BODIPY), 4-chloro-7-nitrobenzo-2-oxa-1,3-diazol (NBD), 1,1'-dioctadecyl-3,3,3',3'-tetramethylindodicarbocyanine (DiD), 1,1'-dioctadecyl-3,3,3',3'-tetramethylindotricarbocyanine (DiR), silica nanoparticles (Si-NPs), calcium phosphate nanoparticles (CPNPs)

Recently, calcium phosphate nanoparticles (CPNPs) were identified as a novel carrier for drug delivery and bioimaging [146, 151, 152]. Because of their ubiquitous presence in the form of amorphous calcium phosphate and crystalline hydroxyapatite inside the body, CPNPs are relatively non-toxic, biodegradable, and elicit low immune response [153]. The first work of CPNPs as carrier for contrast agent was recently reported in which the NIR fluorophore i.e indocyanine green was encapsulated into nanoparticles by double reverse microemulsion approach [146]. Unlike the other nanoparticles, monomeric state of fluorophores was retained after encapsulation inside CP matrix. When injected in animals, preliminary results verified the capacity of CPNPs for deep tissue imaging applications. The same nanoparticles were further targeted by using anti-CD71 antibody and gastrin peptide for imaging of breast and pancreatic cancer, respectively [147]. Apart from these, various other nanomaterials have been used as carriers for contrast agents. All the other examples of fluorophore-doped nanomaterials are summarized in **Table 3**.

1.2.1. Poly(D,L-lactic-*co*-glycolic acid) based nanoparticles as an optical inert matrix

Poly(D,L-lactic-*co*-glycolic acid) (PLGA) is an aliphatic copolymer consisting of repeating units of lactic and glycolic acid attached by ester linkages (**Figure 2A**). These copolymers are generally synthesized by ring-opening copolymerization of cyclic lactides and glycolides in presence of an appropriate catalyst such as tin(II) 2-ethylhexanoate [154], tin(II) alkoxides [155], or aluminum isopropoxide [156]. The copolymer can also be synthesized by direct polycondensation of lactic and glycolic acid [157]. However, this method is only suitable for synthesis of low molecular weight copolymers because of the inherent limitation such as the hydrolysis of growing polymer chain in presence of liberated water from the reaction mixture. In

general, during polymerization the monomer units are linked together by ester linkage to yield a linear, aliphatic polyester product (**Figure 2A**). The physical and rheological properties of the resulting copolymer largely depend on the ratio of lactic acid/glycolic acid and the stereochemistry (D- and/or L-lactic acid) of monomers. Polyglycolic acid (PGA) is a highly crystalline material with a melting temperature of 225-230°C. On the other hand, polylactic acid (PLA) is a semi-amorphous material with a melting temperature of 173-178°C. Unlike glycolide, lactic acid exists in two distinct optically active forms i.e. D-lactide and L-lactide due to the presence of a chiral center. By precisely controlling the ratio of lactide to glycolide, the physiochemical properties of PLGA copolymer can be fine-tuned to virtually mold into any shape and size that has the capacity to encapsulate molecules of any size. The examples of the PLGA derived materials include nanofibers, nano-and microparticles, implants, sutures and many more [158].

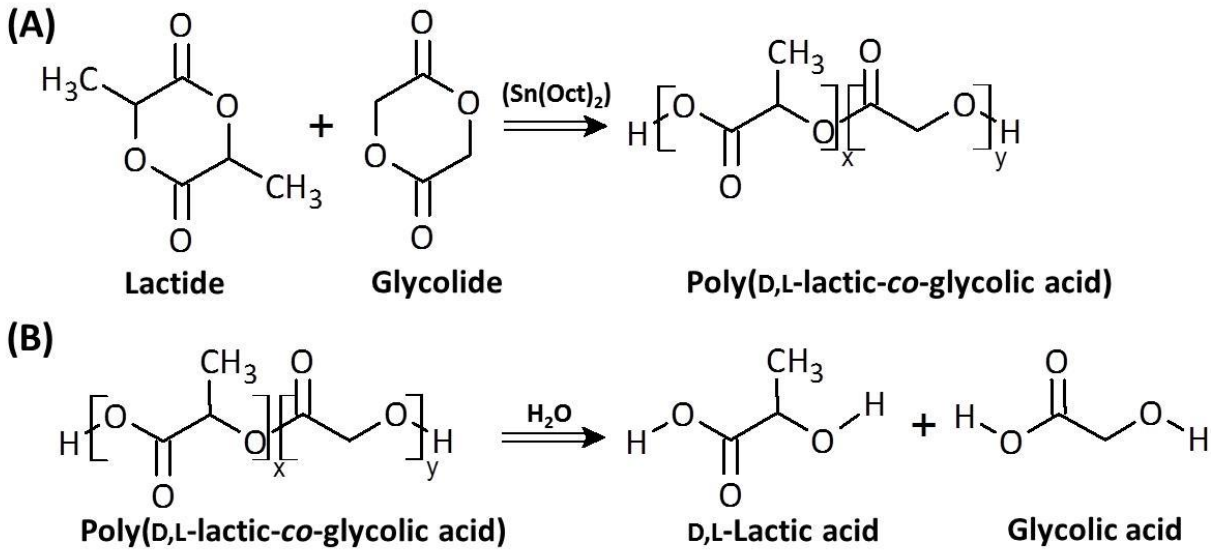

Figure 2. Schematic representation of synthesis and hydrolysis of PLGA copolymers. (A) Synthesis of PLGA copolymer by ring-opening copolymerization in presence of stannous octoate. (B) Hydrolysis of PLGA copolymer.

One important characteristic of PLGA copolymers is their biodegradation and biocompatibility. Under physiological conditions, the copolymers can undergo hydrolysis (in presence of water) owing to the presence of intrinsically sensitive ester linkages. The hydrolysis results in non-toxic components (lactic and glycolic acid) **(Figure 2B)**, which can be easily eliminated from the body in the form of water and carbon dioxide *via* the Krebs cycle. The rate of degradation may vary from copolymer to copolymer depending on the monomer composition. For example, PLGA copolymers containing high lactide content degrade more slowly as compared to the one with high glycolide. This is mainly because the presence of a methyl side group in lactic acid imparts a more hydrophobic character and therefore reduces the absorption of water and subsequent degradation. In addition, the hydrolytic degradation behavior of copolymers also depends on their chemical composition, mechanism of hydrolysis (noncatalytic, autocatalytic, enzymatic), additive (such as surfactants), morphology, dimensions, porosity, glass transition temperature, and molecular weight distribution. This composition dependent degradation of PLGA copolymers have been explored in field of drug delivery.

PLGA nanoparticles have gained much interest because of their ability to carry a wide variety of molecules ranging from small molecules to macromolecules **(Table 4)** [158, 159]. However, PLGA derived particles are extremely hydrophobic and when injected intravenously undergo rapid clearance from the circulation with accumulation in major excretory organs such as liver and spleen. To overcome these limitations and also to incorporate more flexibility, various types of block copolymers of PLGA and polyethylene glycol (PEG) such as PLGA-PEG, PLGA-PEG-PLGA, and PEG-PLGA-PEG have been developed [160-162]. The physiochemical properties of these block copolymers vastly differ from each other and thus result in different kinds of nanostructures. For instance, PLGA-PEG diblock copolymers undergo self-assembly in

aqueous environment to form a core-shell type of structures consisting of hydrophobic PLGA core surrounded by a layer of hydrophilic PEG. The PEG coating is known to minimize the aggregation upon storage as well as to help to improve the circulation time *in vivo* [163]. Additionally, the sheath of hydrophilic PEG also exposes multiple terminal functional groups at the surface for bioconjugation of the targeting ligand [164].

Table 4. Examples of PLGA nanoparticles used as a nanocarrier.

	Therapeutic/imaging agent	***Disease treated/diagnosed***	***Targeting ligand***	***Reference***
Therapeutic	Cisplatin	Prostate cancer	Aptamer	[160, 161]
	Doxorubicin	Breast cancer	N/A	[165]
	Docetaxel	Prostate cancer	Aptamer	[166]
	Lonidamine	Cancer	Peptide	[167]
	α-tocopheryl succinate	Cancer	Peptide	[167]
	Curcumin	Alzheimer's disease	Peptide	[167]
	2,4-dinitrophenol	Obesity	Peptide	[167]
	Docetaxel and cisplatin	Prostate cancer	Aptamer	[168]
	Camptothecin	Colorectal cancer	Antibody	[169]
	Doxorubicin and combretastatin-A4	Melanoma and lung cancer	N/A	[170]
	(-) Epigallocatechin 3-gallate	Prostate cancer	Small molecule	[171]
	Loperamide and Rhodamine-123	BBB, Analgesia	Peptide	[172]
Diagnostic	Indocyanine green	N/A	N/A	[98]
	Indocyanine green	Breast cancer	Folic acid	[119]
	Alexa 488	Inflammation	Peptide	[173]
	AuNC and QD-620	Macrophage labeling	N/A	[174]
Theranostics	MNP and Doxorubicin	Lung cancer	N/A	[175]
	MNP and Doxorubicin	Breast cancer	Herceptin	[176]

Abbreviations: Brain blood barrier (BBB), gold nanocrystal (AuNC), quantum dot (QD), magnetic Fe_3O_4 nanoparticles (MNP).

A wide variety of therapeutic and/or diagnostic agents can be loaded into polymeric nanoparticles by following approaches: 1) covalent conjugation with the polymer backbone, 2)

direct adsorption on the particle surface, and 3) entrapment inside the core of the particle during self-assembly. These agents can be used alone or in combination with each other. The choice of technique mainly depends on the physiochemical properties of the molecules of interest, type of copolymers, and desired characteristics of synthesized particles.

Unlike diblock copolymer, triblock copolymers such as PLGA-PEG-PLGA or PEG-PLGA-PEG are water soluble at lower temperature (<20°C) and undergo phase transformation to form a semi-solid hydrogel at body temperature (37°C) [162, 177]. This is mainly due to the involvement of strong hydrophobic interactions and hydrogen bonding between the copolymers. At lower temperature, the hydrogen bonding between the water and the PEG molecules dominate, thus resulting in the dissolution of polymer in water. As the temperature increases, the hydrophobic interactions between the PLGA segments of copolymer become dominant and the hydrogen bonding gets weaker leading to phase transformation from solution to gel. These temperature sensitive polymers can be used for various biomedical applications including drug delivery and tissue engineering.

1.2.1.1. Fabrication of polymeric nanoparticles

A number of top-down approaches are available for the preparation of polymeric nanoparticles [178]. Most of these methods involves the self-assembly of block polymers having two distinct polymeric chains with different solubility. The most common method for the synthesis of nanoparticles is single-emulsification/solvent evaporation technique (O/W) [179]. In this method, PLGA and the drug of interest are dissolved in water immiscible organic solvent and then emulsified in a large volume of water in the presence of emulsifier such as polyvinyl alcohol (PVA). The organic phase is then extracted or evaporated under low pressure to yield

solid nanoparticles. The size of particles can be controlled by adjusting the process parameters such as oil to water phase ratio, concentration of emulsifier, rate of stirring, and sonication time. This method is mainly used for the encapsulation of hydrophobic molecules. A modified method called double or multiple emulsification method (O/W/O) has also been developed for encapsulation of hydrophilic molecules. However, despite of widespread use of the emulsification methods, there are some limitations associated with these methods. The first drawback is the instability of encapsulated molecules especially proteins and peptides due to the high shear speed or sonication to create a stable emulsion. Secondly, the emulsifiers such as PVA are known to show concentration dependent toxicity including lysis of red blood cells. Lastly, the complete removal of organic solvent is difficult and thus also results in added toxicity.

Alternatively, nanoparticles can be synthesized by nanoprecipitation or solvent displacement method [164]. In this method, the drug of interest and copolymer are first dissolved in water-miscible organic solvents such as DMF, acetone, or acetonitrile and then this organic phase is added to the aqueous phase. The surfactant may be added to the aqueous phase. Due to the solubility differences of PLGA (lipophilic) and PEG (hydrophilic) in aqueous and organic phases, a phase separated structure is formed. PLGA is soluble in organic solvent but not in aqueous phase. On the other hand, being hydrophilic, PEG is soluble in water but not in organic solvent. During the self-assembly, PLGA aggregate in aqueous environment to form the core and PEG migrates from the inner core to surface toward the core-water interface. Upon solvent evaporation, the core solidifies to form tiny particles. In addition to the conventional methods, new approaches have been used for the synthesis of polymeric nanoparticles. These include eletro-spraying, premix membrane emulsification, aerosol flow reactor method, and supercritical

technology [91]. Recently, a more advanced technique that uses a microfabricated device with build-in microscale fluidic channels has been also reported for the fabrication of polymeric nanoparticles [180]. There reported devices have shown a dramatic improvement in controlling the physiochemical properties (such as size, surface composition, drug loading) of the nanoparticles over the bulk synthesis methods. As a result, these microfluidics systems have the capacity to synthesize the nanoparticles in a well-controlled, reproducible and high throughput manner [181].

1.2.2. Limitations of single fluorophore-doped nanoparticles

Also, a variety of nanoparticles encapsulated with near-infrared fluorophores have been developed for *in vivo* optical imaging **(Table 3)**. Unfortunately, the encapsulated fluorophores have the disadvantage that their Stokes shift (the difference between the absorption and emission λmax) is smaller than 25 nm and therefore they exhibit a high background fluorescence while imaging. Additionally, fluorophores with a small Stokes shift also prone to self-quenching tendency and thus lead to high level of scattered light measurement error. All of these can result in dramatic decrease in signal-to-noise and thus insufficient resolution at the target sites.

1.3. Strategies to improve the signal-to-noise ratio (SNR)

One approach to improve the resolution at the target site is by improving the Stokes shift of encapsulated fluorophores. Foster resonance energy transfer (FRET) is a simple way to elicit a large Stokes shift by using a combination of two different fluorophore molecules. A typical FRET-based contrast agent consists of a donor fluorophore which upon excitation non-radiantly transfers its energy to another nearby molecule (an acceptor) *via* long dipole-dipole interactions.

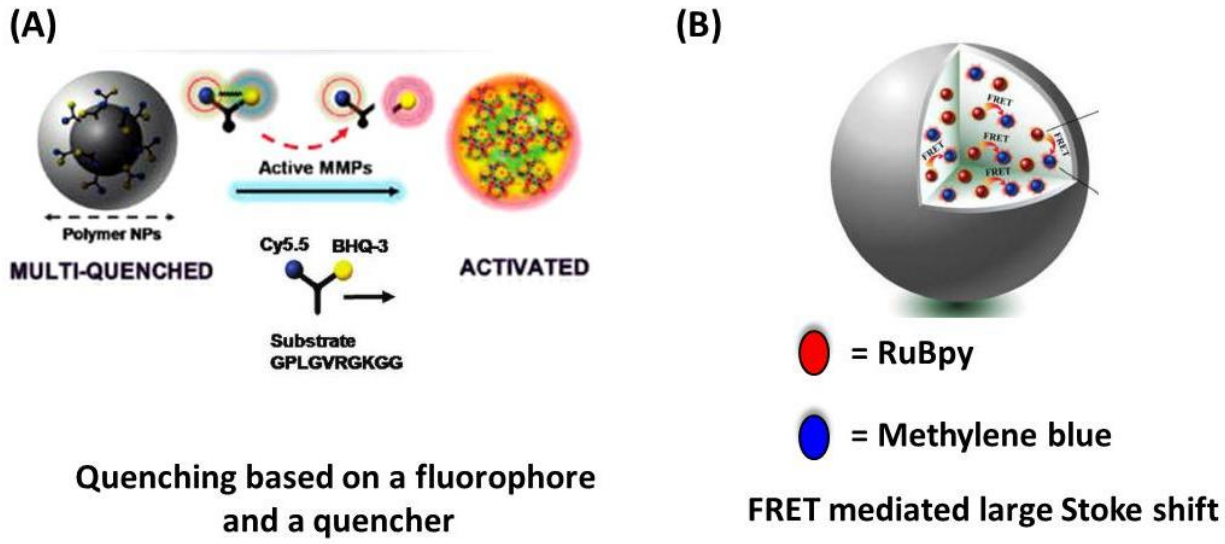

Figure 3. Design of FRET-based contrast agent for *in vivo* imaging applications. (A) Protease activatable polymeric nanoparticles with in-build quenching by using combination of Cy5.5 fluorophore and black hole quencher. The figure is adapted from reference [182]. (B) A FRET mediated large Stokes shifting near-infrared fluorescent silica nanoparticles incorporating a FRET pair (RuBpy and Methylene blue) for *in vivo* imaging The figure is adapted from the reference [183].

Depending on the type of the acceptor molecules, the transfer of energy results in either quenching of fluorescence (optically silent) **(Figure 3A)** or emission of fluorescence at longer wavelength region (large Stokes shift) **(Figure 3B)**. As the transfer of energy is not mediated by actual emission of photons, the phenomenon is termed resonance energy transfer. When both donor and acceptor molecules are fluorescent, the term fluorescence resonance energy transfer is commonly used in scientific literature. The rate of energy transfer mainly depends upon 1) the percentage overlap between the donor emission and the acceptor absorption spectrum, 2) the quantum yield of the donor, 3) the distance between the donor and acceptor molecule, and 4) the relative orientation of transition dipoles.

1.3.1. Basic principles of FRET

The concept and theoretical basis of resonance energy transfer was first developed by a German scientist, Theodor Foster. According to the Foster theory, energy transfer will takes place when an excited fluorophores with an oscillating dipole comes in proximity of another molecule with similar resonance frequency **(Figure 4)**. In contrast to the radiative mechanisms, both structural and positional information regarding the specific donor-acceptor pair can be obtained using the resonance energy transfer.

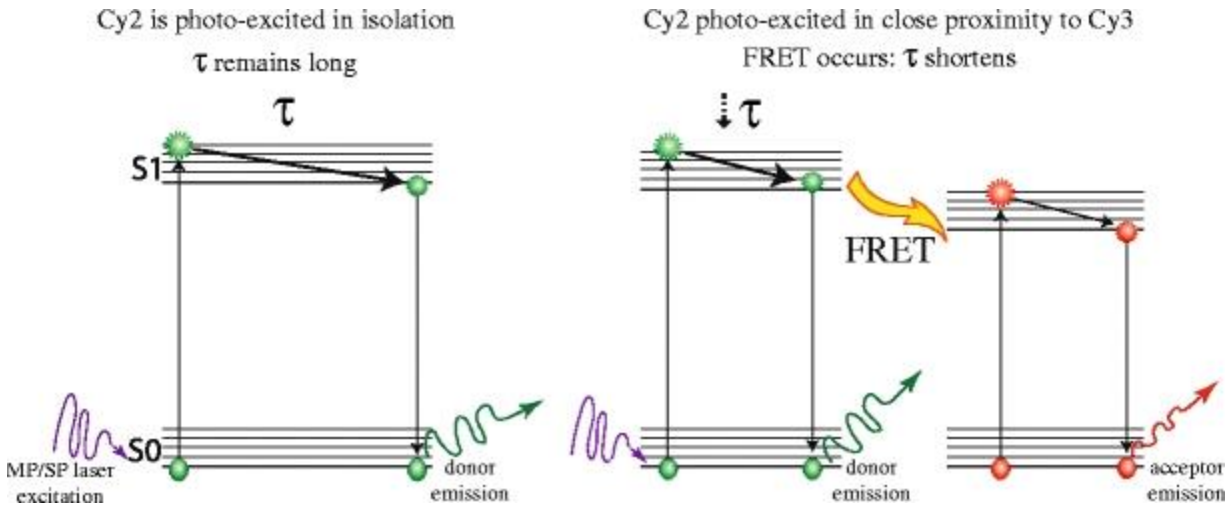

Figure 4. Jablonski diagram of Foster resonance energy transfer. The figure is adopted from the reference [184].

According to the Foster theory, the FRET efficiency (E_{FRET}) is proportional to the inverse sixth power of the distance between the donor and the acceptor (r).

$$E_{FRET} = \frac{1}{[1+\left(\frac{r}{R_o}\right)^6]} \quad \text{..... (1)}$$

Where, R_o is the Foster distance where the FRET efficiency is 50% for a given FRET pair.

$$Ro = [2.8 \times 10^{17} \times k^2 \times Q_D \times \varepsilon_A \times J(\lambda)]^{\frac{1}{6}} \quad \text{..... (2)}$$

Where, k^2 (kappa squared) is the orientation factor between the dipoles of two fluorophores. Q_D is the quantum yield of the donor, ε_A is the extinction coefficient of the acceptor in $Mol^{-1}cm^{-1}$, and $J(\lambda)$ is the spectral overlap integral between the normalized emission spectrum of the donor ($F_D(\lambda)$) and absorption spectrum of the acceptor ($E_A(\lambda)$).

$$J(\lambda) = \int F_D(\lambda) \times E_A(\lambda) \times \lambda^4 d\lambda \quad \text{..... (3)}$$

1.3.2. Applications of FRET

Because of the distance dependent energy transfer, FRET has become an important tool for investigating a variety of biological phenomena that produce changes in molecular proximity. For example, a sensor can be genetically encoded with two fluorescent protein variants for monitoring intracellular Ca^+ activity [185, 186] and apoptosis [187, 188]. Organic donor and acceptor molecules can also be cooperated as a FRET pair for sensing disease-associated analytes such as glucose [189], zinc [190], lysozymes [191], and cholera toxin [192]. Recently, FRET biosensors have been explored for cancer detection and evaluation of drug efficacy [193]. Beside these applications, FRET has been used to overcome the undesirable photophysical properties such as small Stokes shifts (typically less than 25 nm) of exogenous fluorophores.

1.3.3. Activatable imaging probes

One of the approaches to improve the detection sensitivity *in vivo* is by using the activatable imaging probes. These imaging probes are optically silent in native state, however become fluorescent when activated by different stimulus such as enzymes [169], temperature [194], sugar [195], and lysosomal degradation [196]. Among all, the enzyme activatable probes

are the most common, because of the significant differences in the expression level of proteolytic enzymes in normal and pathological conditions such as cancer, atherosclerosis, inflammation, vascular diseases, and Alzheimer's disease as well as in infectious diseases such as AIDS, Ebola, and malaria [197]. In general, the enzyme activatable probes consist of a donor fluorophore, an acceptor (quencher), and an enzyme specific cleavable peptide sequence. The donor and acceptor are linked in such a way that their close proximity (2-10 nm) results in energy transfer. To achieve significant changes in fluorescence signal, an efficient quencher molecule is utilized as an efficient quencher to the donor fluorescence. This approach offers the advantage of high quenching, but at the same time requires much complicated synthetic procedures. The simplest design of these probes connects a donor fluorophore and a quencher by using protease cleavable spacer. For example, a dark quenched fluorogenic probe was synthesized by conjugating Cy5.5 molecule and a black hole quencher (BHQ-3) at the terminal ends of a short peptide sequence (GPLGMRGLGK) [198]. Due to the close proximity of Cy5.5 and BHQ-3, the probe was optical silent in its native state. However, upon cleavage of the enzyme cleavable substrate in the core peptide by MMP-13, the probe became highly fluorescent owing to the release of the BHQ-3. This fluorogenic probe was used for the detection of MMP-13 under *in vitro* condition as well as in osteoarthritis induced rat model. In another study, polymeric nanoparticle based activable near-infrared nanosenor consisting of Cy5.5 and BHQ-3 have been developed for determination of protease activity *in vivo* [182].

1.3.4. Fluorescent probe based on FRET mediated large Stoke shift

Another approach to improve the resolution at the target site is by reducing the fraction of excitation light and scattered light in the emission window. This can be easily achieved by

synthesizing a fluorescent probe with a large Stokes shift. Inorganic fluorescent nanocrystals such as quantum dots (QDs) are the fluorescent probes with extremely large Stokes shift of more than 200 nm [199]. They are known to be more sensitive (brighter) and less susceptible to photo-degradation than organic fluorophores. However, their unsure long-term toxicities hinder their future application in the clinical settings [200]. Therefore, various alternative strategies have been developed to synthesize organic fluorophores with large Stokes shift. FRET is the most commonly used strategy to impart a large Stokes shift between the excitation and emission maxima. Two different designs mainly prevail in this category. The first design consists in energy transfer cassettes in which the donor and the acceptor molecules are covalently linked together. Another approach consist in doping two or more fluorophores inside the nanoparticle to favor the energy transfer.

1.3.4.1. Energy transfer cassettes

Energy transfer cassettes mainly consist of a FRET donor and an acceptor molecules covalently linked together using an appropriate spacer molecule [201]. The mode of energy transfer is highly dependent on the type of the linker molecule. The fluorophores are linked together by a non-conjugated spacer **(Figure 5A)** and the energy transfer mainly occurs through space *via* non-radiative decay pathway (like the traditional FRET). These energy transfer cassettes result in a pseudo-Stokes shift which is larger than the respective Stokes shifts of either donor or acceptor fluorophores alone. However, they are still limited by the requirement that emission spectrum of the donor must overlap the absorption spectrum of the acceptor. Alternatively, the fluorophores can be connected together by electronically conjugated linkers **(Figure 5B)**, where the energy transfer primarily takes place through the bond and to some

extent through space also. This mode of energy transfer is called a through bond energy transfer (TBET). Unlike through space energy transfer, TBET is not constrained by the requirement of the spectral overlap between the fluorophores and therefore does not necessarily involve loss of sensitivity at high resolutions. Regardless of the mode involved in energy transfer, the main advantage of these cassettes is their stability against photodestruction. This is mainly because the energy transfer rates are much faster than intersystem crossing and thus reduce photo-bleaching by avoiding the population of highly reactive triplet state of the fluorophore.

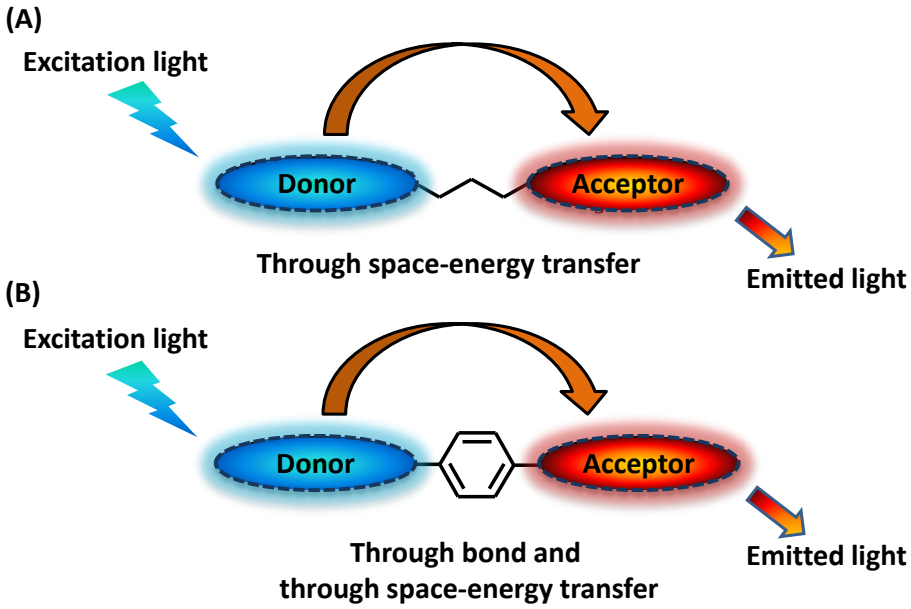

Figure 5. Energy transfer mechanisms in bichromophoric cassettes.

Despite of their distinct advantages over a single fluorophore, widespread applications of the energy transfer cassettes are mainly restricted because of their limited aqueous solubility. The compatibility of cassettes with aqueous media can be improved by introduction of a water soluble moiety. However, this approach is very challenging as very small amount of fluorescent impurities in the purification step may impair the imaging experiment data. Furthermore, the

presence of water solubilizing groups may also result in a decrease in the fluorescence intensity by assisting the non-radiative decay process facilitated by solvation sphere rearrangement in excited state. All these limitations can be mitigated by encapsulating the energy transfer cassettes inside the water soluble nanomaterials. For example, the energy transfer cassettes based on a BODIPY as a donor molecule and a cyanine as an acceptor molecule were successfully encapsulated in calcium phosphate/silicate nanoparticles (22 nm) using double reverse microemulsion method [202]. These particles were water-dispersible and further used for labeling of different organelles inside the cells [202, 203].

1.3.4.2. Multiple fluorophores-doped nanoparticles

An alternative approach to achieve a large Stokes shift is by encapsulating two or more fluorophores inside a single micro/nano-particle [204, 205]. This is designed to maximize the energy transfer among the fluorophores such that maximum emission arises from the fluorophores with lowest excited state energy level in the sphere. Unlike the bichromophoric cassettes in which the fluorophores are conjugated using covalent bond, these nanoparticles are designed using a simple approach by creating high local concentration of the fluorophores to facilitate the energy transfer. This approach is relatively easy and straight forward as no covalent conjugation among the fluorophores is required. In general, the fluorophores are non-covalently entrapped inside the protective matrix. In some cases, covalent conjugation of the fluorophores to protective matrix can be used as an alternative method [205]. The advantage of the covalent approach is that it allows precise control of fluorophore loading and also that the fluorophores are less prone to leakage from the matrix. The energy transfer in multiple-fluorophores doped nanoparticles is mainly facilitated by entrapment of hundreds to thousands of fluorophore

molecules in a small space. As the energy transfer largely depends on the distance between the two fluorophores, the total concentration inside the particles is the key factor. However, when two identical fluorescent molecules comes in close proximity, their fluorescence emission is quenched by intermolecular interactions. Therefore a balance between the level of energy transfer and fluorescence quenching should be optimized based on the intended application of particles. Similarly to single fluorophore-doped nanoparticles, a wide range of organic and inorganic energy transfer fluorophores can be entrapped inside the inert matrix.

Silica nanoparticles are the most extensively studied in this category. An approach has been developed for simultaneous encapsulation of two inorganic fluorophores, Tris(2,2‘-bipyridyl)osmium(II)bis(hexafluorophosphate) (OsBpy) and Tris(2,2‘-bipyridyl)dichlororuthenium(II)hexahydrate (RuBpy) [204]. These fluorophores act as a FRET pair because of their broad overlapping excitation spectrum and the distinct emission maxima. By controlling the ratio and concentration of these two fluorophores, the efficiency of energy transfer can be fine-tuned. Subsequently, these two fluorophores-doped nanoparticles can be used for parallel and high-throughput screening of biomolecules. In another study, two hydrophilic fluorophores, RuBpy and methylene blue (MB), were encapsulated as the model donor-acceptor pair in the silica nanoparticles [183]. It was observed that the resulting near-infrared fluorescent silica nanoparticles possessed strong fluorescence with a large Stokes shift of >200 nm and thus, it can effectively helped to increase the discrimination of fluorescence signal in the region of interest (ROI) over the background signals. Apart from these studies, based on the theoretical modeling, it has been proposed that using silica nanoparticles codoped with Cy3 and Cy5 molecules at a controllable ratio, one can achieve a high resolution in far-field fluorescence imaging [206].

Polystyrene microspheres is another type of inert matrix that has been employed for the encapsulation of fluorophores. The well-known example of multiple fluorophores-doped polystyrene nanoparticles is TransFluoSpheres® (http://www.invitrogen.com). TransFluoSpheres are commercially available fluorescent particles which incorporate a series of two or more proprietary fluorophores that are carefully chosen to allow excited-state energy transfer between the fluorophores, thus producing particles with extremely large Stokes shift. The proprietary fluorophores were optimally loaded to ensure that the excitation energy is efficiently transferred from fluorophore to fluorophore so that essentially only the longest wavelength fluorophore exhibit the maximum fluorescence. These fluorescent tiny particles have been successfully used in a wide variety of experimental and diagnostic applications such as detecting cell-surface antigens [207], tracing neurons [208], and studying phagocytosis [209]. Recently, polystyrene microspheres with a large Stokes shift of 180 nm have also been reported [210]. These particles were synthesized by using two julolidine fluorophores through solvent evaporation technology. Because of deep embedment of the fluorophore molecules, the particles showed better stability than traditional surface labelled microsphere.

As the fluorescent nanoparticles are discriminated on the basis of colors, they are extremely useful in diagnostic field especially for parallel and high-throughput screening in the multiplex format [211, 212]. Large number of nanoparticles can be generated based on the different amounts of one or more fluorophores emitting in multiple different wavelengths. However, the number of colors generated by combination of single or two fluorophores can be limited, which restricts their use in multicolor and multiplexed imaging applications [204]. To generate versatile colors, a new strategy that encapsulate 3 or more energy transfer fluorophores simultaneously inside a single nanoparticle has been developed. By varying the combinations of

encapsulated fluorophores, the FRET mediated emission signature can be tuned in such a way that the particles exhibit different colors after excitation at a single wavelength. Therefore, a large number of encoded nanoparticles can be generated from a combination of limited number of individual fluorophores. The first example of this kind of particles is silica nanoparticles in which three different organic fluorophores i.e. fluorescein, Rhodamine 6G (R6G) and 6-carboxyl-X-Rhodamine (ROX) were incorporated [205]. These fluorophores were carefully selected based on their overlapping emission and excitation spectra in order to allow efficient energy transfer. By doping different combination of three fluorophores, barcoded particles with a single wavelength excitation were produced for multiplexed and multicolor imaging. These nanoparticles were subsequently used for simultaneous monitoring and identification of multiple bacteria or cancer cells [213, 214]. Polymeric nanospheres encapsulating with phosphorescent ruthenium metal-ligand complex and cyanine derivatives were applied to time-resolved multiplexed bioassays [215]. Apart from multiplexed applications, FRET based nanoparticles can also be employed to monitor the integrity of nanoparticles, as the energy transfer is highly dependent on the distance between the donor and acceptor molecules (1−10 nm). For example, polymeric micelles encapsulating a FRET pair (DiO and Dil) showed a significant change in FRET efficiency upon the release of fluorophore molecules, which could be useful for monitoring the stability of polymeric micelles in both *in vitro* and *in vivo* systems.

1.4. Thesis objective

Polymer-based nanomaterials are one of the few materials injected into the body that are easily degraded by body's natural metabolic pathways. They can be synthesized by using polymers or peptides that allow them to mold to various materials, which can act as delivery cargo for therapeutic agents. Furthermore, their unique structure also makes them ideal carriers

for diagnostic molecules. There exists other materials that may have ideal characteristics of delivery cargo, but polymer-based nanomaterials have the most desirable combination of safety, biocompatibility, stability, and theranostic platform for variety of applications.

This dissertation seeks to develop and investigate novel polymeric nanomaterials for several applications that range from *in vitro* multiplex imaging to *in vivo* optical imaging. A systematic approach is reported for the development of fluorophore-doped nanoparticles.

The specific goals of this Ph.D thesis are as follows:

- **Chapter 1:** Design and evaluation of FRET-based polymeric nanoparticles for *in vivo* NIR and FRET imaging.
- **Chapter 2:** Design and evaluation of multiple fluorophores doped nanoparticles for multicolor and multiplexed imaging.
- **Chapter 3:** Evaluation of peptide-based nanofiber as a carrier for tumoral delivery

CHAPTER 2. DEVELOPMENT OF BIOCOMPATIBLE POLYMERIC NANOPARTICLE FOR IN VIVO NIR AND FRET IMAGING*

** Published in Bioconjugate Chem., 2012, 23 (5), pp 981–992, DOI: 10.1021/bc200637h)*
(Copyright © 2012 American Chemical Society)

2.1. Abstract

The majority of near-infrared (NIR) fluorophores are organic molecules that show significant overlapping between the excitation and emission spectra and therefore exhibit high fluorescence backgrounds during *in vivo* imaging. Recently, cyanine dyes with a large Stokes shift have shown great promises for NIR imaging but often undergo rapid photo-degradation and non-specific protein adsorption. Alternatively, fluorescence resonance energy transfer (FRET) is a promising technique to generate a larger gap between the excitation and emission maxima and thus can reduce the background signal. Here, we report the rational design of FRET-based polymeric nanoparticles for NIR imaging. The particles were assembled from diblock copolymers of poly(D,L-lactic-*co*-glycolic acid) and maleimide-activated polyethylene glycol, which were also encapsulated with both the donor (1,1'-dioctadecyl-3,3,3',3'-tetramethylindodicarbocyanine) and acceptor (1,1'-dioctadecyl-3,3,3',3'-tetramethylindotricarbocyanine) fluorophores. Because of their extreme hydrophobicity, thousands of fluorophores could be encapsulated inside a single particle without causing leakage. FRET resulted in a large Stokes shift (>100 nm) of the emission maxima and the transfer efficiency could be fine-tuned by further adjusting the doping ratio of the donor and acceptor fluorophores. The optimized formulation was less than 100 nm in size, brighter than quantum dots, stable in human serum, and demonstrated the similar biodistribution to most nanomaterials.

Additional animal phantom studies demonstrated that the developed FRET imaging platform could have far-reaching applications in optical imaging.

2.2. Background

Optical imaging has become an emerging diagnostic tool that provides several advantages, including higher sensitivity, lower cost, and avoidance of using ionizing radiation, over other imaging modalities [8]. Optical contrast agents are often required to enhance detection sensitivity *in vivo*. To improve tissue penetration, most contrast agents are incorporated with fluorescence reporters that excite and emit photons at the NIR region (650-900 nm) [216]. The majority of these reporters are organic molecules that exhibit high background fluorescence while imaging, because of the small Stokes shift (difference between the excitation and emission maxima of the fluorophore). Alternatively, heptamethine cyanine fluorophores with a larger Stokes shift (>100 nm) can be synthesized [217, 218]. These fluorophores are water soluble and could be easily coupled with a variety of the biological entities including biomolecules such as antibodies, and peptides. However, due to their rapid photo-degradation, nonspecific protein adsorption, and biological or chemical degradation, they are not suitable for long term imaging [15, 219]. Inorganic fluorescent nanocrystals such as quantum dots (QDs) can be used as an alternative [199]. They are known to be more sensitive (brighter) and less susceptible to photo-degradation than organic fluorophores but the unsure long-term toxicities hinder their future application in the clinical settings [200].

One of the approaches to improve the stability of fluorophores is through doping them into/onto nanoparticles [220, 221]. Fluorophores molecules can be incorporated into the nanoparticles *via* ionic interaction, entrapment or covalent conjugation [93]. Unlike organic

fluorophores, nanoparticles-based contrast agents are less prone to the rapid photobleaching and thus allowing long-term and sensitive tracking of the signal. Furthermore, nanoparticles possess unique physiochemical properties that can be exploited in specific disease conditions. For example, in cancer, these contrast agents may accumulate at the tumor site *via* EPR phenomenon and thus helps in the early detection. Another advantage of nanoparticles is that more than one type of fluorophores can be easily incorporated inside single nanoparticle to favor the FRET [205], a process that transfers radiationless energy from an excited state donor fluorophore to a ground state acceptor molecule *via* dipole-dipole interaction [222-224]. Since the energy transfer highly depends on the distance between the donor and acceptor molecules (1-10 nm), FRET can be also employed to monitor the integrity of nanoparticles. For example, polymeric micelles that were encapsulated with FRET pair (DiO and Dil) showed a significant change in FRET efficiency upon the release of fluorophore molecule and thus could be useful for monitoring the stability of polymeric micelles in both *in vitro* and *in vivo* systems [225-227]. However, the employed FRET pairs did not absorb and/or emit photons at the NIR region and therefore potentially limited their use for *in vivo* applications [198]. Until now, no one has explored the utility of FRET in the development of a NIR contrast agent for *in vivo* imaging.

In the present study, we report the development of biocompatible polymeric nanoparticles for *in vivo* NIR and FRET imaging. These particles are composed of diblock copolymers of poly(D,L-lactic-*co*-glycolic acid) (PLGA) and maleimide-activated polyethylene glycol (PLGA-PEG_{3500}-maleimide) [228], and were encapsulated with two lipophilic NIR fluorophores, DiD and DiR, as the donor and acceptor, respectively **(Figure 6)** [150]. One of the advantages of FRET over single fluorophores as the optical reporters is that it has a relatively larger gap between the excitation and emission and thus can significantly reduce the background while

imaging [217]. It is important to note that the observed FRET transfer was efficient, even if there was a smaller overlap between the emission spectra of the donor (DiD) and the excitation spectra of the acceptor (DiR) **(Table 5)** as compared to previously reported Di-series analogues (DiO and Dil) [226, 227]. Energy transfer from DiD to DiR resulted in a decrease of the emission maxima at 668 nm and was accompanied with an increase of the emission maxima at 795 nm. We further demonstrated that these nanoparticles have tremendous potential for *in vivo* imaging.

2.3. Experimental procedures

2.3.1. Chemicals and materials

All solvents were purchased from Fischer Scientific (Pittsburgh, PA). Poly(D,L-lactic-*co*-glycolic acid) (PLGA-COOH, monomer ratio 50:50, 17 kDa) was received as gift samples from PURAC Biomaterials (Netherland). Maleimide-activated PEG (Mal-PEG_{3500}-NH_2, 3.5 kDa) was purchased from JenKem Technology USA, Inc. (Allen, TX). 1,1'-dioctadecyl-3,3,3',3'-tetramethylindodicarbocyanine, 4-chlorobenzenesulfonate salt (DiD) and 1,1'-dioctadecyl-3,3,3',3'-tetramethylindotricarbocyanine iodide (DiR), and Qdot® 800 ITK™ carboxyl quantum dots (QDs-800) were obtained from Life Technologies Corporation (Grand Island, NY). Cy5 and Cy7 monofunctional hydroxysuccinimide ester were purchased from GE Healthcare Biosciences (Piscataway, NJ). Trilite™ fluorescent nanocrystal 665 nm (QDs-665) was purchased from Cytodiagnostics, Inc. (Burlington, Ontario). Uranyl acetate and copper grids were obtained from Electron Microscopy Sciences (Hatfield, PA). 1-ethyl-3-(3-dimethylaminopropyl) carbodiimide (EDC) and *N*-hydroxysuccinimide (NHS) were purchased from Advanced ChemTech (Louisville, KY) and Alfa Aesar (Ward Hill, MA), respectively. Bovine serum albumin (BSA), *N*,*N*-diisopropylethylamine (DIEA), 20% (w/v) Intralipid emulsion, and agar powder were

obtained from Sigma-Aldrich (St. Louis, MO). Whole blood was purchased from Biochemed Services (Winchester, VA). Ellman's reagent was purchased from Enzo Biochem, Inc. (New York, NY). CellTiter 96® AQueous One Solution Cell Proliferation Assay (MTS) was provided by Promega Corporation (Madison, WI).

2.3.2. Synthesis of polymeric constructs (PLGA-PEG_{3500}-maleimide)

The copolymer was synthesized by standard carbodiimide chemistry, as previously described [164]. PLGA-COOH (1 g, 0.06 mmoL) dissolved in anhydrous dichloromethane (DCM, 10 mL) was activated by adding excess NHS (0.035 g, 0.30 mmoL) and EDC (0.056 g, 0.30 mmoL). After 4 h, the activated PLGA-NHS ester was precipitated in ice cold diethyl ether (25 mL), washed with a mixture of ice cold methanol and diethyl ether (30:70, 3 × 5 mL) to remove the unreacted NHS, and dried under the vacuum. The collected precipitate (0.8 g, 0.047 mmoL) was then dissolved in chloroform (8 mL). Mal-PEG-NH_2 (0.217 g, 0.062 mmoL) was then added to the solution mixture, in the presence of DIEA (0.028 g, 0.22 mmoL). The solution mixture was stirred in the dark for 12 h at room temperature. The copolymer was then precipitated in ice cold diethyl ether (25 mL) and washed with ice cold methanol (3 × 5 mL) to remove the unreacted PEG. The final product, PLGA-PEG_{3500}-maleimide, was dried under the vacuum to remove the residual solvents and further characterized by ^{1}H-NMR spectroscopy. ^{1}H-NMR (400 Hz, $CDCl_3$): δ 6.70 (2H, -CH=, s), δ 5.22 (1H, –C(O)CH(CH_3)O–, m), δ 4.83 (2H, –C(O)CH_2O–, m), δ 3.64 (4H, –OCH_2CH_2–, s), δ 1.58 (3H, –C(O)CH(CH_3)O–, dd).

2.3.3. Nanoparticle assembly

All the nanoparticles were fabricated by the nanoprecipitation method as previously described in chapter 1.2.1.1 [229, 230]. The single fluorophore-doped nanoparticles were synthesized by mixing PLGA-PEG_{3500}-maleimide (2 mg) with different amounts of DiD or DiR fluorophores (0.05 to 3% w/w) in DMF (0.2 mL). The solution mixtures were then added dropwise to deionized water (2 mL). The resulting particles were allowed to stir for 2 h at room temperature. Nanoparticles were then purified by ultracentrifugation (3000 × *g*, 15 min) using SPIN-X UF concentrators with 10 kDa MWCO (Corning Incorporated, Lowell, MA) and washed with deionized water (2 × 5 mL) to remove the free fluorophores. The purified nanoparticles were re-suspended in deionized water (0.2 mL) and stored at 4°C. Using the same protocol, FRET nanoparticles (FRET-NPs) were synthesized by adding a mixture of DiD and DiR fluorophores (1:1 ratio) to the copolymer.

2.3.4. Physical characterization of the particles

Particle size and zeta potential were measured by dynamic light scattering (Zetasizer, Malvern Instruments, Worcestershire, U.K.). The equipment was first calibrated according to the manufacturer's instruction, using the certified zeta potential transfer standard (DTS1050). For the size measurement, the samples (0.2 mg/mL) were loaded in a disposable polystyrene cuvette. All measurements were recorded with the same particle concentration in deionized water at 25°C. The solvent parameters such as refractive index and viscosity were set at 1.33 and 0.8872 cP, respectively. The intensity-weighted mean values were recorded as the average of three independent measurements. The zeta potentials of the particles (0.2 mg/mL) were measured in a disposable capillary cell (Malvern Instruments, Worcestershire, U.K).

The surface morphology and the size of the particles were confirmed by high resolution transmission electron microscope (JEM-2100, Jeol Ltd., Peabody, MA). Samples were negatively stained with uranyl acetate [231]. Briefly, nanoparticles (2 mg/mL) in deionized water (10 µL) were adsorbed on to 200 mesh formvar/carbon coated grids for 5 min and the excess samples were blotted off by a filter paper. The grids were stained with 3% (w/v) uranyl acetate in deionized water (10 µL) for 5 min and then blotted off. Finally, the grids were air-dried and images were acquired using computer controlled camera.

2.3.5. Determination of particle numbers

The number of nanoparticles (*n*) in the stock solution was estimated as previously described from the following equation [232]:

$$n = \frac{6c}{\pi \times d^3 \times \rho_P} \quad \text{..... (4)}$$

Where *c* is the polymer concentration, *d* is the particle hydrodynamic diameter obtained by dynamic light scattering, and ρ_p is the density of PLGA nanoparticle core (estimated to be 1.27 g cm^{-3} at 20°C).

2.3.6. Determination of fluorophore contents in the particles

The fluorophore loading (% w/w) of the particles was determined by UV absorbance. The numbers of particles in the stock solutions were first determined by using the equation (1). The solution mixtures (~3×10^{13} particles/mL) were then freeze-dried, weighed (~ 0.5 mg), and re-dissolved in DMSO (1 mL) to extract the encapsulated fluorophores. The resulting mixtures were centrifuged (10,000 × *g*, 5 min) to remove any visible aggregate. The amount of

fluorophores in the solution mixtures were further quantified by absorbance according to our predetermined extinction coefficient values in DMSO ($\varepsilon_{DiD\ at\ 655\ nm}$ = 173,000 M^{-1} cm^{-1} and $\varepsilon_{DiR\ at\ 760\ nm}$ = 207,000 M^{-1} cm^{-1}).

The percentage of fluorophore loading was calculated from the following equation [233]:

$$\%\ \text{Fluorophore loading} = \frac{\text{Weight of the encapsulated fluorophore}}{\text{Total weight of the particles}} \times 100\ \% \quad \text{..... (5)}$$

The loading efficiency was calculated from the following equation [233]:

$$\%\ \text{Loading efficiency} = \frac{\text{Weight of the encapsulated fluorophore}}{\text{Weight of the fluorophore used for the particle assembly}} \times 100\ \% \quad \text{..... (6)}$$

The number of fluorophores per particle was calculated from the following equation:

$$\text{No. of fluorophores per particle} = \frac{\text{Weight of the encapsulated fluorophore}}{\text{Molecular weight of the fluorophore x No.of particles}} \quad \text{..... (7)}$$

To accurately determine the amount of the individual fluorophore in FRET-NPs, the absorbance at the λ_{max1} and λ_{max2} were first corrected from the degree of spectral overlap of the DiD and DiR fluorophores [234].

2.3.7. Measurement of absorbance and fluorescence

All measurements were recorded in deionized water at room temperature, using a sub-microcuvette for absorbance or fluorescence (Starna Cells, Inc., Atascadero, CA). For the ease of comparison, all samples were diluted to the same particle number (1×10^{12} particles/mL) in deionized water (100 µL). Absorption spectra were collected from a spectrophotometer (Spectramax, Molecular Devices, LLC, Sunnyvale, CA). Fluorescence spectra were measured on

a spectrofluorometer (Cary Eclipse, Agilent Technologies, Inc., Santa Clara, CA). The DiD-doped nanoparticles and FRET-NPs were excited at 650 nm and the DiR-doped nanoparticles were excited at 755 nm. Fluorescence emissions were recorded between 660 to 850 nm with a scanning interval of 0.2 nm. The excitation and emission slit widths were set at 2.5 and 5 nm, respectively.

2.3.8. Measurement of extinction coefficient (ε) and quantum yield (Φ)

The number of particles in stock solutions and the number of fluorophores in each particle were first determined from equations (4) and (7), respectively. The extinction coefficient of the particles (ε) was determined from the Lambert-Beer's law [235]. Note: The extinction coefficient based on the amount of fluorophore (ε_f) was calculated by dividing the ε value with the total number of fluorophores in the respective particles.

The relative quantum yield was determined in deionized water by the previously described comparative method [97, 236], using Cy5 and Cy7 as the reference standards for DiD- and DiR-doped nanoparticles, respectively [150]. Each particle sample was prepared in a series of four dilutions (0.1-0.5 μM of the fluorophore). The DiD- and DiR-doped nanoparticles were excited at 640 and 740 nm, respectively. The entire fluorescence spectra (from 660 to 850 nm) were then recorded and integrated using the Prism software (GraphPad Software, Inc., La Jolla, CA). The relative quantum yield was then calculated from the following equation as previously described [237]:

$$\Phi = \Phi_R \left(\frac{M}{M_R}\right)\left(\frac{n^2}{n_R^2}\right) \quad (8)$$

Where, Φ and Φ_R are the quantum yields of the sample and its corresponding reference, respectively; M and M_R are the slopes calculated from a plot of the absorbance at excitation wavelength versus the integrated fluorescence spectra, and n is the refractive index of the solvent, i.e. deionized water.

2.3.9. Calculation of net FRET (nFRET), FRET ratio (R_{FRET}), and FRET efficiency (E_{FRET}) of FRET-NPs

FRET signals were converted to the net FRET value (*nFRET*) as previously described [238, 239]. Briefly, the fractional cross-talks of the DiD and DiR fluorophores in the FRET setting were first determined from the following equations:

$$a = \frac{I_{DiD\ at\ 775\ nm\ (\lambda_{650\ nm})}}{I_{DiD\ at\ 668\ nm (\lambda_{650\ nm})}} \quad (9)$$

$$b = \frac{I_{DiR\ at\ 775\ nm\ (\lambda_{650\ nm})}}{I_{DiR\ at\ 775\ nm\ (\lambda_{755\ nm})}} \quad (10)$$

Where, $a = 0.04$, was determined by dividing the fluorescence intensity of DiD-doped nanoparticles (excited at 650 nm) at the acceptor emission λ_{max} (775 nm) with the intensity at the donor emission λ_{max} (668 nm) and $b = 0.03$, was determined by dividing the fluorescence intensity of DiR-doped nanoparticles at the acceptor emission λ_{max} (775 nm) when excited at 650 nm with the intensity when excited at 755 nm.

The net FRET (*nFRET*) was then calculated from the following equation [238]:

$$nFRET = I_{FRET} - a \times I_{DiD} - b \times I_{DiR} \quad (11)$$

Where I_{FRET}, I_{DiD}, and I_{DiR} are the fluorescence intensities of FRET-NPs at the FRET, DiD, and DiR settings. The FRET ratio (R_{FRET}) was calculated by dividing the *nFRET* values by I_{DiD} [240].

FRET efficiencies (E_{FRET}) were determined according to the donor-based and acceptor-based methods as previously described [241, 242]. Briefly, the respective steady-state fluorescence emission spectra (excited at 650 nm) were recorded: (1) the emission of FRET-NPs (F_{FRET}; recorded at 660-850 nm), (2) emission of DiD-doped nanoparticles consisting of the same total fluorophore contents as the FRET-NPs (F_{DiD}; recorded at 660-850 nm) and (3) the acceptor emission of DiR-doped nanoparticles consisting of the same total fluorophore contents as the FRET-NPs (F_{DiR}; recorded at 660-850 nm). The emission spectra were further integrated using Prism software. The donor-based FRET efficiency (E_D) was calculated from the following equation [241, 242]:

$$\mathrm{E_D} = 1 - \frac{\int_{660}^{774} \mathrm{F_{FRET}\ d(nm)}}{\int_{660}^{774} \mathrm{F_{DiD}\ d(nm)}} \quad \text{(12)}$$

The acceptor-based FRET efficiency (E_A) was calculated from the following equation [241, 242]:

$$\mathrm{E_A} = \frac{\varepsilon_{\mathrm{DiD\ at\ 650\ nm}}}{\varepsilon_{\mathrm{DiR\ at\ 650\ nm}}}\left(\frac{\int_{775}^{850} \mathrm{F_{FRET}\ d(nm)} - \int_{775}^{850} \mathrm{F_{DiD}\ d(nm)}}{\int_{775}^{850} \mathrm{F_{DiR}\ d(nm)}} - 1\right) \quad \text{(13)}$$

Where, $\varepsilon_{DiD\ at\ 650\ nm}$ and $\varepsilon_{DiR\ at\ 650\ nm}$ are the extinction coefficients of DiD- and DiR-doped nanoparticles at 650 nm, respectively.

2.3.10. Comparison of the brightness of the particles

The brightness of single-fluorophore doped nanoparticles was determined using a reflectance imaging system (*In-vivo* system FX, Carestream Health, Inc., Rochester, NY) as described previously [243]. The imaging system was equipped with a halogen lamp (150 W) as an excitation light source. Band pass filters (Carestream Health, Inc., Rochester, NY) were employed to adjust the corresponding excitation wavelengths for DiD (615/645 nm) and DiR (700/740 nm) fluorophores. Briefly, the particles (1×10^{12} particles/mL) suspended in deionized water (100 µL) were added to the wells of a clear-bottom 96-well black plate (Corning Incorporated, Lowell, MA). The plates were then exposed to the excitation light source. The emitted light were collected using the corresponding band pass filters (Carestream Health, Inc., Rochester, NY) for DiD (680/720 nm) and DiR (770/810 nm). All images were acquired with a single exposure time of 5 min and were further analyzed using Kodak molecular imaging software (Carestream Health, Inc., Rochester, NY). The region of interest (ROI) of individual wells was selected for the determination of the relative fluorescence intensities.

The brightness of the particles was also compared with the commercially available quantum dots (QDs-650 and QDs-800) using a spectrofluorometer (Cary Eclipse, Agilent Technologies, Inc., Santa Clara, CA). The samples were first diluted to the same number of particles ($1\text{-}5 \times 10^{12}$ particles/mL) in deionized water (100 µL). For the ease of comparison, QDs were prepared in a series of four different particle concentrations ($1\text{-}5 \times 10^{12\text{-}14}$ particles/mL) in deionized water (100 µL). The QDs were excited at 465 nm and fluorescence emissions were recorded (from 600 to 850 nm).

2.3.11. Quenching of maleimide groups of FRET-NPs

The surface maleimide groups of FRET-NPs were neutralized by cysteine. Briefly, FRET-NPs (1 mg, 47 nmoL) and cysteine (0.1 mg, 820 nmoL) were dissolved in 1 mL of phosphate buffer (pH 8, 100 mM). After 2 h, the resultant FRET-NPs were purified by ultracentrifugation (15 min, 3000 × *g*) using SPIN-X UF concentrators with 10 kDa MWCO. The successful quenching of the maleimide groups was confirmed by the determination of unreacted cysteine using the Ellman's reagent as previously described [244].

2.3.12. Synthesis of IgG-conjugated FRET-NPs (IgG-FRET-NPs)

Free sulfhydryl groups were first introduced to IgGs amino acid sequence by reacting the primary amino groups of human IgG antibody (100 µg) with a 50 molar excess of 2-iminothiolane (16.5 µL, 4mM) in PBS (200 µL, 10 mM, pH 8.0) for 2 h. The reaction mixture was then washed and purified by ultracentrifugation (15 min, 3000 × *g*) using SPIN-X UF concentrators with 10 kDa MWCO (Coaster, Corning, NY). The resulting thiolated IgG (50 µg) was then reacted with the FRET-NPs (500 µg) in PBS (0.2 mL, 10 mM, pH 7.4) for 4 h and further purified by size-exclusion chromatography (Sephacryl-300 HR, GE Healthcare, Piscataway, NJ). The successful conjugation of the IgG antibody was confirmed by UV-visible spectroscopy by recording the absorption at λmax=280 nm.

2.3.13. MTS assay

MTS assays were performed as previously described [245]. Both mouse leukemic monocyte macrophage (RAW 264.7) and human embryonic kidney (HEK-293) cell lines were obtained from American Type Culture Collection (Manassas, VA) and maintained in Dulbecco's

Modified Eagle Medium (DMEM) supplemented with 10% (v/v) fetal bovine serum (FBS), penicillin (50,000 units/L), and streptomycin (50 mg/L) at 37°C. The cells (5000/well) in complete DMEM medium (100 µL) were seeded in a clear bottom 96-well plate (Corning Incorporated, Lowell, MA). After 12 h, fresh complete DMEM medium (150 µL) mixed with FRET-NPs (0.4-2 mg/mL) in sterile PBS (50 µL) were added to the cells and incubated at 37°C. Cells incubated with PBS served as a negative control. After 24 h of incubation, fresh complete DMEM medium (100 µL) containing MTS reagent (20 µL) was added to each well and the cell viability was determined by measuring the absorbance (A) at 490 nm at 1 h. The percentage cell viability relative to the negative control was determined by using the following equation:

$$(A_{sample})/(A_{control}) \times 100\% \quad \text{.....(14)}$$

2.3.14. Hemolysis assay

The hemocompatibility of the particles was tested on erythrocytes as previously described [246]. The erythrocytes were isolated from the blood by centrifugation (800 × *g*, 15 min) and further washed with PBS. The stock of erythrocytes dispersion (3.5×10^8 cell/mL) in PBS (100 µL) was mixed with FRET-NPs (0.2-2 mg/mL) in PBS (100 µL) and then incubated at 37°C. 10% (v/v) Triton X-100 and PBS were used as the positive and negative controls, respectively. After 3 h, the intact erythrocytes were separated by centrifugation (800 × *g*, 15 min) and the absorbance of the supernatant (100 µL) was measured at 540 nm to detect the presence of the released hemoglobin. All absorption values were corrected for the intrinsic absorbance of the particles. The percentage of hemolysis was calculated using the following equation:

$$(A_{sample}-A_{negative})/ (A_{positive}-A_{negative}) \times 100 \quad \text{.....(15)}$$

2.3.15. *In vitro* stability studies

To determine the long term colloidal stability, FRET-NPs (1 mg/mL) were first suspended in deionized water (1 mL) and then kept at room temperature. The particle size and the zeta potential were measured by dynamic light scattering (DLS) for 7 days. The physical stability of particles was tested in different biological media as previously described [247]. Briefly, FRET-NPs (2 mg/mL) suspended in deionized water (500 µL) were added to different media (500 µL), including PBS alone, 9.0% (w/v) of BSA in PBS, and 20% (v/v) of FBS in minimum essential medium (MEM). Deionized water was used as a negative control. The solution mixtures were incubated at 37°C. At different time points, an aliquot of nanoparticles solutions (100 µL) was collected to measure their sizes. Similarly, the changes in the optical properties of the particles (0.1 mg/mL) with time was determined [226]. After each time point, an aliquot of nanoparticles in the media (100 µL) was collected and the fluorescence intensities were recorded between 660 to 850 nm after excitation at 650 nm. The FRET ratio (R_{FRET}) was calculated by dividing the *nFRET* values by I_{DiD}. All the FRET ratio values were normalized according to the corresponding samples at t=0 h (R_{FRET}=1).

2.3.16. Biodistribution studies

Four to five week old female, Severe Combined Immunodeficiency (SCID) hairless outbred *(SHO-Prkdc^{scid}Hr^{hr})* mice (approximately 20 g in weight) were purchased from Charles River Laboratories (Wilmington, MA). The animals were maintained in a pathogen-free and temperature-controlled environment and were provided with sterilized food and water. All the animal experiments were performed according to the guidelines of the Institutional Animal Care and Use Committees (IACUC) at North Dakota State University. For the biodistribution study,

mice were injected with the same number of FRET-NPs (5×10^{12}/mL) in PBS (100 µL) *via* tail-vein. After 24 h, the mice were euthanized by intraperitoneal injection of pentobarbital (100 mg/kg) and different organs including livers, hearts, bladders, kidneys, spleens, brains, lungs, stomachs, pancreas, and intestines were excised, washed, and imaged using a reflectance imaging system by employing the FRET channel (excited at 615/645 nm and recorded at 770/810 nm). All images were collected with a single exposure time of 5 min and were further processed using Kodak molecular imaging software. Following imaging, each organ was weighed (50 mg), homogenized with DMSO (200 µL), and centrifuged (5000 × *g*, 5 min). The fluorescence intensity of the supernatant (100 µL) was recorded on a spectrofluorometer and the amount of FRET-NPs was quantitatively determined according to the standard curve. The standard curve was generated by mixing known amounts of FRET-NPs in deionized water with the corresponding isolated organ (50 mg) from an uninjected mouse and extracted as described above. All the data was normalized in unit of percentage of injected dose per gram of the tissue (% ID/g).

2.3.17. Phantom studies

For the phantom study, the mice were first euthanized by intraperitoneal injection of pentobarbital (100 mg/kg). A glass capillary tube (1.1 × 90 mm) filled with FRET-NPs or DiR-doped nanoparticles (5×10^{12} particles/mL) in deionized water (10 µL) was then carefully inserted into the thoracic region *via* the mouth of the animal. The images were then acquired at the respective channels: DiD (excited at 615/645 nm and recorded at 680/720 nm), DiR (excited at 700/740 nm and recorded at 770/810 nm), and FRET (excited at 615/645 nm and recorded at 770/810 nm). Water soluble QDs-800 (2.5×10^{13} particles/mL) in deionized water (10 µL) was

used as a positive control and the images were acquired with excitation at 445/485 nm and recorded at 770/810 nm. All images were recorded with a single exposure time of 5 min and were further processed using Kodak molecular imaging software.

2.3.18. Imaging data processing and analysis

All the raw images were processed using PixFRET ImageJ plug-in freeware as previously described [248]. Briefly, the fractional cross-talk values of DiD (a = 0.09) and DiR (b = 0.26) fluorophores were first determined from equation (9) and (10), using the phantom containing only the DiD- and DiR-doped nanoparticles (2.10% w/w), respectively. The FRET image of the FRET-NPs phantom was then corrected for the fractional cross-talk values as well as the background fluorescence to obtain the *nFRET* image. For data analysis, the signal-to-phantom background ratio was determined by dividing the signal intensity of the sample with the phantom background at the ROIs. The phantom images of DiR-doped nanoparticles and QDs-800 were corrected for the background fluorescence. A constant Gaussian blur (2.0) and a threshold (1.0) values were applied to all the images.

2.4. Results and discussion

2.4.1. Synthesis of the polymeric constructs (PLGA-PEG_{3500}-maleimide)

The nanoparticles were composed of PLGA-PEG_{3500}-maleimide copolymers (**Figure 6A**), which were synthesized by reacting an equivalent amount of maleimide-activated polyethylene glycol (Mal-PEG_{3500}-NH_2) with poly(D,L-lactic-*co*-glycolic acid) carboxylic acid (PLGA-COOH) in DCM [164]. The resulting copolymer was recovered by precipitation in diethyl ether and further washed with methanol to remove the unreacted Mal-PEG_{3500}-NH_2. The

final product, PLGA-PEG_{3500}-maleimide, was confirmed by ^{1}H-NMR **(Figure 7)**. When compared to the ^{1}H-NMR spectrum of PLGA-COOH **(Figure 8),** an additional peak (-OCH_2CH_2-, s) appeared at 3.64 ppm indicating that the reaction was successful [164]. A small peak observed at 6.70 ppm (-CH=, s) also confirmed the preservation of the maleimide groups [249]. The coupling efficiency of the reaction was calculated based on the relative integration of the peaks at 3.64 and 5.22 ppm for PEG and PLGA, respectively and was estimated to be approximately 50%.

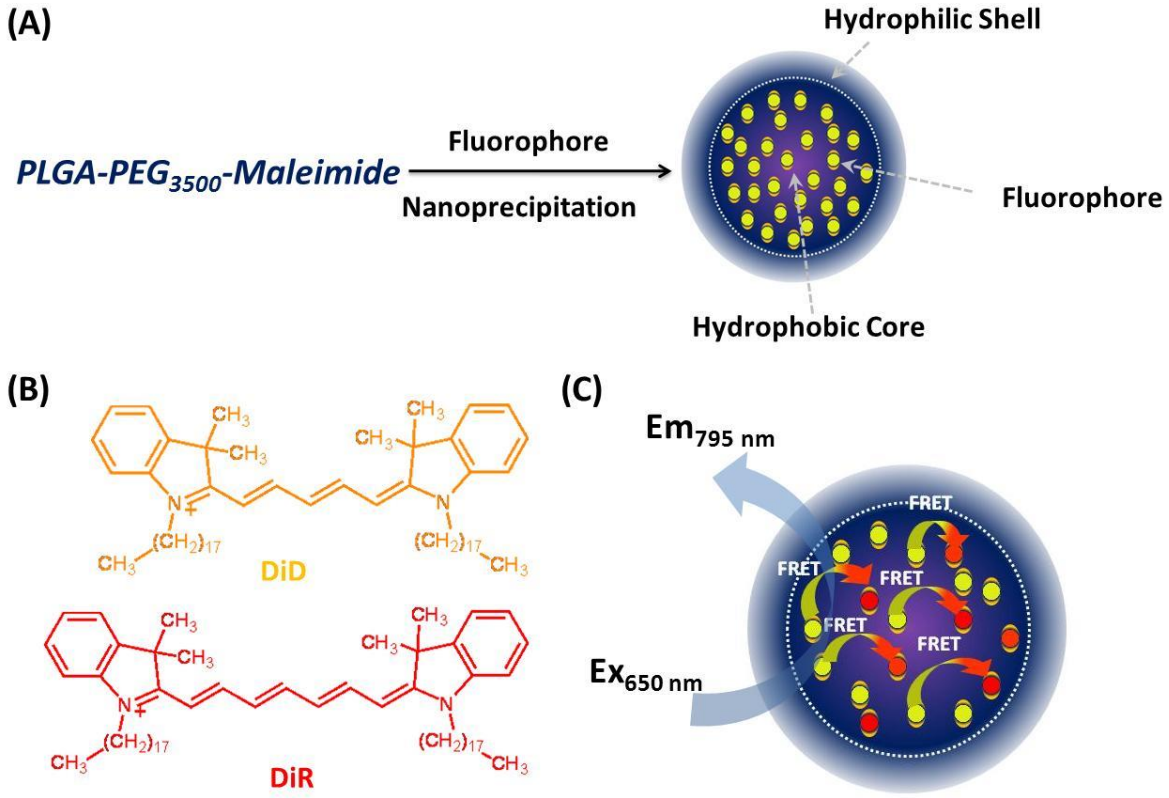

Figure 6. The design of FRET-NPs. (A) Nanoparticles was synthesized by nanoprecipitation method [164, 229]. DiD fluorophore, with excitation λmax at 644 nm and emission λmax at 665 nm in methanol, and DiR fluorophore with excitation λmax at 750 nm and emission λmax at 780 nm, in methanol were encapsulated inside the FRET-NPs. (B) The chemical structures of DiD and DiR fluorophores. (C) The close proximity between the entrapped DiD and DiR fluorophores favored the phenomenon of fluorescence resonance energy transfer (FRET).

2.4.2. Particle assembly

All particles were assembled from the PLGA-PEG_{3500}-maleimide copolymers by previously described nanoprecipitation method (**Figure 6**) [230]. This method is simple and does not require the use of surfactant or toxic solvent [250]. Nanoparticles of various sizes (65 nm to 300 nm) can be synthesized simply by changing the solvent parameters [251] and polymer concentrations [164]. To synthesize nanoparticles of less than 100 nm in size, a mixture of copolymer constructs and fluorophores in DMF was added dropwise to deionized water. This procedure has been employed previously to encapsulate a large amount of hydrophobic drug molecules (~18% w/w) in the nanoparticles [161].

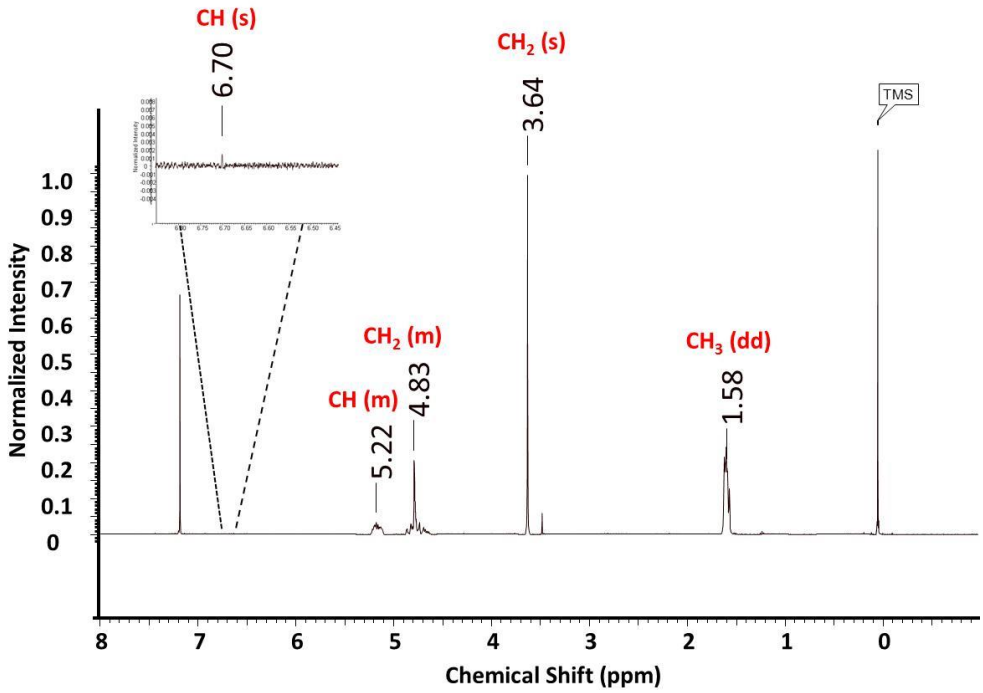

Figure 7. ^{1}H-NMR spectra of PLGA-PEG-maleimide (5 mg/ml) in $CDCl_3$.

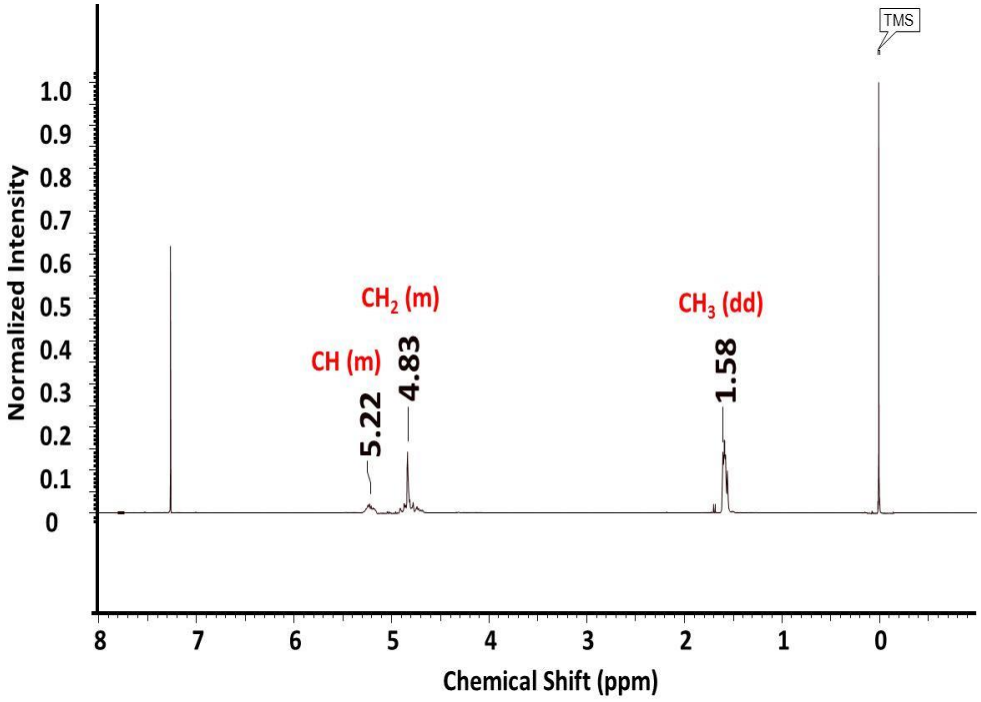

Figure 8. ^{1}H-NMR spectra of PLGA (5 mg/mL) in $CDCl_3$.

2.4.3. Physical characterization of the single-fluorophore doped nanoparticles

DiD and DiR are carbocyanine derivatives and are conjugated with lipophilic alkyl tails (C_{18}) at the imine nitrogens. The fluorophores were originally developed as organelle sensors for cell membrane, mitochondria, and endoplasmic reticulum [252, 253]. To investigate whether particles composed of PLGA-PEG_{3500}-maleimide copolymers could be used as a fluorophore carrier, a series of particles encapsulated with various amounts of DiD or DiR fluorophores (0.0-2.10% w/w) were prepared.

Table 5. The optical properties of FRET pairs.

FRET Pair	***Overlap (%)****	***Wavelength (nm)***
DiO and Dil	61	521
DiD and DiR	36	700

* The percentage overlap was determined using Invitrogen fluorescence spectra viewer.

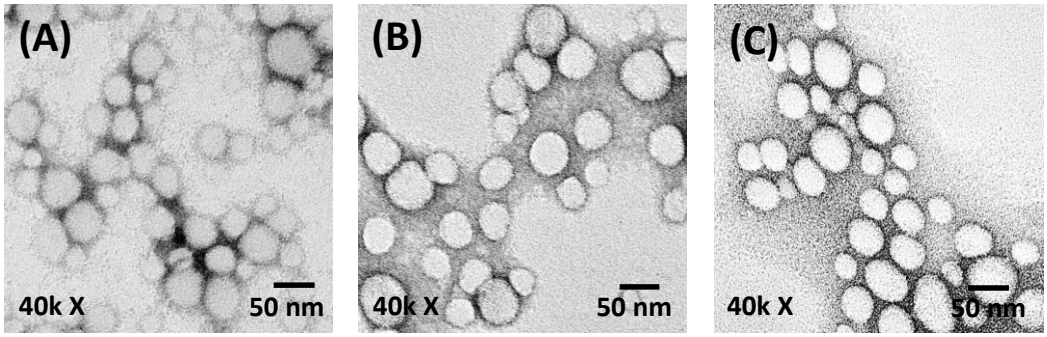

Figure 9. The transmission electron microscope (TEM) images of (A) blank nanoparticles, (B) DiD-doped nanoparticles (0.72% w/w), and (C) DiR-doped nanoparticles (0.74% w/w). The particles were negatively stained with uranyl acetate (3% w/v) (Scale bar = 50 nm).

Table 6. The physical properties of single fluorophore-doped nanoparticles.

NPs	*Fluorophore Content*		*Loading Efficiency (%)*	*Particle Size (nm)*	*Zeta Potential (mV)*	*Polydispersity*	*Number of Fluorophores/ Particle*
	Used (% w/w)	*Loading (% w/w)*					
	0	0.00 ± 0.00	00 ± 0	57 ± 2	-17.0 ± 2.0	0.17 ± 0.02	0
DiD-doped Nanoparticles	0.05	0.04 ± 0.01	88 ± 9	58 ± 2	-17.5 ± 0.5	0.15 ± 0.05	33
	0.10	0.08 ± 0.01	87 ± 11	61 ± 2	-17.7 ± 1.5	0.13 ± 0.04	70
	0.25	0.20 ± 0.04	83 ± 13	60 ± 1	-17.7 ± 1.5	0.16 ± 0.05	161
	0.50	0.38 ± 0.05	75 ± 10	66 ± 3	-15.4 ± 0.8	0.16 ± 0.04	419
	1	0.72 ± 0.09	72 ± 10	68 ± 5	-17.0 ± 0.7	0.14 ± 0.03	756
	2	1.46 ± 0.09	73 ± 5	71 ± 4	-16.8 ± 0.2	0.11 ± 0.03	2048
	3	2.10 ± 0.17	70 ± 6	84 ± 8	-17.3 ± 0.5	0.17 ± 0.03	4908
DiR-doped Nanoparticles	0.05	0.04 ± 0.01	90 ± 7	56 ± 3	-15.2 ± 0.7	0.16 ± 0.03	31
	0.10	0.08 ± 0.02	88 ± 9	58 ± 4	-16.5 ± 0.8	0.15 ± 0.02	68
	0.25	0.20 ± 0.03	80 ± 10	64 ± 2	-16.3 ± 0.9	0.17 ± 0.04	205
	0.50	0.38 ± 0.08	76 ± 14	60 ± 3	-18.2 ± 0.3	0.15 ± 0.01	323
	1	0.74 ± 0.04	75 ± 4	61 ± 4	-17.1 ± 1.8	0.11 ± 0.02	666
	2	1.50 ± 0.18	76 ± 9	72 ± 4	-15.6 ± 2.3	0.12 ± 0.02	2295
	3	2.10 ± 0.14	69 ± 5	85 ± 5	-16.0 ± 1.0	0.15 ± 0.03	5104

The DiD and DiR fluorophores were chosen because of their extreme hydrophobicity, therefore hundreds to thousands of the fluorophores could be easily encapsulated inside a single particle. Here, all the single fluorophore-doped particles synthesized were less than 100 nm, as the sizes were confirmed by DLS (**Table 6**) and TEM analysis **(Figure 9)**. There was no significant difference in their zeta potentials, which suggested that the fluorophores were entrapped inside the hydrophobic PLGA matrices **(Table 6).** However, increasing the

fluorophore loadings (from 0.0 to 2.10% w/w) resulted in a gradual increase of the particle size (from ~56 to 85 nm).

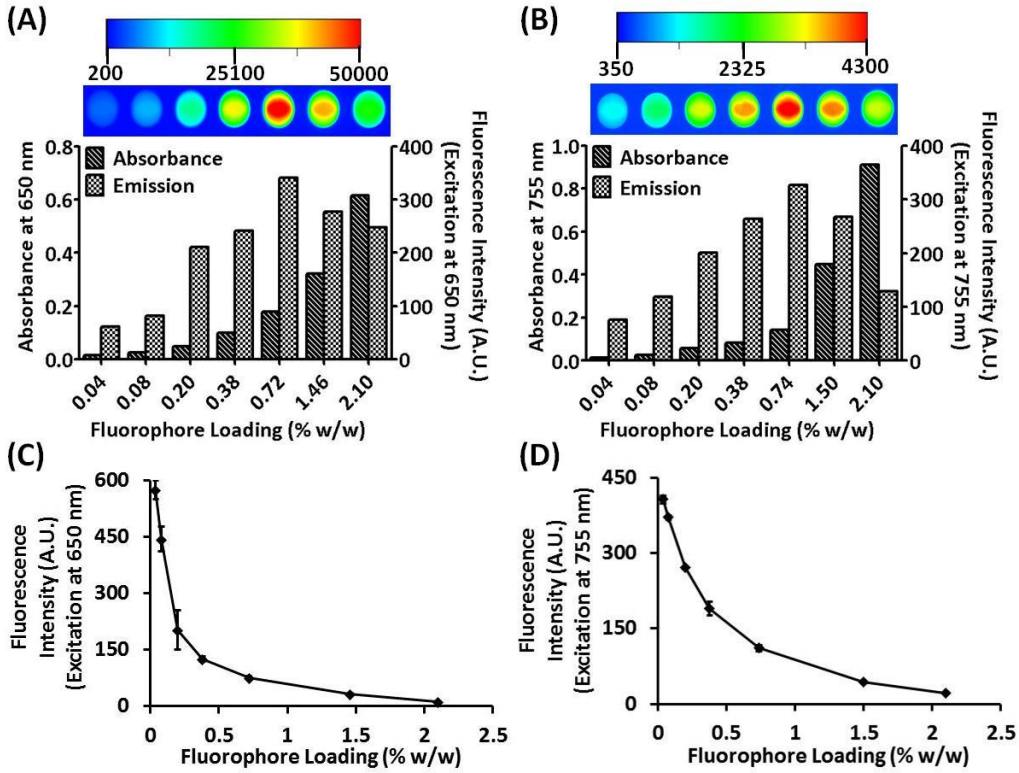

Figure 10. Optical properties of the single fluorophore-doped nanoparticles. A bar chart shows the absorbance and fluorescence emission of (A) DiD- and (B) DiR-doped nanoparticles (0.0-2.10% w/w). All samples consisted of the same number of particles in deionized water (1×10^{12} particles/mL, 100 µL). Insets: The fluorescence images of the particles in a 96-wells plate were acquired by a NIRF reflectance imaging system. A plot of the normalized fluorescence intensities of (C) DiD- and (D) DiR-doped nanoparticles versus fluorophore loadings. The fluorescence intensities were normalized to same fluorophore content (400 nM).

2.4.4. Optical properties of the single-fluorophore doped nanoparticles

Encapsulating a large number of organic fluorophores in a single particle may cause significant fluorescence self-quenching, presumably because the fluorophores are constrained in a close proximity [254]. To compare the optical properties between the single fluorophore-doped nanoparticles, all particles were first diluted to the same particle concentration (1×10^{12}

particles/mL) prior to record the absorbance and emission spectra. Our result demonstrated that with increasing the fluorophore loading, both the absorbance and fluorescence emission increased **(Figure 10A and B)** and were accompanied with continuous blue-shift and red-shift of the absorption and emission λ_{max}, respectively **(Table 7),** which suggested that the entrapped fluorophores were gradually experiencing an increasing hydrophobic environment [146]. Particles encapsulated with ~0.70% w/w of fluorophores were among the brightest **(Figure 10A and B)** and were stable from continuous light irradiation **(Figure 11)**. On the other hand, significant fluorescence quenching was observed in particles with fluorophore loading ≥ 0.70% w/w.

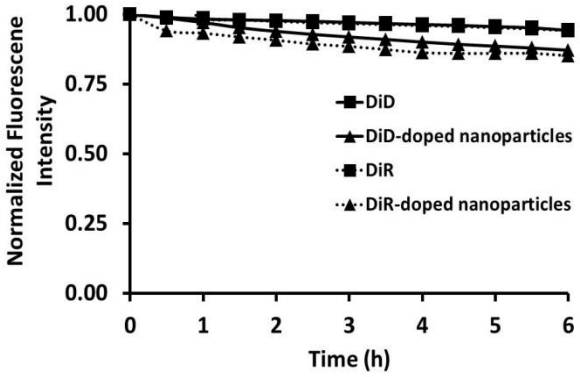

Figure 11. Photostability of single fluorophore-doped nanoparticles. The photostability of DiD- (0.72% w/w) and DiR-doped nanoparticles (0.74% w/w) in deionized water were compared with their corresponding free fluorophores in DMF. All samples were normalized to the same fluorophore contents (1 µM, 10 µL). The samples were loaded into glass capillary tubes (1.1 × 90 mm) and were continuously exposed to a 150 W halogen lamp in the homogeneous lightening field for 6 h. The images were then acquired at the respective channels for every 30 min and the regions of interest were selected for determination of the relative fluorescence intensities.

To study the quenching effect, we determined the quantum yield (Φ) of the particles as previously described [237]. For particles that consisted of a minimal fluorophore content, i.e. 0.04% w/w, the Φ values were comparable to the corresponding free DiD and DiR fluorophores in methanol **(Table 7)** [150], as well as other reported carbocyanine derivatives [255]. As expected, the Φ values declined with further increase in the fluorophore content. Surprisingly, a

plot of the normalized fluorescence intensity (according to the total fluorophore content) versus the fluorophore loading revealed that quenching even occurred in particles consisting of low fluorophore content **(Figure 10C and D)**. This suggested that there might be a non-uniform absorption of the incident light by the encapsulated fluorophores inside the particles, as reflected by the linear decrease in the extinction coefficient values with increasing the fluorophore contents **(Table 7).**

Table 7. The optical properties of single fluorophore-doped nanoparticles.

NP	*Fluorophore Content*		*Absorbance*	*Emission*	*Extinction Coefficient (ε)*		*Quantum*
	Used (% w/w)	*Loading (% w/w)*	*λ_{max} (nm)*	*λ_{max} (nm)*	*(ε) Per Particle x 10^7 ($M^{-1}cm^{-1}$)*	*(ε_f) Per Fluorophore x 10^5 ($M^{-1}cm^{-1}$)**	*Yield (Φ)*
DiD-doped Nanoparticles	0.05	0.04 ± 0.01	652	665	0.84	2.55	0.34
	0.10	0.08 ± 0.01	652	665	1.51	2.14	0.27
	0.25	0.20 ± 0.04	651	666	2.94	1.82	0.26
	0.50	0.38 ± 0.05	650	667	5.99	1.43	0.21
	1	0.72 ± 0.09	650	668	10.7	1.42	0.10
	2	1.46 ± 0.09	650	668	19.5	0.95	0.05
	3	2.10 ± 0.17	649	668	37.1	0.75	0.02
DiR-doped Nanoparticles	0.05	0.04 ± 0.01	759	769	0.79	2.56	0.46
	0.10	0.08 ± 0.02	758	771	1.54	2.27	0.31
	0.25	0.20 ± 0.03	755	772	3.43	1.68	0.24
	0.50	0.38 ± 0.08	755	774	4.94	1.53	0.16
	1	0.74 ± 0.04	755	773	8.61	1.29	0.08
	2	1.50 ± 0.18	755	775	27.1	1.18	0.04
	3	2.10 ± 0.14	754	781	54.8	1.07	0.02

*****The extinction coefficient per fluorophore was calculated by dividing by ε_f value with the number of fluorophores per particle.

Next, we compared the brightest of the particles with the water soluble quantum dots (QDs-665 and QDs-800). The optimized DiD- and DiR-doped nanoparticles were more than 100 and 70 times brighter than their corresponding QDs, respectively **(Figure 12).**

2.4.5. FRET-based nanoparticles

FRET is known to be affected by the distance between the donor and acceptor fluorophores and the orientation factor of the employed FRET pair [205]. To determine an optimum fluorophore loading for the efficient FRET, a series of particles were synthesized by

encapsulating an equal mixture of DiD and DiR but different total fluorophore contents (0.20, 0.38, 0.72, 1.48, and 2.10% w/w) inside our developed polymeric platform. The resulting FRET-NPs were characterized and found having the similar physical properties as the single-fluorophore doped nanoparticles **(Table 6 and 8).** The two absorption maxima, λ_{max1} and $\lambda_{max2,}$ appeared in the absorption spectra of the FRET-NPs indicated the presence of both DiD and DiR fluorophores, respectively **(Figure 13A)**. It was estimated that all the FRET-NPs were composed with 1:1 ratio of donor DiD and acceptor DiR **(Table 8)**.

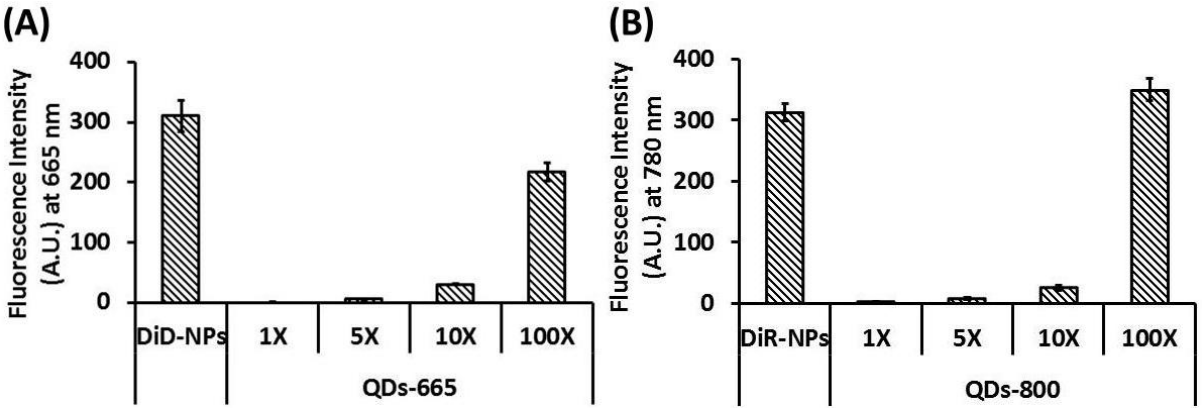

Figure 12. Comparing the fluorescence intensities of the single fluorophore-doped nanoparticles with water soluble quantum dots. A bar chart showing the relative fluorescence intensities of (A) DiD-doped nanoparticles (0.72% w/w, 1×10^{12} particles/mL, 100 µL) and QDs-665 ($1 \times 10^{12\text{-}14}$ particles/mL, 100 µL) and (B) DiR-doped nanoparticles (0.74% w/w, 1×10^{12} particles/mL, 100 µL) and QDs-800 ($1 \times 10^{12\text{-}14}$ particles/mL, 100 µL) in deionized water.

We then compared the optical properties between all the FRET-NPs formulations by recording their absorbance and fluorescence spectra in deionized water **(Figure 13A and B)**. As expected, the absorbance of particles increased with increase in total fluorophore content. Increasing the fluorophore loading from 0.20 to 2.10% w/w resulted in a significant red-shift (24 nm) of the acceptor emission λ_{max} **(Table 9)**. It was found that 0.38% w/w of FRET-NPs was among the brightest **(Table 9)** and similar results were obtained when the recorded FRET intensities were further converted to net FRET (*n*FRET) in order to remove the cross-talk

between the DiD and DiR fluorophores [238]. On the other hand, particles consisting of 2.10% w/w fluorophore content were most efficient for FRET **(Figure 13B)** and the results were also confirmed by the calculated donor-based E_{FRET} (E_D) and acceptor-based E_{FRET} (E_A) values **(Table 9)** [241]. The optimized particles (2.10% w/w) were brighter than QD-800 **(Figure 13D)**, but lost some of the brightness (2.5 times dimmer) when compared to the 0.38% w/w, presumably because of fluorophore self-quenching.

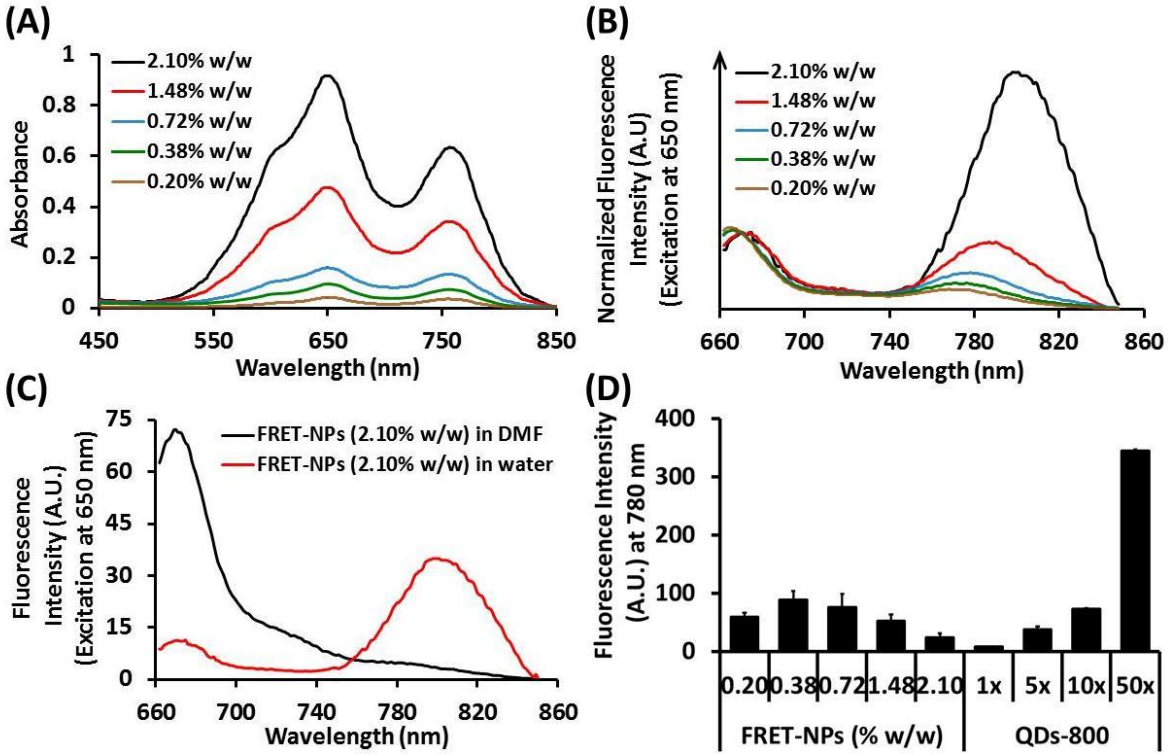

Figure 13. The optical properties of FRET-NPs. (A) The absorption spectra of FRET-NPs (0.20-2.10% w/w) in deionized water (1×10^{12} particles/mL, 100 µL). (B) The emission spectra of FRET-NPs (5×10^{12} particles/mL, 100 µL) in deionized water. All emission spectra were normalized at 666 nm and the excitation and emission slit widths were set at 2.5 and 5 nm, respectively. (C) Emission spectra of FRET-NPs (5×10^{12} particles/mL, 100 µL) after dilution in DMF (Solid) and deionized water (Dotted). (D) Comparison of the *n*FRET intensities of FRET-NPs (0.20-2.10% w/w, 5×10^{12} particles/mL, 100 µL) with the fluorescence intensities of quantum dots ($2.5 \times 10^{12\text{-}14}$ particles/mL, 100 µL) in deionized water.

Table 8. The physical properties of FRET-NPs.

FRET-NPs (% w/w)	*DiD/DiR Ratio*	*Particle Size (nm)*	*Zeta Potential (mV)*	*Polydispersity*	*Total Number of Fluorophores/Particle*
0.20	1:1	64 ± 3	-17.3 ± 2.5	0.18 ± 0.02	213
0.38	1:1	69 ± 4	-17.4 ± 2.0	0.19 ± 0.01	478
0.72	1:1	72 ± 3	-16.8 ± 1.5	0.16 ± 0.03	1065
1.48	1:1	84 ± 5	-16.5 ± 3.9	0.17 ± 0.02	3439
2.10	1:1	93 ± 8	-16.4 ± 0.5	0.16 ± 0.04	6563

To confirm the occurrence of FRET, the particles were further dissolved in DMF and the emission spectra were recorded with excitation at 650 nm. As expected, after decomposition, the FRET emission disappeared **(Figure 13C).** FRET-NPs also consisted of multiple thiol-activated maleimide groups on the surface. Therapeutic molecules such as antibody could be attached to the particles in the future **(Figure 14)**.

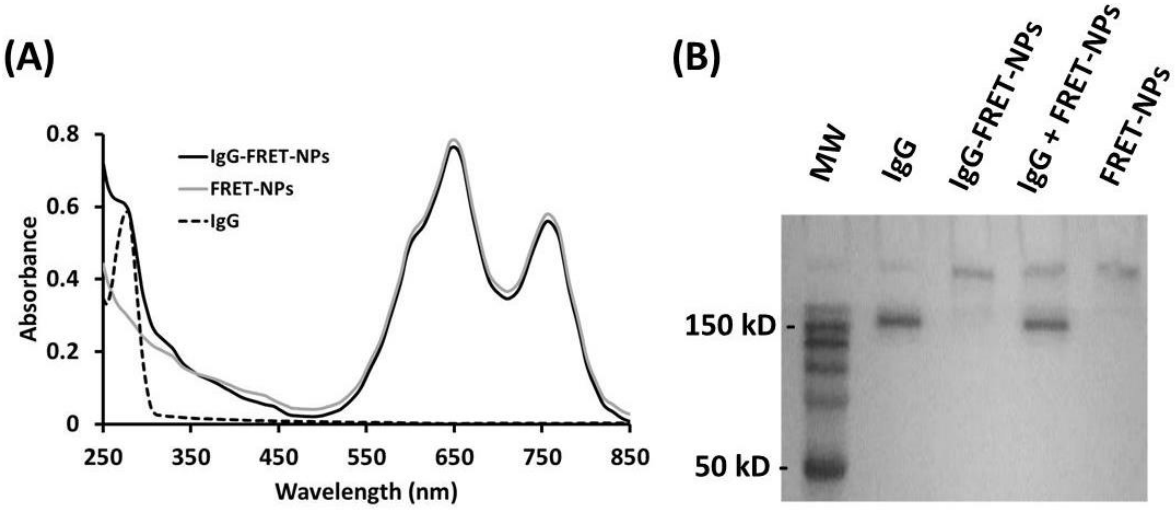

Figure 14. Conjugation of human IgG antibody to the FRET-NPs (2.10% w/w). (A) A comparison of the absorption spectra of free IgG (0.25 mg/mL), FRET-NPs (1×10^{12} particles/mL), and IgG-conjugated FRET-NPs (1×10^{12} particles/mL) in deionized water (100 µL). (B) A SDS-PAGE demonstrating that IgG was covalently attached to IgG-FRET-NPs. The SDS-PAGE gel (15% w/v) was loaded with IgG (2 µg), IgG-FRET-NPs (2 µg), a physical mixture of IgG (2 µg) and FRET-NPs (2 µg), and FRET-NPs only (2 µg). After electrophoresis, the gel was stained with 2% (v/v) Coomassie Blue for 1 h, de-stained overnight in deionized water, and imaged by Fluorchem™ 5500 imaging system (Alpha Innotech, Sanleandro, California).

Table 9. The optical properties of FRET-NPs.

FRET-NPs (% w/w)	***Absorbance λ_{max} (nm)***		***Extinction Coefficient (ε) Per Particle x 10^7 ($M^{-1}cm^{-1}$)***		***FRET λ_{max} (nm)***	***FRET Intensity***	***nFRET***	***R_{FRET}***	***E_{FRET}***	
	λ_{max1}	***λ_{max2}***	***λ_{max1}***	***λ_{max2}***					***E_D***	***E_A***
0.20	651	757	2.55	2.20	771	60 ± 7	34 ± 5	0.14 ± 0.012	0.66	0.47
0.38	651	756	5.77	4.47	776	89 ± 15	57 ± 11	0.22 ± 0.021	0.67	0.91
0.72	649	756	9.60	8.09	778	76 ± 23	50 ± 19	0.29 ± 0.089	0.79	1.25
1.48	649	756	28.7	20.6	790	53 ± 11	40 ± 10	0.70 ± 0.144	0.90	1.70
2.10	649	756	55.3	38.1	795	24 ± 8	20 ± 8	2.25 ± 0.490	0.97	2.30

2.4.6. The stability of FRET-NPs

To examine the long-term stability of FRET-NPs, the particles were monitored by DLS for the changes of physical behavior. FRET-NPs were found stable in deionized water, with no significant changes in both the size and zeta potential for 7 days **(Figure 15A)** [256]. In addition, there was no observable change in the size of FRET-NPs that were kept in PBS only or 10% (v/v) of FBS in MEM media **(Figure 15B)**. However, in the presence of 4.5% (w/v) of BSA in PBS, the particles were slightly increased in the size after 24 h. This could be due to the adsorption of proteins on the particle surfaces.

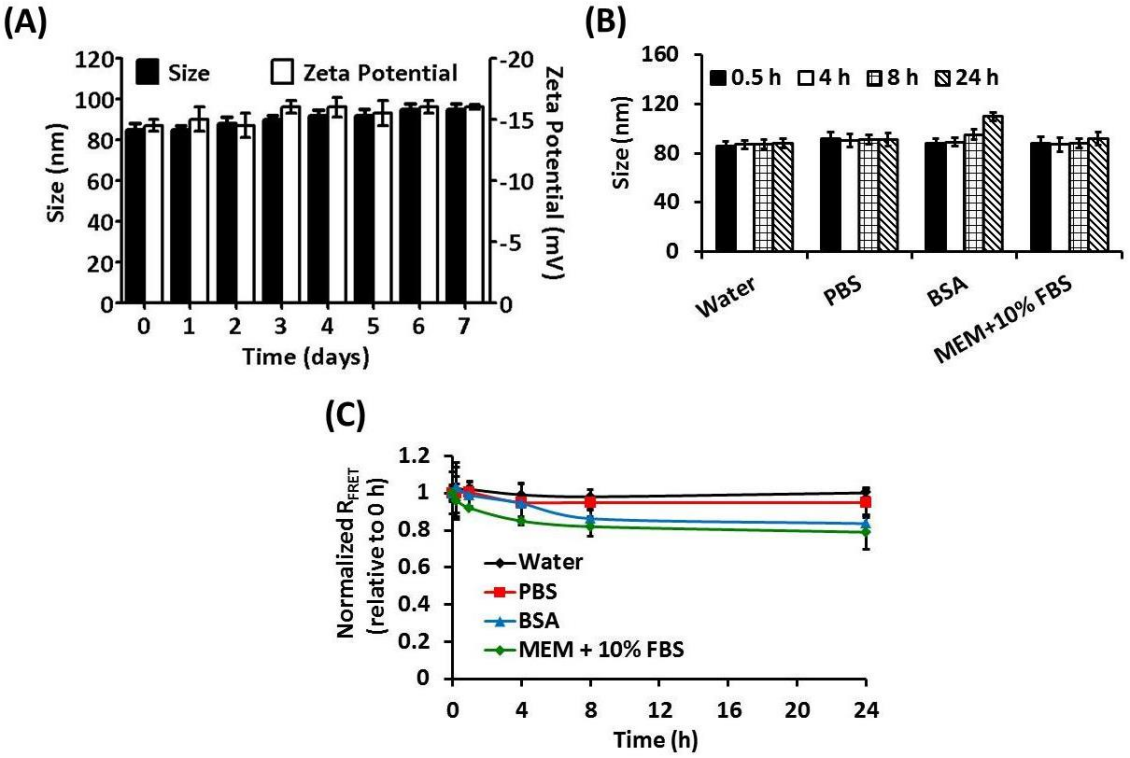

Figure 15. Long term stability testing of FRET-NPs. (A) The colloidal stability of FRET-NPs (1 mg/mL) in deionized water at room temperature. The size (nm) and zeta potential (mV) measurements of the particles over a period of 7 days. (B) A bar chart showing the temporal changes in the size of FRET-NPs (1 mg/mL) in different biological media at 37°C. (C) A comparison of the normalized FRET ratio (Normalized R_{FRET}) of FRET-NPs (0.1 mg/mL) versus time in different biological media at 37°C. The R_{FRET} was normalized according to the corresponding samples at t=0 h.

Similarly, there was a slight decrease in the normalized R_{FRET} stored in 4.5% (w/v) of BSA in PBS or 10% (v/v) of FBS in MEM culture media, which suggested that there might be some leakages of the encapsulated fluorophores from the particles with time **(Figure 15C)**.

2.4.7. Biocompatibility of FRET-NPs

Next, we investigated the biocompatibility of the FRET-NPs using MTS assay **(Figure 16A)**. Mouse leukemic macrophage (RAW 264.7) and human embryonic kidney (HEK-293) cells were used as the model of phagocytic and non-phagocytic cell lines. After 24 h of incubation with FRET-NPs, no significant difference in the cell viability suggested that they were non-toxic.

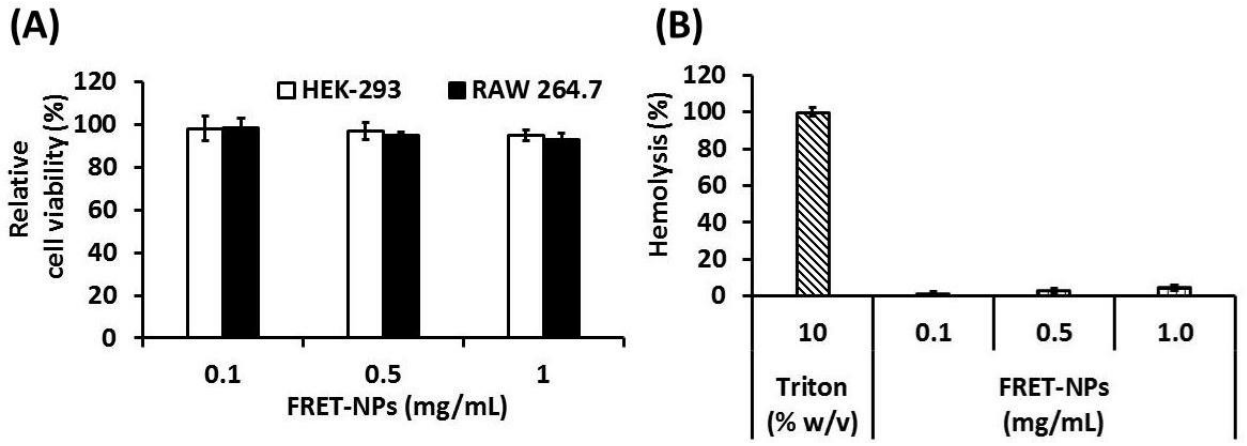

Figure 16. Biocompatibility and hemocompatibility of FRET-NPs. (A) The relative cell viability of RAW 264.7 and HEK-293 cells in the presence of FRET-NPs at 24 h. Cell viability was determined by MTS assay. (B) *In vitro* hemolysis assay. The particles were incubated with the RBCs for 3 h at 37°C and amount of the released hemoglobin was determined by absorbance at 540 nm. The results were expressed as the percentage of hemolysis with respect to the positive control (Triton X-100).

We also investigated the hemocompatibility of FRET-NPs. According to the standard of the American Society for Testing and Materials (ASTM), if the percentage of hemolysis is > 5%,

the material is considered causing damage to red blood cells [246]. Here, the hemolysis assay was performed using isolated erythrocytes from the blood as previously described [246]. Triton X-100 and PBS were used as the positive and negative controls, respectively. The percentage of hemolysis increased in a concentration-dependent manner **(Figure 16B)**, with 4.5% of hemolysis in the sample containing the highest concentration (1 mg/mL) of FRET-NPs. Our results indicated that FRET-NPs did not induce any damage to red blood cells and thus were considered to be hemocompatible.

Table 10. The number of maleimide groups on FRET-NPs before and after reaction with cysteine by using the Ellman's assay.

Nanoparticles	***Before the reaction (nmoL)***	***After the reaction* (nmoL)***
FRET-NPs	23.5	2.3

2.4.8. Biodistribution of FRET-NPs

Next, we studied the biodistribution of FRET-NPs. To prevent the possible interaction of nanoparticles with the serum proteins, the maleimide groups on the particle surfaces were first quenched by reacting with cysteine, prior to injecting the FRET-NPs to the severe combined immunodeficiency (SCID) mice (n=3) by tail-vein injections. Ellman's assay confirmed that nearly 85% of initial maleimide groups were quenched **(Table 10)**. Similar to other nanoparticles, FRET-NPs showed a typical tissue distribution pattern with a majority of uptake in the liver and spleen at 24 h after injection **(Figure 17A)** [257]. The FRET signal in these organs indirectly suggested that FRET-NPs were remaining intact in the body **(Figure 17B and C)**. While not a focus of this study, the length and terminal functional groups of PEG chains could be varied to bypass the uptake from the reticuloendothelial system in the future [11].

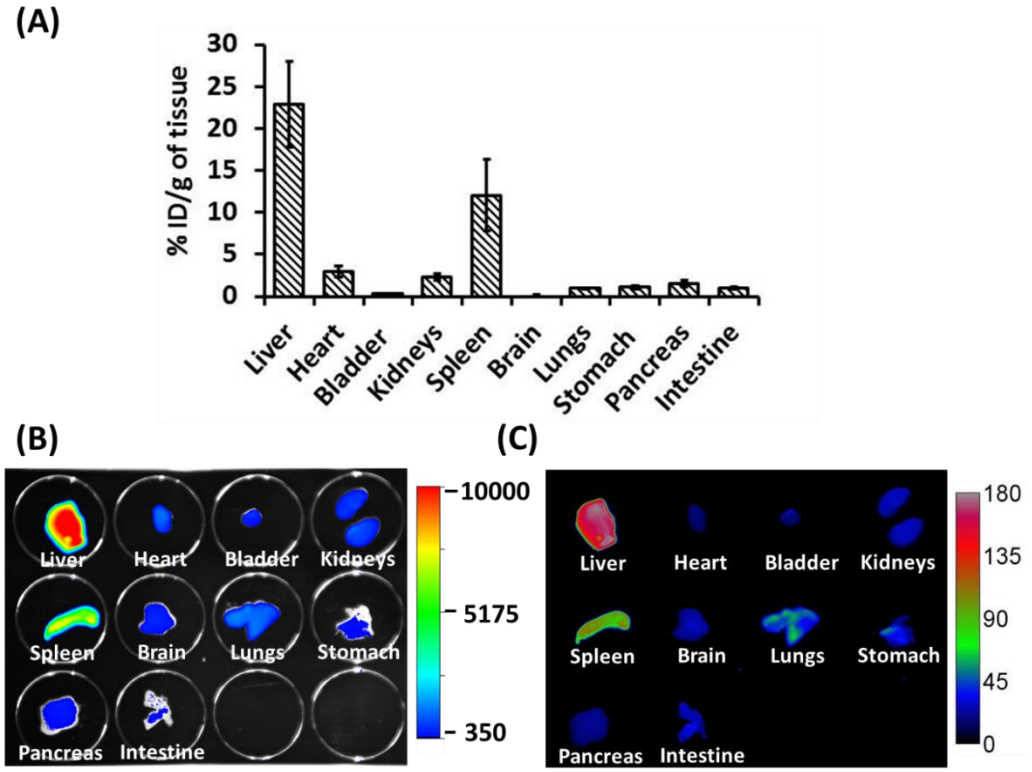

Figure 17. Biodistribution of the FRET-NPs in SCID mice. (A) A bar chart showing the organ distribution at 24 h after intravenous administration of FRET-NPs (5×10^{12}/mL) in sterile PBS (100 µL) to the SCID mice (n=3, mean ± SEM). The (B) raw and (C) *n*FRET images of isolated organs. The mice were injected with the same number of FRET-NPs (5×10^{12}/mL) in sterile PBS (100 µL) *via* tail-vein.

2.4.9. Phantom studies

Prior to administration of FRET-NPs in a preclinical animal model for imaging, phantom studies were performed to evaluate their efficacy as an imaging agent. An animal phantom was constructed to simulate the tissue fluorescence while imaging. The phantom was composed with a capillary tube was pre-filled with FRET-NPs, DiR-doped nanoparticles, or QDs-800 in deionized water, that was inserted into the thoracic region of a SCID mouse *via* its mouth **(Figure 18)**. FRET-NPs consisting of 2.10% w/w fluorophore content were chosen in this study. These particles had the highest FRET efficiency **(Table 9)** and thus were considered more applicable for FRET imaging. In the present study, both the raw FRET image of FRET-NPs and

NIRF image of DiR-doped nanoparticles showed the similar brightness and signal-to-phantom background ratio (1:11) and were also more sensitive than the QDs-800 **(Figure 18)**. Our results indicated that FRET-NPs had no advantage over the DiR-doped nanoparticles alone in terms of the detection sensitivity and the ability to increase the contrast between the tested sample and the animal. However, when the FRET signal was converted into *n*FRET as previously described [238], the processed image of the FRET-NPs showed significant improvement of the signal-to-phantom background ratio (from 1:11 to 1:39), presumably as a result from removing the fractional cross-talk of the fluorophores and reducing the background contributed by the phantom **(Figure 18)**. Similar results were also obtained when agarose was used to substitute as the phantom **(Figure 19)**. Overall, our results suggested that FRET-NPs can be used for time-resolved imaging in the future, which will further improve the spatial and temporal resolution, by discriminating against light scattering, reflection, auto-fluorescence, and extraneous prompt fluorophores [258].

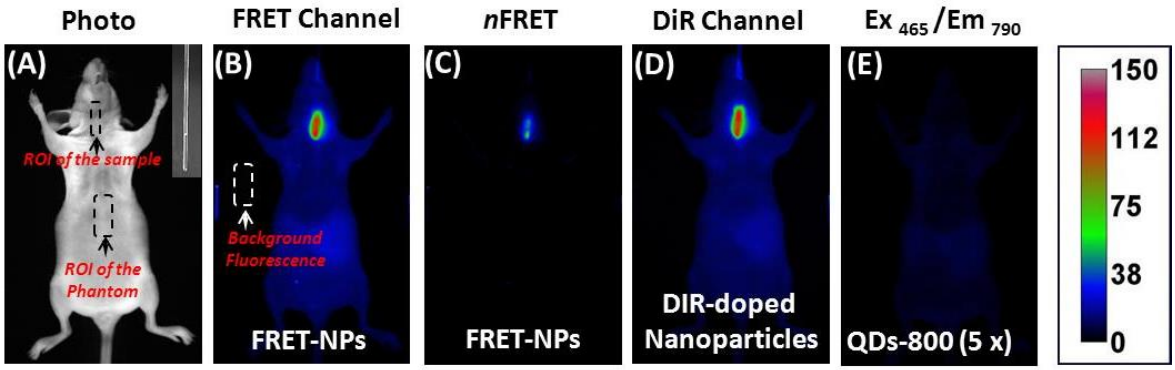

Figure 18. Phantom studies in SCID mice. The (A) photo, (B) FRET, and (C) *n*FRET images of a mouse inserted with a glass capillary tube (1.1 × 90 mm) that was filled with FRET-NPs in deionized water (5×10^{12} particles/mL, 10 µL). The fluorescence images of a mouse that was inserted with (D) DiR-doped nanoparticles (5×10^{12} particles/mL, 10 µL) and (E) QDs-800 (2.5×10^{13} particles/mL, 10 µL). For the data analysis, all the images were corrected for the corresponding background fluorescence. The signal-to-phantom background ratio was determined by dividing the signal intensity of the samples with the phantom at the region of interests (ROIs).

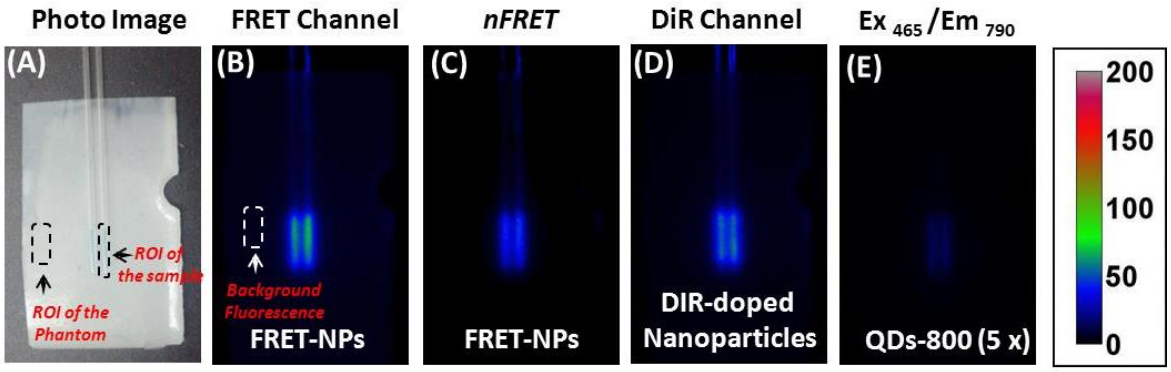

Figure 19. Phantom studies using agarose phantom. The (A) photo, (B) FRET, and (C) *n*FRET images of two glass capillary tubes (1.1 × 90 mm) filled with FRET-NPs (5×10^{12}/mL, 10 µL). The tubes were placed on top of a 3% w/v agarose phantom (5 × 3 × 0.15 cm) that was constructed as previously described [259]. The fluorescence images of a phantom consisting of (D) DiR-doped nanoparticles (5×10^{12}/mL, 10 µL) and (E) QDs-800 (2.5×10^{13}/mL, 10 µL).

2.5. Conclusion

Numerous types of near-infrared (NIR) fluorescent materials such as organic fluorophores [73], rare-earth emitters [260], quantum dots [199], gold nanoparticles [261], long circulating polymers with tagged fluorophore [262], and fluorescent proteins [263] have been employed for *in vivo* imaging. However, there is only a limited number of FRET-based contrast agents developed for *in vivo* NIR imaging. In the present study, we investigated polymeric nanoparticles that composed of PLGA-PEG_{3500}-maleimide copolymers as a fluorophore carrier and DiD and DiR fluorophores as the FRET pair. The particles (FRET-NPs) were synthesized by the nanoprecipitation method. The energy transfer was found more efficient in particles that consisted of higher fluorophore contents. The optimized FRET-NPs were brighter than the quantum dots, stable in biological media, and hemocompatible. Most importantly, the energy transfer from DiD (donor) to DiR (acceptor) fluorophore resulted in a large Stokes shift (> 100 nm) between the excitation and emission maxima. Similar to other nanoparticles, FRET-NPs revealed the expected tissue distribution in mice model. For proof-of-principle, an animal

phantom was also constructed to demonstrate the potential imaging application of FRET-NPs. Our results showed that simply by applying equation (11) during image processing would significantly improve the signal-to-phantom background ratio.

CHAPTER 3. POLYMERIC NANOPARTICLES WITH SEQUENTIAL AND MULTIPLE FRET CASCADE MECHANISMS FOR MULTICOLOR AND MULTIPLEXED IMAGING*

**Published in Small, Volume 9, Issue 12, pages 2129–2139, 2013, DOI: 10.1002/smll.201202655)* *(Copyright © 2013 WILEY-VCH Verlag GmbH & Co. KGaA, Weinheim)*

3.1. Abstract

The ability to map multiple biomarkers at the same time has far-reaching biomedical and diagnostic applications. Here, we report a series of biocompatible poly(D,L-lactic-*co*-glycolic acid) and polyethylene glycol particles for multicolor and multiplexed imaging. More than 30 particle formulations that exhibited distinct emission signatures (ranging from the visible to near-infrared wavelength region) were designed and synthesized. These particles were encapsulated with combinations of carbocyanine-based fluorophores, DiO, Dil, DiD, and DiR, and were characterized as <100 nm in size and brighter than commercial quantum dots. We identified (1) a particle formulation that simultaneously emitted fluorescence at three different wavelengths upon a single excitation at 485 nm (*via* sequential and multiple FRET cascade events) for multicolor imaging and (2) three other particles that displayed maximum fluorescence intensity at 570, 672, or 777 nm for multiplexed imaging. These particles were individually conjugated with specific (Herceptin or IgG2A11 antibody) or non-specific (heptaarginine) ligands for targeting and, thus, could be applied to differentiate different cancer cells from a cell mixture according to the expressions of cell-surface human epidermal growth factor receptor 2 and the receptor for advanced glycation endproducts. Using an animal model subcutaneously implanted with the

optimized particles, we further demonstrated that our developed platform could be useful for *in vivo* multiplexed imaging.

3.2. Background

A pool of nanoparticles that individually process distinct emission signature (when excited at the same wavelength) can be a useful tool for multiplexed bioassay and imaging [264]. In the past, many nanoparticle platforms have been tailored for *in vitro* applications including multiplexed bioassay [265], cell labeling [266], detection of cancer cells [214], and monitoring of bacteria [213]. Among all of these, quantum dots (QDs) were the most commonly used ones because of their broad excitation spectra and size-dependent tunable emission wavelengths [267, 268]. For example, QDs with distinct luminescence emissions have been used to simultaneously visualizing various subcellular structures and multiple molecular markers in a single cancer cell [269, 270]. By combining six colored QDs, a library of one million optically encoded polymeric microbeads were generated for parallel and high throughput analysis [264]. Apart from these applications, QDs have also shown great potential as a multiplexed imaging probe *in vivo*. In one study, five different colored QDs were used for the simultaneous visualization of five distinct lymphatic basins in the neck and axillary region in mice [271]. In another study, QDs were evaluated for *in vivo* multiplex imaging of mouse embryonic stem cells [272]. Despite these successful attempts, the cumbersome synthetic procedures, sporadic blinking, and the unsure long-term toxicity often hinder their *in vivo* applications [273, 274].

Nanoparticles assembled from other materials such as silica, polystyrene, and gold have also been explored for multiplexed applications [204, 275, 276]. These particles were often designed with the encapsulation of more than two different but complementary organic and/or

inorganic fluorophores, in order to create a fluorescence resonance energy transfer (FRET) cascade upon excitation [204, 205]. With such design, a desired emission signature could be fine-tuned by changing the choice, the amount, and the ratio of the fluorescence entities [204, 205]. For example, silica nanoparticles encapsulated with fluorescein and a variety of rhodamine analogues have been used for simultaneous monitoring of multiple bacteria or cancer cells [213, 214]. Polymeric nanospheres co-encapsulated with phosphorescent ruthenium metal-ligand complex and cyanine derivatives were applied to time-resolved multiplexed bioassays [215]. The advantage of this approach is that the particles can provide an optimal environment to enhance the brightness of the fluorophores [145]. Furthermore, the consequence of FRET cascade could further increase the Stokes Shift of the emission maxima and thus significantly minimize the crosstalk between the excitation and emission spectra [277].

We have recently reported fluorophore-doped poly(D,L-lactic-*co*-glycolic acid) and polyethylene glycol (PLGA-PEG) nanoparticles for FRET and NIR imaging [278]. These particles were nontoxic, photo-stable, and brighter than QDs. In the present study, we further synthesized more than 30 particles with diverse emission patterns, ranging from the visible to near-infrared (NIR) wavelength region (500 to 790 nm), for multicolor and multiplexed imaging. These particles were encapsulated with a combination of four lipophilic carbocyanine fluorophores, including 3,3'-dioctadecyloxacarbocyanine (DiO), 1,1'-dioctadecyl-3,3,3',3'-tetramethylindocarbocyanine (Dil), 1,1'-dioctadecyl-3,3,3',3'-tetramethylindodicarbocyanine (DiD), and 1,1'-dioctadecyl-3,3,3',3'-tetramethylindotricarbocyanine (DiR). Simply by changing the amount as well as the ratio of the doped fluorophores, the optical property of the particles could be fine-tuned to display distinct or multiple emission λ maxima (λmax). We further selected three of the optimized formulations and utilized them as a multiplexed imaging

platform. Each of the particles exhibited a distinct emission maximum at 570, 672, or 777 nm. By attaching targeting antibodies (including Herceptin and IgG2A11) to individual particles, we demonstrated that the combined multiplexed platform could be applied for imaging the human epidermal growth factor receptor 2 (HER2) and receptor for advanced glycation endproducts (RAGE) simultaneously in a mixture of breast cancer (SK-BR-3) and melanoma (WM-115-RAGE) cell lines. Here, multiple transduction domains (RRRRRRRC) were also attached to one of the particles for cell labeling.

3.3. Experimental procedures

3.3.1. Chemicals and materials

All solvents were purchased from Fischer Scientific (Pittsburgh, PA). Poly(D,L-lactic-*co*-glycolic acid) (PLGA-COOH, monomer ratio 50:50, 17 kDa) was received as a gift sample from PURAC Biomaterials (Netherland). Maleimide-activated PEG (Mal-PEG_{3500}-NH_2, 3.5 kDa) was purchased from JenKem Technology USA, Inc. (Allen, TX). Uranyl acetate and formvar/carbon coated grids (200 mesh) were obtained from Electron Microscopy Sciences (Hatfield, PA) and SPI Supplies/Structure Probe, Inc. (West Chester, PA), respectively. Trilite™ fluorescent nanocrystal 665 nm (QDs-665) was purchased from Cytodiagnostics, Inc. (Burlington, Ontario). DiO, Dil, DiD, DiR, Hoechst 33342, and Qdot® 800 ITK™ carboxyl quantum dots (QDs-800) were obtained from Life Technologies Corporation (Grand Island, NY). *N*-hydroxysuccinimide (NHS) and 9,10-phenanthrenequinone were obtained from Alfa Aesar (Ward Hill, MA). 1-ethyl-3-(3-dimethylaminopropyl) carbodiimide (EDC) and *N*,*N*-diisopropylethylamine (DIEA) were purchased from Advanced ChemTech (Louisville, KY) and Sigma-Aldrich (St. Louis, MO), respectively. Herceptin antibody was purchased from Genentech, Inc. (South San Francisco,

CA). The IgG2A11 antibody was a generous gift from Dr. Estelle Leclerc. Heptaarginine peptide (RRRRRRRC) was custom synthesized at Tufts Medical School (Boston, MA).

3.3.2. Synthesis of PLGA-PEG copolymer

The PLGA-PEG-Mal copolymer was synthesized by reacting poly(D,L-lactic-*co*-glycolic acid) carboxylic acid (PLGA-COOH) with maleimide-activated poly(ethylene glycol) (Mal-PEG_{3500}-NH_2), employing the standard carbodiimide chemistry, as previously described [164, 278]. After synthesis, the copolymer was purified and dried under vacuum to remove the residual solvents. The resulting PLGA-PEG-Mal was characterized by ^{1}H-NMR spectroscopy [278].

3.3.3. Synthesis of nanoparticles

All the nanoparticles were prepared in an aqueous environment by the nanoprecipitation method [164]. Briefly, the PLGA-PEG-Mal copolymer (1 mg) together with different amounts and ratios of DiO, Dil, DiD, and DiR fluorophores were dissolved in DMF (100 µL) and then added dropwise to deionized water (1 mL). The resulting nanoparticle suspensions were allowed to stir for 2 h at room temperature, and the organic solvent was removed by ultracentrifugation (3000 × *g*, 15 min) using SPIN-X UF concentrator with a 10 kDa MWCO (Corning Incorporated, Lowell, MA). The samples were purified by washing with deionized water (2 × 1 mL). The purified nanoparticles were resuspended in deionized water (100 µL) and stored in the dark at 4°C.

3.3.4. Physical characterization of nanoparticles

The size (hydrodynamic diameter) and zeta potential of the nanoparticles were measured by dynamic light scattering (DLS) using a Zetasizer (Malvern Instruments, Worcestershire, U.K.) equipped with a dynamic light scattering detector (5 mW laser, incident beam 633 nm), as previously described [278]. The nanoparticles (0.3 mg/mL) were suspended in deionized water (1 mL), and the intensity-weighted mean values were recorded as the average of three independent measurements.

3.3.5. Transmission electron microscopy (TEM)

A drop of particle suspension (0.5 mg/mL) in deionized water was adsorbed on to 200 mesh formvar/carbon coated grids for 2 min, and the excess sample was blotted by using a filter paper. All the samples were then negatively stained with freshly prepared 2% (w/v) uranyl acetate in deionized water (10 µL) for 1 min. The grids were washed with deionized water and then air-dried. The images were acquired by transmission electron microscope (JEOL 100CX, JEOL USA, Inc. Peabody, MA).

3.3.6. Determination of the particle brightness

The brightness levels of T3 and M5 were compared with the corresponding commercial water-soluble QDs, QDs-665 and QDs-800, respectively, using a spectrofluorometer (Cary Eclipse, Agilent Technologies, Inc., Santa Clara, CA). The same numbers of particles (5×10^{11}/mL) were diluted in deionized water (100 µL). For the ease of comparison, QDs with three different particle concentrations ($2.5\text{-}5 \times 10^{11\text{-}12}$/mL) were prepared. The fluorescence spectra of

all the particles were recorded upon excitation at 485 nm. I_{FRET} was referred to the fluorescence intensity of the acceptor (at λmax) upon excitation of the donor (at λmax).

The brightness of the particles (5×10^{11}/mL) was also compared with the QDs using a reflectance imaging system (*In vivo* system FX, Carestream Health, Inc., Rochester, NY), as previously described [243, 254]. The particles (5×10^{11}/mL) suspended in deionized water (100 µL) were added to the wells of a clear-bottom 96-wells black plate (Corning Incorporated, Lowell, MA). The plates were exposed to the excitation light source equipped with an excitation band-pass filter for DiO (445-485 nm). The images were acquired using the corresponding emission band pass filters for DiD (680-720 nm) and DiR (770-810 nm). All the images were acquired with a single exposure time of 5 min and were further analyzed using the Kodak molecular imaging software (Carestream Health, Inc., Rochester, NY).

3.3.7. Synthesis of thiolated antibody

The free amino groups of the antibody were converted into sulfhydryl groups by using Traut's reagent [278]. Briefly, excess 2-iminothiolane (1 mM, 6.7 µL) was added to the antibody (6.7 µM, 100 µL) in PBS buffer (10 mM, pH 8.0) containing ethylenediaminetetraacetic acid (10 mM). After 2 h, the thiolated antibody was further washed and purified by ultracentrifugation (3000 × *g*, 15 min) using SPIN-X UF concentrator with a 10 kDa MWCO (Corning Incorporated, Lowell, MA).

3.3.8. Conjugation of targeting ligands

The targeting ligands were conjugated to the nanoparticle surfaces employing the thiol-maleimide chemistry [279]. The thiolated antibody (50 µg) or RRRRRRRC peptide (50 µg) was

added to the maleimide-activated nanoparticles (500 µg) in PBS buffer (200 µL, 10 mM, pH 8.0) and allowed to react for 2 h at room temperature. The unreacted maleimide groups of nanoparticles were neutralized by the addition of cysteine (50 µg) in the reaction mixtures, and further incubated for 30 min at room temperature [278]. The resulting particles were purified by size exclusion chromatography (Sephacryl-300 HR, GE Healthcare, Piscataway, NJ), using PBS buffer (10 mM, pH 7.4) as an eluent. The successful conjugation of the peptide and antibody was confirmed by the absorbance at 205 and 280 nm, respectively, by UV-visible spectroscopy. The successful quenching of free maleimide groups was confirmed by the quantification of unreacted cysteine using Ellman's reagent, as previously described [278].

3.3.9. Determination of the number of targeting ligands

The total number of nanoparticles (*N*) in stock solution was determined by using the following equation [278].

$$N = \frac{6c}{\pi \times d^3 \times \rho_P} \quad \text{(16)}$$

Where c is the polymer concentration, d is the hydrodynamic diameter of particles determined by dynamic light scattering, and ρ_p is the density of PLGA nanoparticle core (estimated to be 1.27 g cm^{-3} at 20°C).

The amount of antibodies conjugated to the particles was determined by microBCA assay (Thermo Fisher Scientific, Inc., Rockford, IL). Briefly, the antibody-conjugated particles (1 mg/mL) in PBS buffer (150 µL) were mixed with bicinchoninic acid (BCA) reagent (150 µL) and then incubated for 2 h at 37°C. The unmodified nanoparticles were used as a blank. The samples were cooled to room temperature in order to measure the absorbance at 562 nm. The

corrected absorbance was converted into the actual amount according to a standard curve prepared by using known concentrations of albumin standards (1-160 µg/mL).

The amount of peptides conjugated to the particles was determined by measuring the arginine content [280]. Briefly, the peptide-conjugated particles (1 mg/mL) in PBS buffer (50 µL) were mixed with 9,10-phenanthrenequinone (30 µg/mL) in ethanol (150 µL) and NaOH (2N, 25 µL) and then incubated for 3 h at 60ºC. An equal volume of HCl (1.2 N, 200 µL) was added to the reaction mixture (200 µL), which was then incubated for 1 h at room temperature. The fluorescence intensity at 395 nm was recorded upon excitation at 312 nm. The amount of the peptide was quantified according to a standard curve generated by using known concentrations of free peptide (1-20 µg/mL).

The number of targeting ligands in the solution was then determined by multiplying the amount of the antibody or peptide (nmoL) by Avogadro's number. Finally, the number of targeting ligands per nanoparticle (*n*) was calculating using the following equation:

$$n = \frac{\text{Total number of targeting ligands}}{N} \quad \text{(17)}$$

3.3.10. Estimation of distance between fluorophores

The average distance between the fluorophores in solution and inside particles was estimated by using the following equations, as previously described [281].

$$V_F = \frac{1.66}{C} \quad \text{(18)}$$

$$d = \sqrt[3]{V} \quad \text{(19)}$$

Where V_F is volume of a single fluorophore (nm^3), C is concentration (M), and d is average separating distance (nm).

The volume of a single fluorophore inside nanoparticles was estimated using the following equation:

$$V_F = \frac{V_T}{n_F} \quad (20)$$

Where V_T is the total volume of a single particle (nm^3) and n_F is the estimated total number of fluorophores in a single particle, as previously described [278].

3.3.11. Lifetime measurements

All the fluorescence lifetime measurements were performed on a fluorescence-lifetime instrument obtained from Photon Technology International (PTI). The light emitting diodes (LEDs) with the power output at 495 nm was used as a excitation source and emitted light was detected at an 90°c angle using a emission monochromator set at 505 nm. A total of 10000 photon counts were collected. The contribution of the instrument response function (Prompt) was corrected from the fluorescence decay curves of nanoparticles. The corrected decay curves were fitted in two-exponential model to obtain the individual lifetime (T_1 and T_2) with their relative amplitude (β_1 and β_2) of the individual samples. The global average lifetime was obtained by the following the equation.

$$Global\ average\ lifetime\ (T) = \frac{(T_1\beta_1) + (T_2\beta_2)}{\beta_1 + \beta_2} \quad (21)$$

3.3.12. Fluorescence microscopy

The SK-BR-3 cancer cell line was obtained from the American Type Culture Collection (ATCC, Manassas, VA). The cells were grown in culture media supplemented with 10% (v/v) fetal bovine serum (FBS), penicillin (50,000 units/L), and streptomycin (50 mg/L), as recommended by ATCC and maintained in 5% CO_2 at 37°C under humidified conditions. The WM-115-RAGE cell line was maintained in an Opti-MEM medium supplemented with FBS (4% v/v), penicillin (100,000 units/L), streptomycin (100 mg/L), and G418 (0.1% w/v). For microscopic study, the cells (3000/well) were seeded on a 4-chambers slide (Thermo Fisher Scientific, Inc., Rockford, IL). After 12 h, the same number of particles (9×10^{11} /mL) were added to the cells in a phenol red free culture medium (400 μL) and allowed to incubate for 15 min. Hoechst 33342 (2 μg/mL) was added to all the samples for nuclear staining 10 min prior to imaging. The cells were washed and then imaged under a fluorescence microscope (Olympus IX-81, Olympus America, Inc., Melville, NY). A metal cube (Semrock, Inc., Rochester, NY) that was assembled with the appropriate excitation and emission band pass filters was employed. To acquire FRET images, the excitation band pass filter for DiO (460-500 nm) and one of the following emission band pass filters for Dil (525-574 nm), DiD (635-675 nm), and DiR (754-816 nm) were manually assembled into the cube (Semrock, Inc., Rochester, NY). Images were recorded by a CCD camera (Hirakuchi, Hamamatsu, Japan) interfaced with a computer and were processed using HCImage software (Hamamatsu Corporation, Bridgewater, NJ).

3.3.13. MTS assay

The MTS assay was performed as previously described [245, 282]. The cancer cells (5000/well) were seeded in a clear bottom 96-wells plate (Corning Incorporated, Lowell, MA).

After 12 h, different amounts (10-500 µg) of the particles suspended in culture medium (100 µL) were added to the cell lines at 37°C. Cells incubated with sterile PBS buffer served as a negative control. After 24 h of exposure, fresh media containing the MTS reagent (Promega Corporation, Madison, WI) were added to each well and further incubated for 1 h at 37°C. The formation of formazan dye was measured by absorbance at 490 nm ($A_{Particle}$). The results were corrected from the intrinsic absorbance of particles at 490 nm ($A_{Background}$). The percentage of cell viability was determined by using the following equation:

$$(A_{Particle-} A_{Background})/(A_{PBS}) \times 100\% \quad (22)$$

3.3.14. *In vivo* imaging studies

All animal experiments were performed according to the guidelines of the Institutional Animal Care and Use Committees (IACUC) at NDSU. Four- to five-week old female severe combined immunodeficiency (SCID) hairless outbred (SHO-*Prkdc*^{scid}*Hr*^{hr}) mice (20 g) were purchased from Charles River Laboratories (Wilmington, MA) and maintained in a pathogen-free and temperature-controlled environment. For the imaging studies, the mice (n=3) were first anesthetized by intraperitoneal injection of ketamine (90 mg/kg) and phenobarbital (5 mg/kg) and then injected with the same number of fluorophore-doped nanoparticles (3.5×10^{11}) or quantum dots ($3.5 \times 10^{11\text{-}12}$) in deionized water (10 µL) *via* subcutaneous route. Whole-body FRET imaging was performed by using a reflectance imaging system (In-vivo system FX, Carestream Health, Inc., Rochester, NY) [278]. All the FRET images were acquired using the same excitation band-pass filter for DiO (445-485 nm). The emitted light was collected using one of the following emission band pass filters for Dil (580-620 nm), DiD (680-720 nm), and DiR (770-810 nm). All the images were collected with a single exposure time of 1 min and were

processed by using Kodak molecular imaging software (Carestream Health, Inc., Rochester, NY). The signal-to-noise ratio (SNR) was calculated by dividing the average signal intensity of the particles at the injection site by the background of the mouse at the same region of interest (ROI).

3.4. Results and discussion

3.4.1. Design and synthesis of the particles

All the particles were assembled from PLGA-PEG-Mal diblock copolymers, which were synthesized by reacting carboxylic acid-terminated poly(D,L-lactic-*co*-glycolic acid) (PLGA-COOH) with maleimide-activated amino polyethylene glycol (Mal-PEG_{3500}-NH_2), using the carbodiimide chemistry [278]. The reaction was confirmed by ^1H NMR, as previously described [278]. Previous studies have been shown that, in aqueous media, the PLGA segments of the copolymers would agglomerate into a hydrophobic core, which might serve as a reservoir for carrying different therapeutic and imaging agents such as cisplatin, docetaxol, and indocyanine green [280, 283, 284]. Each assembled particle was also surrounded by a sheath of hydrophilic PEG and thereby expose multiple terminal maleimides at the surface for bioconjugation of the targeting ligand [164]. The PEG coating was able to minimize the aggregation upon storage and also helped to improve the circulation time *in vivo* [163]. By using this approach, we designed a series of nanoparticles with tunable emission signatures for multicolor and multiplexed imaging **(Figure 20A and B)**. The particles were encapsulated by a combination of four carbocyanine fluorophores, with each of them attaching to a lipophilic alkyl tail (C_{18}) at the imine nitrogen. Thereby, hundreds to thousands of molecules could be entrapped inside a single particle for safeguarding an efficient FRET [227].

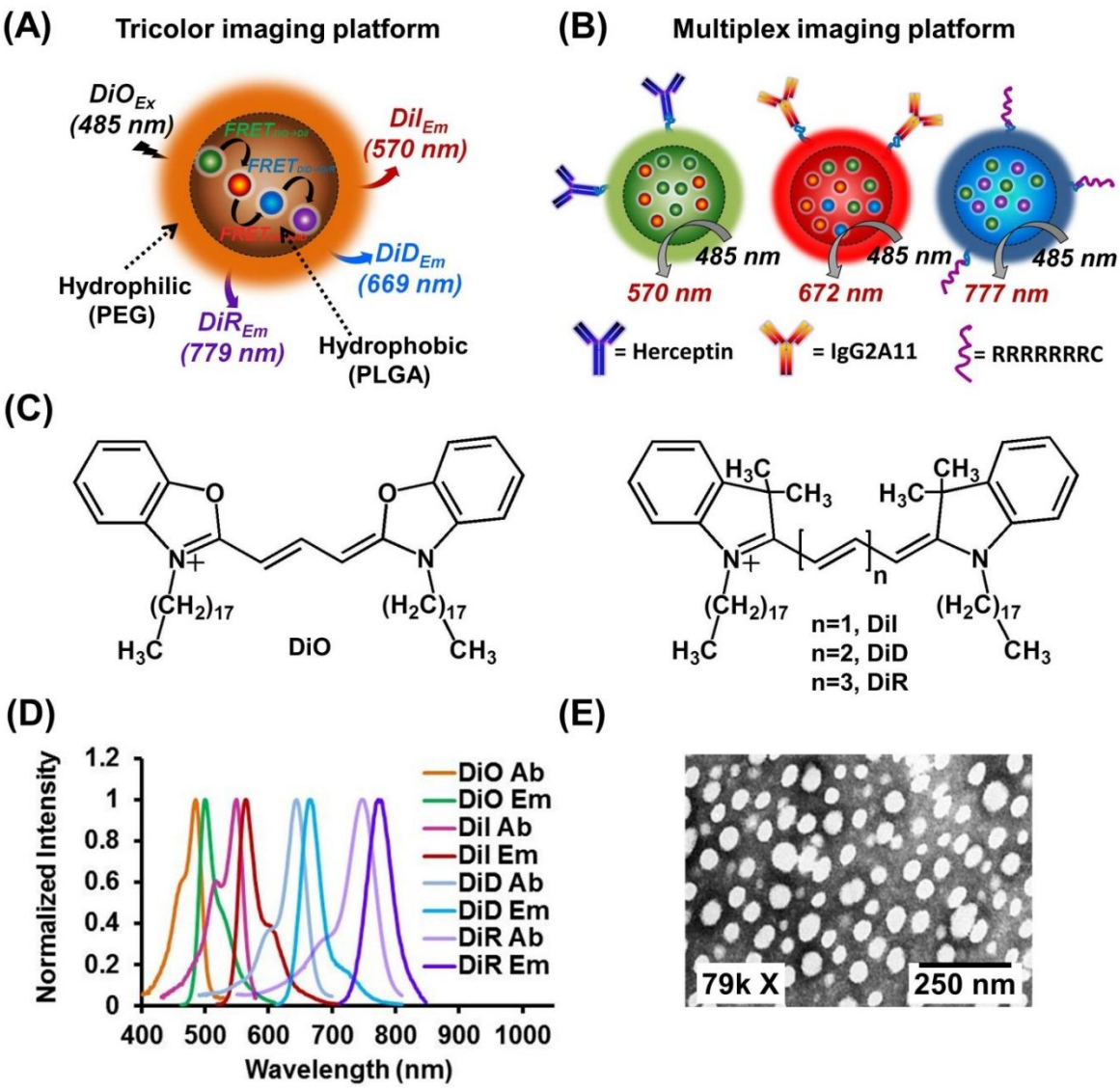

Figure 20. Design and characterization of nanoparticles. A schematic representation of particles designed for (A) multicolor and (B) multiplex imaging. (C) The chemical structures of DiO, Dil, DiD, and DiR. (D) A comparison of the normalized absorption and fluorescence emission spectra among the fluorophores in methanol. (E) A TEM image of Q7. The samples were negatively stained with 2% (w/v) uranyl acetate in deionized water.

The differences among the fluorophores are the heterocyclic ring and the length of the polymethine bridge **(Figure 20C).** The heterocyclic structure offered the high extinction coefficient to the fluorophore, whereas the polymethine determined the absorption and emission λmax [234, 285]. Because of the distinct and overlapping excitation and emission spectra of the

fluorophores **(Figure 20D)**, sequential FRET was prompted to occur when they were encapsulated inside the particle [227, 278].

3.4.2. Particles doped with two fluorophores

The particles were prepared by dissolving the fluorophores along with the PLGA-PEG copolymer in anhydrous DMF and then co-precipitated them in deionized water. The surface morphology and the size distribution of the resulting particles were confirmed by transmission electron microscopy (TEM) **(Figure 20E)**. FRET is proportional to an inverse sixth power of the distance between donor and acceptor fluorophores [278, 286]. On the contrary, encapsulating a large number of fluorophores inside a polymeric particle could lead to fluorescence self-quenching [145, 278]. Therefore, we first determined an optimum fluorophore loading that favored an efficient FRET compromised with a minimum loss of brightness of the particles. D1-D7 were prepared by encapsulating the same ratio but different amounts (0.09 to 3.0% w/w) of DiO and Dil inside the particles. We observed that the average particle size of the resulting particles was 55 ± 9 nm (n=200) under the TEM **(Figure 20E)**. Due to the presence of a hydration layer around the particles in aqueous media [287], the particles appeared to be slightly larger (75 ± 10 nm) when analyzed by dynamic light scattering **(Table 11)**. Here, all the particles possessed the same zeta potential (-18 ± 5 mV), providing evidence that the fluorophores were trapped inside the hydrophobic core.

Table 11. The physical properties of two-fluorophores doped nanoparticles.

NPs	*Total Fluorophore Loading (% w/w)*	*DiO:Dil:DiD:DiR Ratio*	*Size (nm)*	*Polydispersity*	*Zeta Potential (mV)*
D1	0.09	1:1:0:0	66 ± 1.0	0.109 ± 0.01	-19 ± 1.4
D2	0.21	1:1:0:0	72 ± 1.0	0.175 ± 0.04	-20 ± 0.5
D3	0.40	1:1:0:0	75 ± 2.9	0.166 ± 0.03	-18 ± 1.0
D4	0.80	1:1:0:0	77 ± 1.8	0.140 ± 0.01	-17 ± 0.5
D5	1.40	1:1:0:0	80 ± 7.7	0.163 ± 0.04	-19 ± 0.6
D6	2.10	1:1:0:0	88 ± 7.2	0.175 ± 0.02	-17 ± 0.5
D7	3.00	1:1:0:0	107 ± 2.0	0.174 ± 0.01	-19 ± 0.5

Table 12. The optical properties of two-fluorophores doped nanoparticles

NPs	*Absorbance λmax (nm)*				*FRET Emission λmax (nm)*			$I_{FRET(DiO \rightarrow Dil)}$ *(A.U.)*	$I_{FRET(DiO \rightarrow DiD)}$ *(A.U.)*	$I_{FRET(DiO \rightarrow DiR)}$ *(A.U.)*
	λmax_1	λmax_2	λmax_3	λmax_4	*DiO→Dil*	*DiO→DiD*	*DiO→DiR*			
D1	488	553	N/A	N/A	565	N/A	N/A	28 ± 2	N/A	N/A
D2	487	553	N/A	N/A	566	N/A	N/A	75 ± 9	N/A	N/A
D3	486	553	N/A	N/A	567	N/A	N/A	121 ± 1	N/A	N/A
D4	486	555	N/A	N/A	568	N/A	N/A	154 ± 9	N/A	N/A
D5	486	555	N/A	N/A	569	N/A	N/A	185 ± 5	N/A	N/A
D6	485	555	N/A	N/A	570	N/A	N/A	233 ± 25	N/A	N/A
D7	485	556	N/A	N/A	579	N/A	N/A	283 ± 14	N/A	N/A

To compare the FRET among the particles, we suspended the same number of D1-D7 in deionized water and then recorded their absorption and emission spectra. The presence of absorption maxima at 485 and 555 nm indicated that the fluorophores were encapsulated inside the particles **(Figure 21A)**. When compared to the free DiO and Dil in methanol, there was a blue and a red shift of the absorption and emission λmax, respectively **(Table 12)**, mainly because the fluorophores were facing a different environment. The two emission λmax that appeared at 505 and 570 nm upon excitation at 485 nm corresponded to the DiO and Dil emissions, respectively **(Figure 21B)**. Increasing the encapsulated fluorophore contents led to a decrease of the DiO (acceptor) emission, which was accompanied with an increase of the Dil (donor) fluorescence **(Figure 21B)**. These observations clearly demonstrated the occurrence of FRET from DiO to Dil fluorophores inside the nanoparticles. To confirm the occurrence of FRET, we measured the fluorescence lifetimes of DiO fluorophores in presence and absence of the acceptor (Dil). For this purpose, the particles with a low total fluorophore loading of 0.4% (w/w) was employed, to minimize the effect of self-quenching on the lifetime of fluorophore. Upon comparison, a significant reduction was observed in the excited state lifetime of the DiO fluorophores in presence of Dil **(Figure 21C and D)** and thus verified the presence of FRET. Assuming that the fluorophores were uniformed dispersed within the hydrophobic core of the particles, increasing the fluorophore contents (from 0.09 to 2.10% w/w) would decrease the distance between fluorophores (from 37 to 8 nm) and, thus, should favor FRET [288]. Our results demonstrated that D7 was among the brightest **(Table 12)** and significant fluorescence self-quenching was observed in the particles with fluorophore loading ≥ 3.0% w/w **(Figure 22)**. However, its size was >100 nm **(Table 11)** and, thus, unlikely to be applicable for *in vivo*

because of the potential uptake by the reticuloendothelial system (RES) [82]. Therefore, D6 was considered to have the optimum fluorophore loading (2.10% w/w).

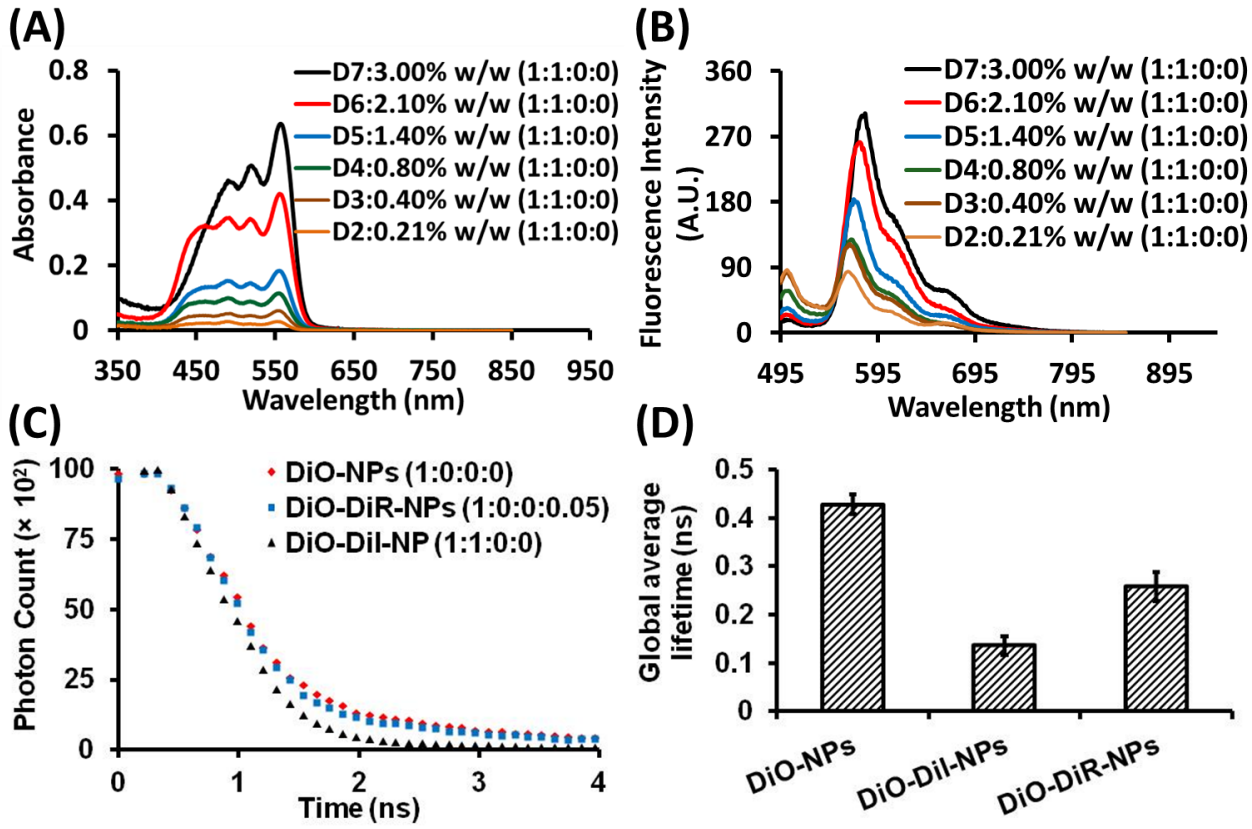

Figure 21. The (A) absorption and (B) fluorescence spectra of two-fluorophores doped nanoparticles. The particles were loaded with same ratio (1:1) of the DiO and DiI fluorophores with the different total fluorophore loading of 0.21 to 3.00 % (w/v). (C) Fluorescence decay curves of the DiO emission at 505 nm in absence and presence of the DiI and DiR fluorophores inside the nanoparticles. To minimize the effect of concentration dependent self-quenching on lifetime, the particles with lower total fluorophore loading (0.4% w/w) were synthesized instead of the optimized fluorophore loading (2.10% w/w). Three different nanoparticle formulations i.e. DiO-NPs (1:0:0:0), DiO-DiI-NPs (1:1:0:0), and DiO-DiR-NPs (1:0:0:0.05) were synthesized. (D) A bar chart showing a comparison of the global average lifetimes of different nanoparticles. The individual lifetime (ns) was obtained by fitting the fluorescence decay vs. time curve of nanoparticles in two-exponential model. All the samples consisted of the same number of nanoparticles (5×10^{11}/mL) suspended in deionized water (100 μL).

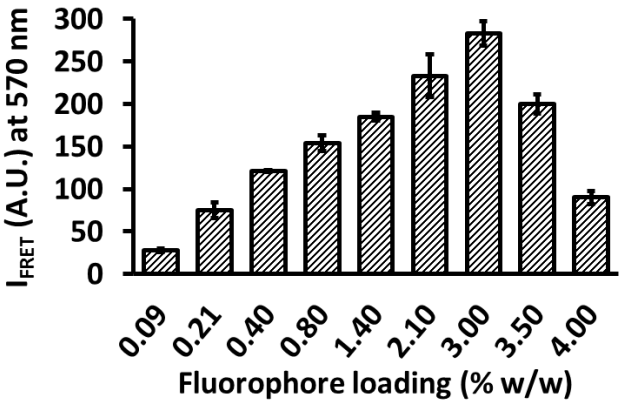

Figure 22. The optical properties of two-fluorophores doped nanoparticles. A plot of FRET intensity (I_{FRET}) versus fluorophore loadings. The particles were loaded with DiO and Dil fluorophores at the same ratio of 1:1. All the samples consisted of the same number of nanoparticles (5×10^{11}/mL) suspended in deionized water (100 μL).

3.4.3. Particles doped with three fluorophores

Next, we investigated if FRET cascade occurred in particles encapsulated with multiple fluorophores. T1-T5 containing the same total fluorophore content (2.10% w/w) but different ratios of DiO, Dil, and DiD were synthesized **(Table 13)**. These particles were characterized as above and have similar physical properties as D1-D7 **(Table 11)**. The successful encapsulations were confirmed by absorbance **(Figure 23A)**.

Table 13. The physical properties of three-fluorophores doped nanoparticles.

NPs	*Total Fluorophore Loading (% w/w)*	*DiO:Dil:DiD:DiR Ratio*	*Size (nm)*	*Polydispersity*	*Zeta Potential (mV)*
T1	2.10	1:1:0.05:0	88 ± 1.0	0.166 ± 0.03	-19 ± 1.4
T2	2.10	1:1:0.2:0	88 ± 3.2	0.163 ± 0.03	-19 ± 0.5
T3	2.10	1:1:0.5:0	86 ± 4.8	0.175 ± 0.04	-18 ± 1.5
T4	2.10	1:1:0.7:0	90 ± 5.1	0.192 ± 0.02	-17 ± 0.5
T5	2.10	1:1:1:0	82 ± 5.5	0.173 ± 0.07	-19 ± 0.6
R1	2.10	0:1:0.05:0	80 ± 1.5	0.170 ± 0.04	-19 ± 1.5
R2	2.10	1:0:0.05:0	81 ± 3.0	0.190 ± 0.02	-21 ± 0.5
R3	2.10	0:0:0.05:0	82 ± 4.0	0.170 ± 0.07	-20 ± 0.6

Table 14. The optical properties of three-fluorophores doped nanoparticles

NPs	*Absorbance λmax (nm)*				*FRET Emission λmax (nm)*			$I_{FRET(DiO \rightarrow Dil)}$ *(A.U.)*	$I_{FRET(DiO \rightarrow DiD)}$ *(A.U.)*	$I_{FRET(DiO \rightarrow DiR)}$ *(A.U.)*
	λmax_1	λmax_2	λmax_3	λmax_4	*DiO → Dil*	*DiO → DiD*	*DiO → DiR*			
T1	491	555	654	N/A	571	672	N/A	117 ± 6	329 ± 14	N/A
T2	491	555	652	N/A	570	672	N/A	76 ± 4	277 ± 23	N/A
T3	491	555	652	N/A	569	672	N/A	36 ± 1	143 ± 4	N/A
T4	491	555	652	N/A	568	673	N/A	26 ± 2	112 ± 5	N/A
T5	490	555	652	N/A	568	673	N/A	15 ± 3	81 ± 5	N/A
R1	N/A	556	651	N/A	575	667	N/A	37 ± 2	180 ± 15	N/A
R2	463	N/A	651	N/A	N/A	669	N/A	N/A	210 ± 20	N/A
R3	N/A	N/A	651	N/A	N/A	671	N/A	N/A	8 ± 1	N/A

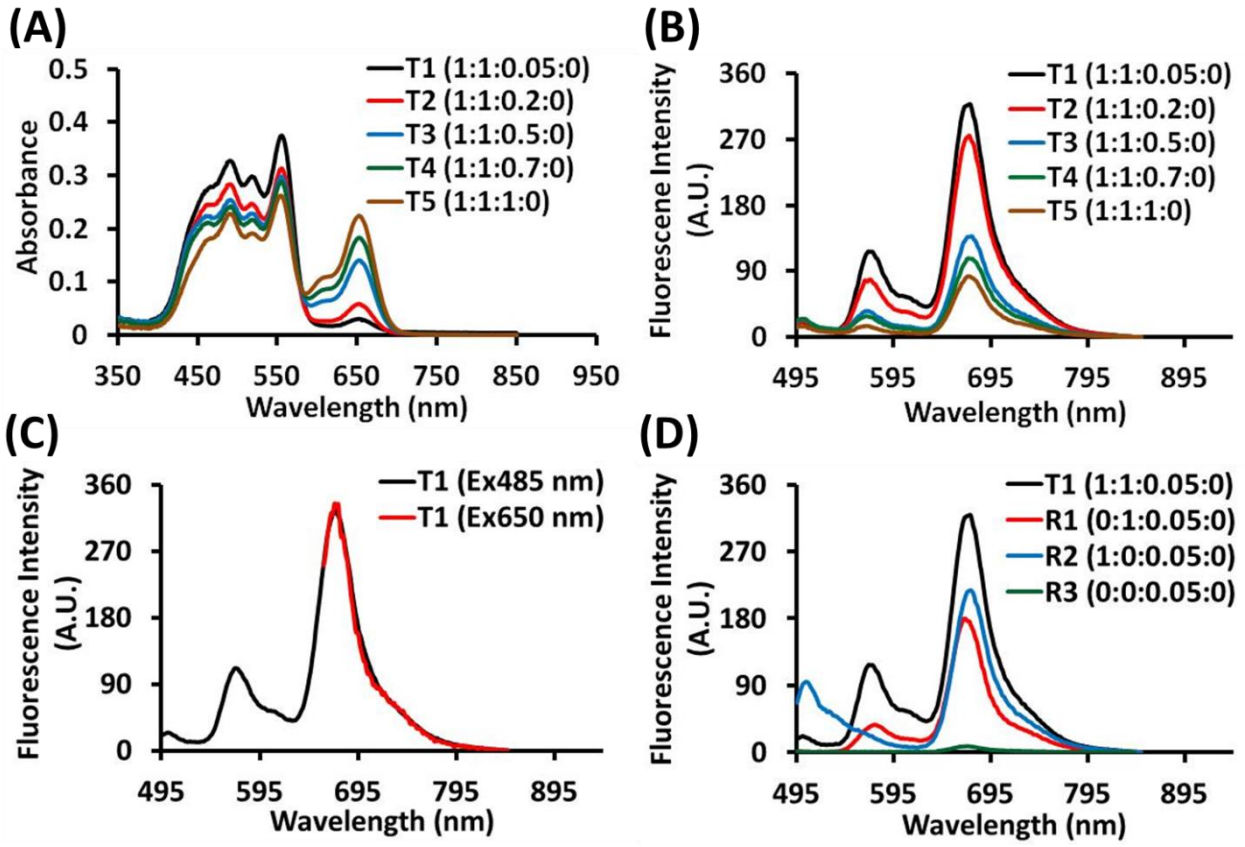

Figure 23. The (A) absorption and (B) fluorescence spectra of three-fluorophores doped nanoparticles. The particles were loaded with different ratios of DiO:Dil:DiD fluorophores at the same total fluorophore loading of 2.10% (w/w). (C) A fluorescence spectra of T3 after excitation at 485 and 650 nm. (D) The fluorescence spectra of control particles (R1-R3) lacking one or more intermediate fluorophores of T1.

Because of FRET cascade, upon excitation at 485 nm, all the particles displayed three distinct emission peaks at ~502, 569, and 672 nm **(Figure 23B)**. When compared to other particle platforms with a similar design [204, 205, 289], the emission λmax of our particles were more red-shifted. Among all the particles, T1 was the brightest, despite that it was encapsulated with the lowest amount of DiD **(Figure 23B and Table 14)**. In contrast, T5 containing the highest DiD content revealed the lowest fluorescence signals. Our results suggested that DiD was more prompt to fluorescence quenching than DiO and Dil. Interestingly, T1 showed a complete

energy transfer. The particles emitted the same fluorescence upon excitation at 485 and 650 nm **(Figure 23C)**. Such phenomenon was attributed to a combination of FRET cascade event and direct FRET from DiO to DiD, as shown by the control particles (R2) only encapsulated with DiO and DiD also emitted fluorescence at 669 nm, upon excitation at 485 nm **(Figure 23D).**

3.4.4. Particles doped with four fluorophores

To investigate whether we could extend the FRET cascade event to the NIR region, we synthesized Q1-Q5. These particles were encapsulated with the same total amount of fluorophore but different ratios of DiO, Dil, DiD, and DiR **(Figure 24A & Table 15)**.

Table 15. The physical properties of four-fluorophores doped nanoparticles.

NPs	*Total Fluorophore Loading (% w/w)*	*DiO:Dil:DiD:DiR Ratio*	*Size (nm)*	*Polydispersity*	*Zeta Potential (mV)*
Q1	2.10	1:1:1:0.05	88 ± 6.0	0.183 ± 0.02	-19 ± 1.4
Q2	2.10	1:1:1:0.2	92 ± 1.5	0.193 ± 0.01	-20 ± 0.5
Q3	2.10	1:1:1:0.5	90 ± 5.0	0.167 ± 0.03	-18 ± 1.0
Q4	2.10	1:1:1:0.7	89 ± 6.1	0.161 ± 0.03	-17 ± 0.5
Q5	2.10	1:1:1:1	90 ± 2.0	0.187 ± 0.06	-19 ± 0.6
Q6	2.10	1:1:0.2:0.05	89 ± 3.2	0.160 ± 0.02	-20 ± 0.6
Q7	2.10	1:1:0.2:0.2	89 ± 4.0	0.187 ± 0.03	-21 ± 0.2
Q8	2.10	1:1:0.2:0.5	87 ± 4.5	0.181 ± 0.02	-20 ± 2.0
Q9	2.10	1:1:0.2:0.7	88 ± 2.9	0.187 ± 0.03	-19 ± 0.5
Q10	2.10	1:1:0.2:1	82 ± 5.5	0.179 ± 0.03	-18 ± 0.6
Q11	2.10	1:1:0.2:0.8	81 ± 7.5	0.172 ± 0.07	-21 ± 1.0
Q12	2.10	1:1:0.14:0.54	84 ± 1.0	0.166 ± 0.04	-20 ± 0.4
Q13	2.10	1:1:0.1:0.4	86 ± 0.4	0.169 ± 0.02	-18 ± 1.5
Q14	2.10	1:1:0.067:0.27	81 ± 1.0	0.150 ± 0.07	-20 ± 2.0

Although all the particles fluoresced at 780 nm, they were all significantly quenched **(Figure 24B & Table 16),** as shown by the fact that the signal intensities were low and decreased with increasing DiD and DiR contents **(Figure 24C)**. To overcome this problem, we redesigned Q6-Q10 by reducing the ratio of DiD and DiR. The FRET in Q6 and Q7 were significantly higher as compared to Q1-Q5 **(Figure 26D)**. However, when both the encapsulated

DiD and DiR contents were too low, only a small fraction of the energy was able to transfer from the donor to the acceptor fluorophores **(Figure 24F)**. Because DiD and DiR were prompt to enact fluorescence quenching, we were unable to fine-tune a particle formulation that would only emit DiR fluorescence **(Figure 26E and F)**. Nevertheless, the multiple emission pattern of Q7 upon a single excitation should be applicable for multicolor imaging [290].

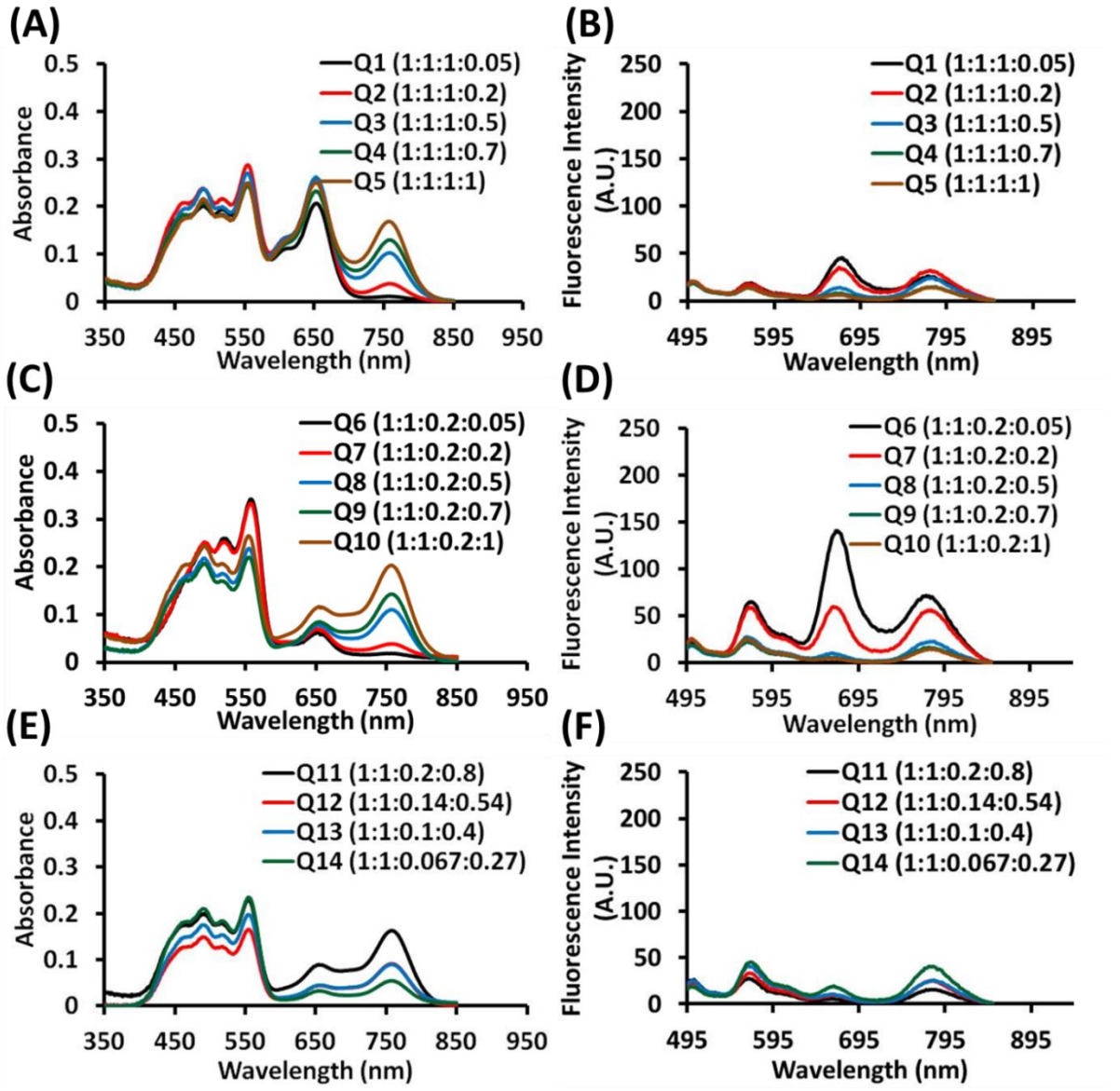

Figure 24. The (A,C,E) absorption and (B,D,F) fluorescence spectra of four-fluorophores doped nanoparticles.

Table 16. The optical properties of four-fluorophores doped nanoparticles.

NPs	*Absorbance λmax (nm)*				*FRET Emission λmax (nm)*			$I_{FRET(DiO \rightarrow Dil)}$ *(A.U.)*	$I_{FRET(DiO \rightarrow DiD)}$ *(A.U.)*	$I_{FRET(DiO \rightarrow DiR)}$ *(A.U.)*
	λmax_1	λmax_2	λmax_3	λmax_4	*DiO→Dil*	*DiO→DiD*	*DiO→DiR*			
Q1	490	554	653	760	570	674	770	22 ± 4	60 ± 5	40 ± 2
Q2	490	554	652	760	568	673	777	18 ± 1	34 ± 2	40 ± 4
Q3	490	554	652	758	565	673	780	14 ± 2	13 ± 1	25 ± 1
Q4	490	554	652	758	564	672	781	14 ± 2	9 ± 3	23 ± 4
Q5	491	554	652	757	564	672	782	14 ± 3	6 ± 1	13 ± 1
Q6	492	556	654	757	572	670	773	59 ± 6	142 ± 8	70 ± 6
Q7	492	556	654	757	570	669	779	56 ± 5	65 ± 6	53 ± 4
Q8	492	556	654	757	568	666	779	31 ± 3	12 ± 1	23 ± 1
Q9	492	556	654	757	565	660	779	27 ± 3	6 ± 1	15 ± 3
Q10	492	556	654	757	562	658	780	28 ± 2	5 ± 1	12 ± 4
Q11	490	554	655	758	566	665	781	25 ± 4	6 ± 2	18 ± 1
Q12	491	554	655	758	566	661	782	30 ± 4	9 ± 1	24 ± 2
Q13	491	554	655	758	566	660	782	38 ± 4	10 ± 1	24 ± 2
Q14	490	554	655	758	569	660	782	61 ± 6	32 ± 3	39 ± 2

To demonstrate the applicability of Q7 for multicolor imaging, we attached multiple copies of protein transduction domains (RRRRRRRC) to the particle surfaces. The successful conjugation of peptides to the nanoparticles was confirmed by absorbance (λmax=205 nm). Gel electrophoresis was also employed to ascertain the covalent conjugation of the peptides (Data not shown). The resulting R7-Q7 was characterized for the number of peptides attached to the surface by 9,10-phenanthrenequinone reagent [280] and showed increased size and zeta potential **(Table 17 & 18)**. Subsequently, the particles were applied to image SK-BR-3 breast cancer cells. The images were acquired at three different channels (Dil, DiD, and DiR) upon a single excitation and were found completely overlapping with each other **(Figure 25)**.

Table 17. The optical properties of particles chosen as a multiplexed and a multicolor platform.

Platform	*NPs*	*DiO:Dil:DiD:DiR Ratio*	*Color*	*λmax (nm)*	*I_{FRET}* (A.U.)*	*Stokes Shift** (nm)*
Multiplexed	D6	1:1:0:0	Red	570	233 ± 25	85
	T3	1:1:0.5:0	Far red	672	143 ± 4	187
	M5	1:0:0:0.05	NIR	777	120 ± 10	292
Multicolor	Q7	1:1:0.2:0.2	Red	570	56 ± 5	85
			Far red	669	65 ± 6	184
			NIR	779	53 ± 4	294

Abbreviations: Nanoparticles (NPs), near-infrared (NIR), FRET intensity (I_{FRET}), and arbitrary unit (A.U.) *I_{FRET} was the fluorescence intensity of the acceptor (at λmax) upon excitation of the DiO (at λmax) and **The Stokes shift was calculated according to the distance between the absorption and emission λmax.

Table 18. The physical properties of the particles conjugated with targeting ligands.

NPs	*Ligand*	*Size (nm)*	*Polydispersity*	*Zeta Potential (mV)*	*No. of Ligands/NP*
HER-D6	Herceptin	98 ± 5.5	0.165 ± 0.04	-18 ± 1.0	30
RAGE-T3	IgG2A11	94 ± 5.0	0.176 ± 0.03	-15 ± 1.5	35
R7-M5	RRRRRRRC	89 ± 3.0	0.180 ± 0.03	+10 ± 1.5	55
R7-Q7	RRRRRRRC	88 ± 2.5	0.185 ± 0.04	+11 ± 1.0	60

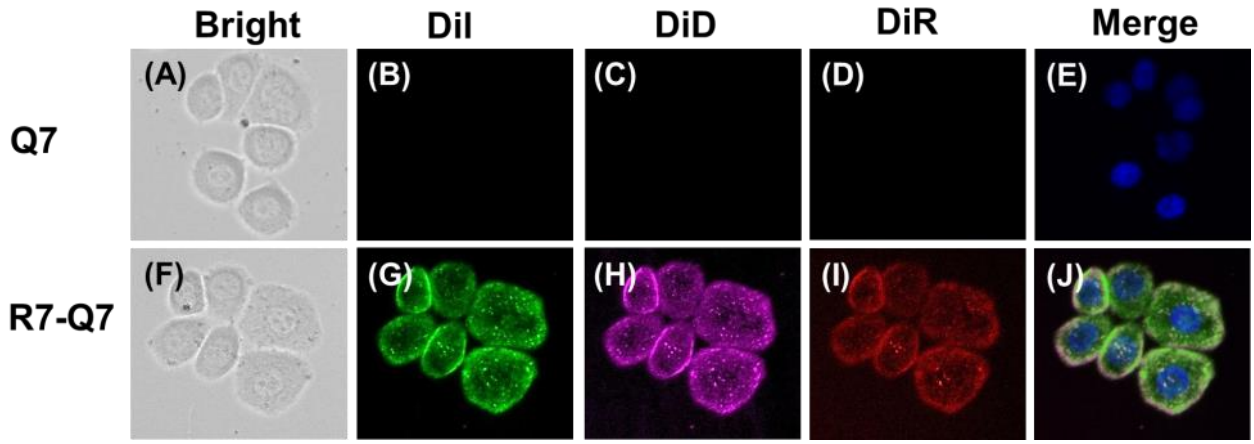

Figure 25. Multicolor imaging. R7-Q7 (9×10^{11}/mL, 400 µL) was chosen for imaging the SK-BR-3 cell line. The nuclei were counterstained with Hoechst 33342 (blue). (A) The bright light and (B-D) FRET images acquired at the Dil, DiD, and DiR channels. All the images (B-D) were merged into (E). (F) A merged image of the cells treated with control Q7 (9×10^{11}/mL, 400 µL). The FRET images were simultaneously acquired with the same excitation at 485 nm (original magnification, 20X).

Table 19. The optical properties of FRET pairs.

Donor : Acceptor	***Overlap (%)****	***Absorbance λmax of Donor (nm)*** **	***Emission λmax of Acceptor (nm)*** **	***Stokes Shift (nm)***
DiO : Dil	61	485	564	79
Dil : DiD	40	550	665	115
DiD : DiR	36	644	773	129
DiO : DiR	7	485	773	288

*The percentage overlap was estimated using Invitrogen fluorescence spectra viewer and **The calculation was based on the absorption and emission spectra of free fluorophore in methanol.

To confirm that the energy was transferred from DiO to DiR in Q7, we interrupted the FRET cascade event by dissolving the particles in DMF. After dissolution, the original emission peaks disappeared and, in exchange, we observed the recovery of DiO fluorescence **(Figure 26A)**. We also synthesized M1-M4 to serve as controls by removing the intermediate fluorophores (DiD and DiR) of Q7 **(Table 20 and 21)**. Yet M4 emitted fluorescence at 779 nm in the absence of Dil and DiD **(Figure 26B)**. This phenomenon was attributed to a direct FRET from DiO to DiR, since the particles did not show the same fluorescence upon excitation at 555

or 650 nm **(Figure 26C)** or after dissolved in DMF **(Figure 26D).** The fluorescence lifetime studies further confirmed the occurrence of a direct FRET from DiO to DiR, even at a lower total fluorophore loading of 0.4% w/w **(Figure 21).**

Table 20. The physical properties of two-fluorophores doped nanoparticles

NPs	*Total Fluorophore Loading (% w/w)*	*DiO:Dil:DiD:DiR Ratio*	*Size (nm)*	*Polydispersity*	*Zeta Potential (mV)*
M1	2.10	0:1:0.2:0.2	83 ± 1.0	0.165 ± 0.04	-20 ± 1.4
M2	2.10	1:0:0.2:0.2	84 ± 2.9	0.176 ± 0.03	-21 ± 0.5
M3	2.10	1:1:0:0.2	82 ± 2.9	0.160 ± 0.03	-22 ± 1.0
M4	2.10	1:0:0:0.2	86 ± 1.5	0.170 ± 0.01	-21 ± 0.5
M5	2.10	1:0:0:0.05	89 ± 4.0	0.186 ± 0.01	-22 ± 1.5
M6	2.10	1:0:0:0.1	89 ± 5.5	0.185 ± 0.02	-20 ± 0.3
M7	2.10	1:0:0:0.5	90 ± 3.1	0.172 ± 0.02	-19 ± 1.7
M8	2.10	1:0:0:0.7	90 ± 1.0	0.169 ± 0.02	-20 ± 0.2

Furthermore, the control particles containing DiR alone (DiR-NPs) did not fluoresce upon excitation at 485 nm **(Figure 26E)**. In fact, the calculated FRET efficiency (0.55) of M4 was high, despite the mere 7% overlap of the absorption and emission spectra of DiO and DiR, respectively **(Table 19).** This could be explained by the relatively higher DiO content; a small fraction of the DiO (donor) emission was sufficient to excite the majority of DiR (acceptor). To confirm this hypothesis, we prepared two particles that, individually, were only encapsulated with the same amount of DiO or DiR as M4. As expected, there was a large overlap (>65%) of the emission of DiO-containing particles and the absorption of DiR-containing particles **(Figure 26F)**. However, we did not rule out the possibility that energy could be transferred *via* the migration of electrons along the polymeric constructs of our particles [277].

Table 21. The optical properties of two-fluorophores doped nanoparticles

NPs	*Absorbance λmax (nm)*				*FRET Emission λmax (nm)*			$I_{FRET(DiO \rightarrow DiI)}$ *(A.U.)*	$I_{FRET(DiO \rightarrow DiD)}$ *(A.U.)*	$I_{FRET(DiO \rightarrow DiR)}$ *(A.U.)*
	λmax_1	λmax_2	λmax_3	λmax_4	*DiO→DiI*	*DiO→DiD*	*DiO→DiR*			
M1	N/A	555	651	757	565	666	779	10 ± 1	5 ± 1	10 ± 1
M2	459	N/A	653	757	N/A	668	779	N/A	8 ± 1	23 ± 2
M3	492	555	N/A	756	569	N/A	779	68 ± 5	N/A	57 ± 3
M4	461	N/A	N/A	757	N/A	N/A	779	N/A	N/A	40 ± 2
M5	492	N/A	N/A	756	N/A	N/A	777	N/A	N/A	120 ± 10
M6	492	N/A	N/A	756	N/A	N/A	779	N/A	N/A	108 ± 13
M7	492	N/A	N/A	756	N/A	N/A	779	N/A	N/A	14 ± 2
M8	493	N/A	N/A	757	N/A	N/A	779	N/A	N/A	11 ± 1

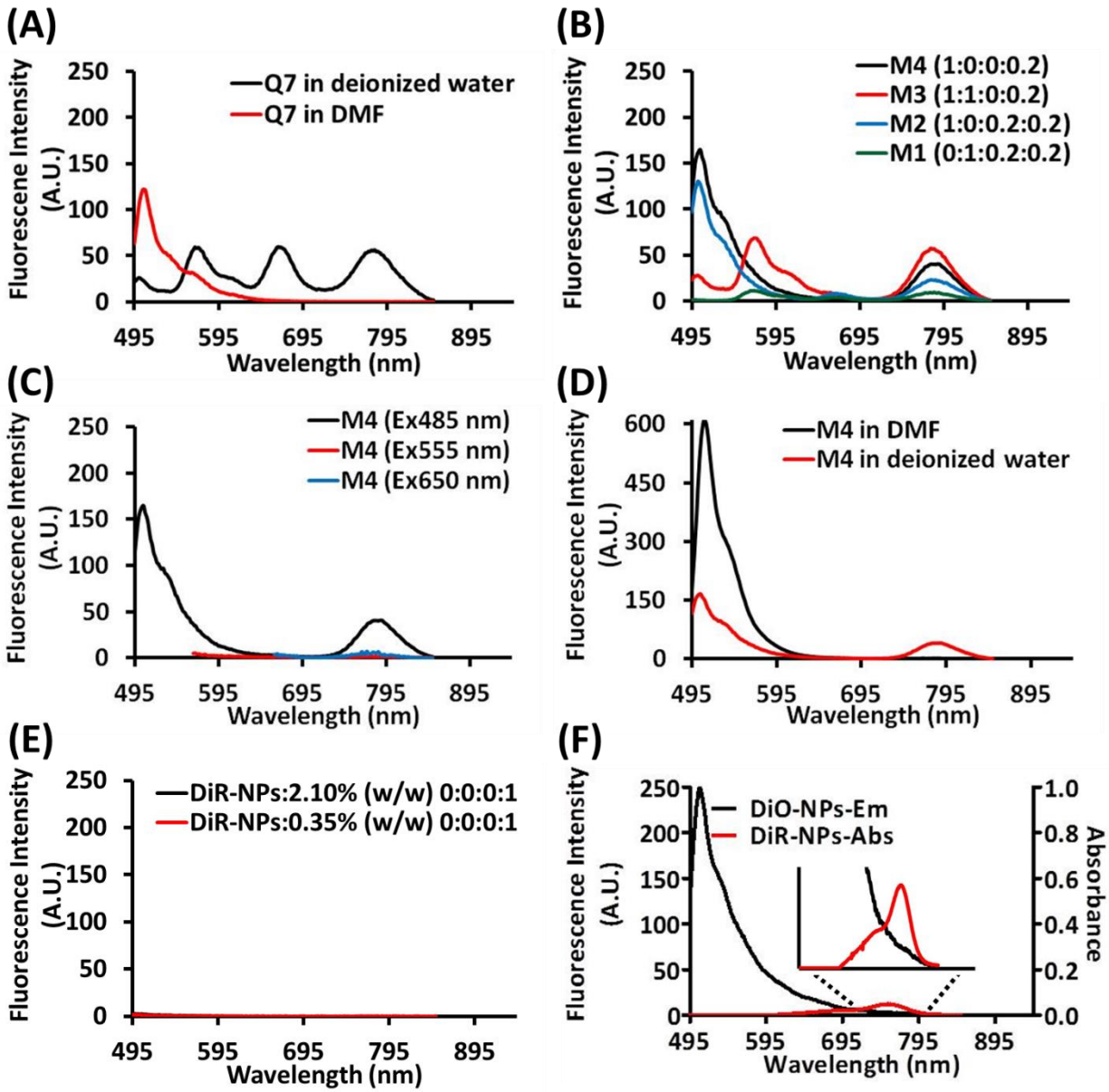

Figure 26. The optical properties of fluorophore-doped nanoparticles. (A) Fluorescence spectra of Q7 in deionized water and DMF. The number of particles in DMF was 10X lower than in water. (B) Fluorescence spectra of M1-M4 in deionized water. (C) Fluorescence spectra of M4 after excitation at different wavelengths. (D) A comparison of M4 in DMF and deionized water. The number of particles dissolved in DMF was 10X lower. (E) the fluorescence spectra of particles that encapsulated with DiR alone in deionized water. (F) The emission spectrum (black) of particles encapsulated with DiO alone (1.75% w/w) and the absorption spectrum (red) of particles encapsulated with DiR alone (0.35% w/w).

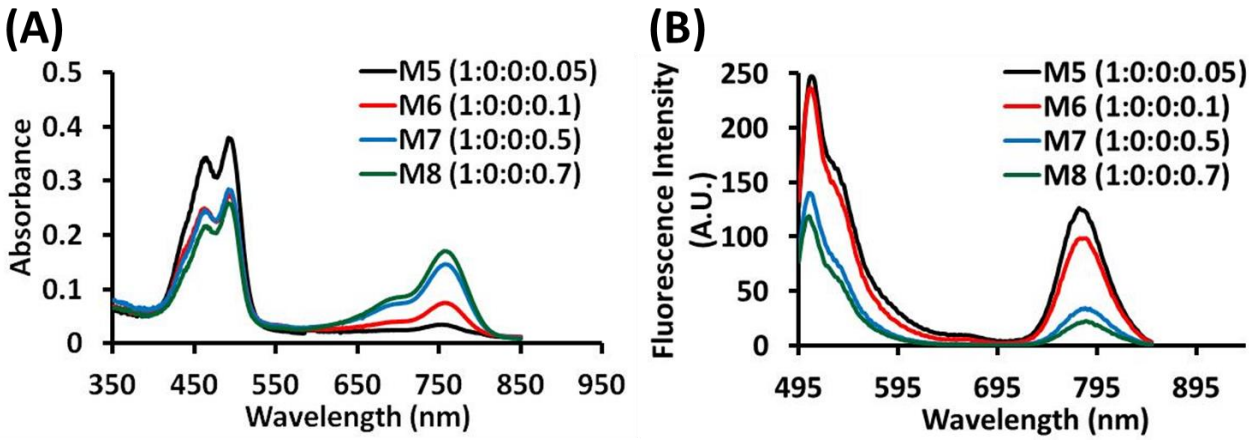

Figure 27. The (A) absorption and (B) fluorescence spectra of two-fluorophores doped nanoparticles. The particles were loaded with different ratios of the DiO and DiR fluorophores at same total fluorophore loading of 2.10% (w/w).

Considering that the distance between the excitation and emission λmax of M4 was more than 250 nm, the particles could still become a useful imaging platform. Hence, to improve the brightness of M4, we synthesized M5-M8 by lowering the ratio of DiR versus DiO **(Figure 27A and Table 20)**. As expected, the amount of DiR was crucial for controlling the brightness of M5-M8 **(Table 21)**. However, more quenching was found when we attempted to enhance the FRET by increasing the encapsulated DiR content. This observation was similar to the four-fluorophores doped nanoparticles **(Figure 24B)**, where we found that the DiR fluorophores were more prone to fluorescence quenching with the increasing concentration. As a result, M5 consisting of the lowest DiR content displayed the highest FRET at 777 nm, but due to an insufficient amount of DiR inside the particles to accept all the energy from the donor (DiO) emissions, the particles also exhibited a significant DiO fluorescence at 505 nm **(Figure 27B)**.

3.4.5. A multiplexed imaging platform

Next, we combined a mixture of particles into a multiplexed imaging platform. D6, T3, and M5 were selected because each of them displayed a distinct fluorescence emission at 570, 672, and 777 nm, respectively, upon excitation at 485 nm **(Table 17)**. These particles were brighter (>10 times) than water-soluble QDs **(Figure 28)**, and their emission peaks were well resolved from one another, with a separation distance of >100 nm.

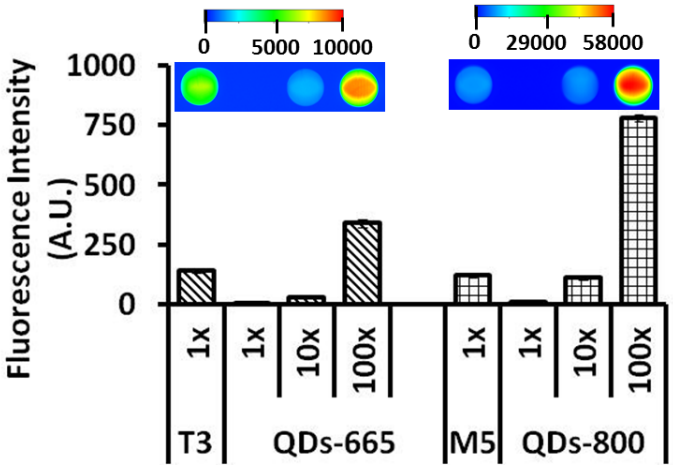

Figure 28. Brightness of nanoparticles. A comparison of the brightness of T3 (emission λmax at 672 nm) and M5 (emission λmax at 777 nm) with the corresponding water-soluble QDs. Note: 1X refers to 5×10^{11} particles/mL. Inset: The FRET images of the particles in a 96-wells plate.

To introduce binding specificity to the particles, we also attached multiple antibodies against HER2 (Herceptin) and RAGE (IgG2A11) to the surfaces of D6 and T3, respectively [279] **(Figure 29)**. Protein transduction domains were conjugated to M5 as the non-specific particles for cell labeling [291, 292]. The resulting particles, HER-D6, RAGE-T3, and R7-M5, were characterized for the number of antibodies and peptides attaching to the surface by BCA protein assay and 9,10-phenanthrenequinone reagent, respectively **(Table 18)** [280]. There were

no significant changes in the morphology and the optical property of the surface-modified nanoparticles, as compared to the unmodified ones.

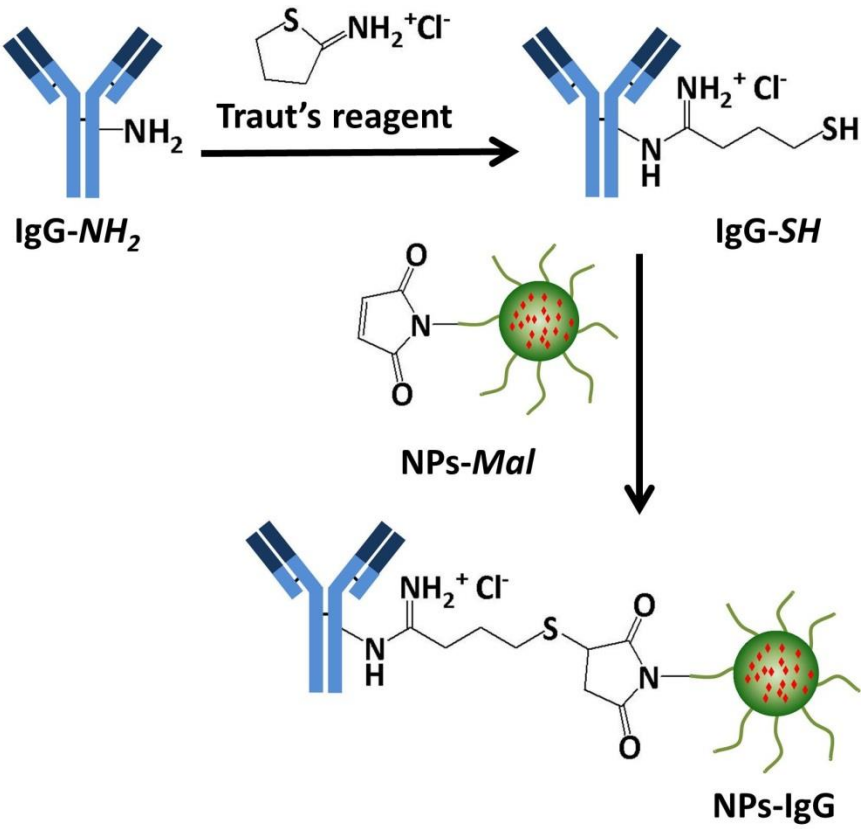

Figure 29. Synthetic scheme for conjugation of nanoparticles to the antibody using Traut's reagent as a linker. The Traut's reagent was reacted with the amino groups of the antibodies to generate free sulfhydryls. The modified antibodies (IgG-*SH*) could be anchored to the surface of maleimide-terminated PLGA-PEG nanoparticles (NPs-*Mal*) *via* thioether bonds.

Next, we employed SK-BR-3 and WM-115-RAGE as the cell models to evaluate the specificity of the particles. SK-BR-3 is a breast cancer cell line that naturally overexpresses HER2 [293]. WM-115-RAGE is derived from the WM-115 melanoma cell line that was stably transfected with the cDNA of full-length RAGE and was a generous gift from Dr. Leclerc [292, 294]. The two cell lines could be easily distinguished from one another based on their

morphologies and, thus, were selected for proof-of-principle experiments. Prior to performing cellular imaging, all the particles were confirmed to be non-toxic by MTS assay **(Figure 30)**.

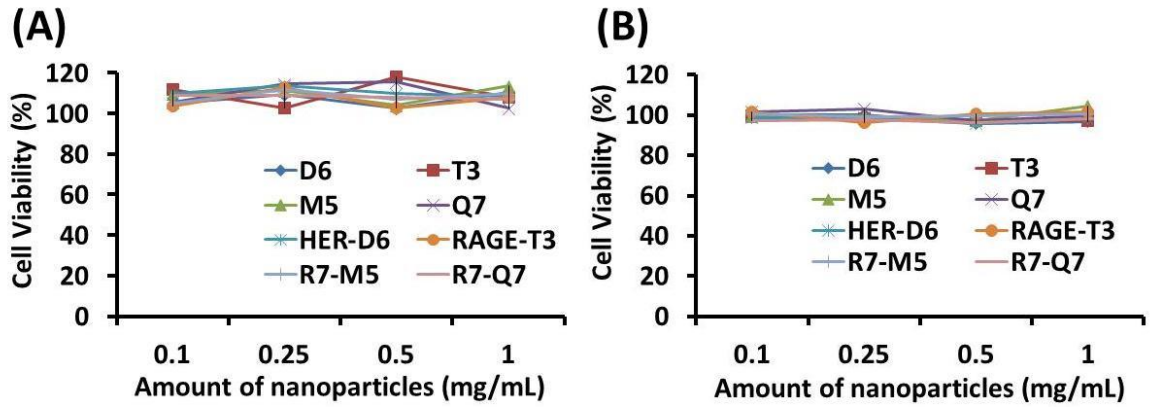

Figure 30. Cytotoxicity assay. The particles were incubated in (A) SK-BR-3 and (B) WM-115-RAGE cell lines for 24 h. The percentage of cell viability was determined by MTS assay.

We observed that both HER-D6 and RAGE-T3 bound specifically to the SK-BR-3 and WM115-RAGE cell lines, respectively **(Figure 31A and B)**. The discrete fluorescence signals localized at the cell membranes and appeared within the cytoplasm, indicating that these particles were taken up by the cancer cells *via* receptor-mediated endocytosis [295]. On the other hand, the control particles i.e., the unconjugated D6 and T3 did not show any non-specific binding **(Figure 32)**. Similar to other polyarginine-conjugated nanoparticles [296], R7-M5 was most likely internalized into both SK-BR-3 and WM115-RAGE *via* the non-endocytic pathways [297] and, thus, was found distributed throughout the cytoplasm, with some of the particles translocated to the nucleus and perinuclear regions **(Figure 31C and D)** [298, 299]. A collection of multiple particles with diverse emission signatures can be a useful tool for detecting different cancer cell targets simultaneously [300-302]. Here, using a combination of HER-D6, RAGE-T3, and R7-M5 (1:1:1), we were also able to identify SK-BR-3 and WM-115-RAGE in a mixture of cell lines according to the expression of cell-surface receptors **(Figure 31E)**.

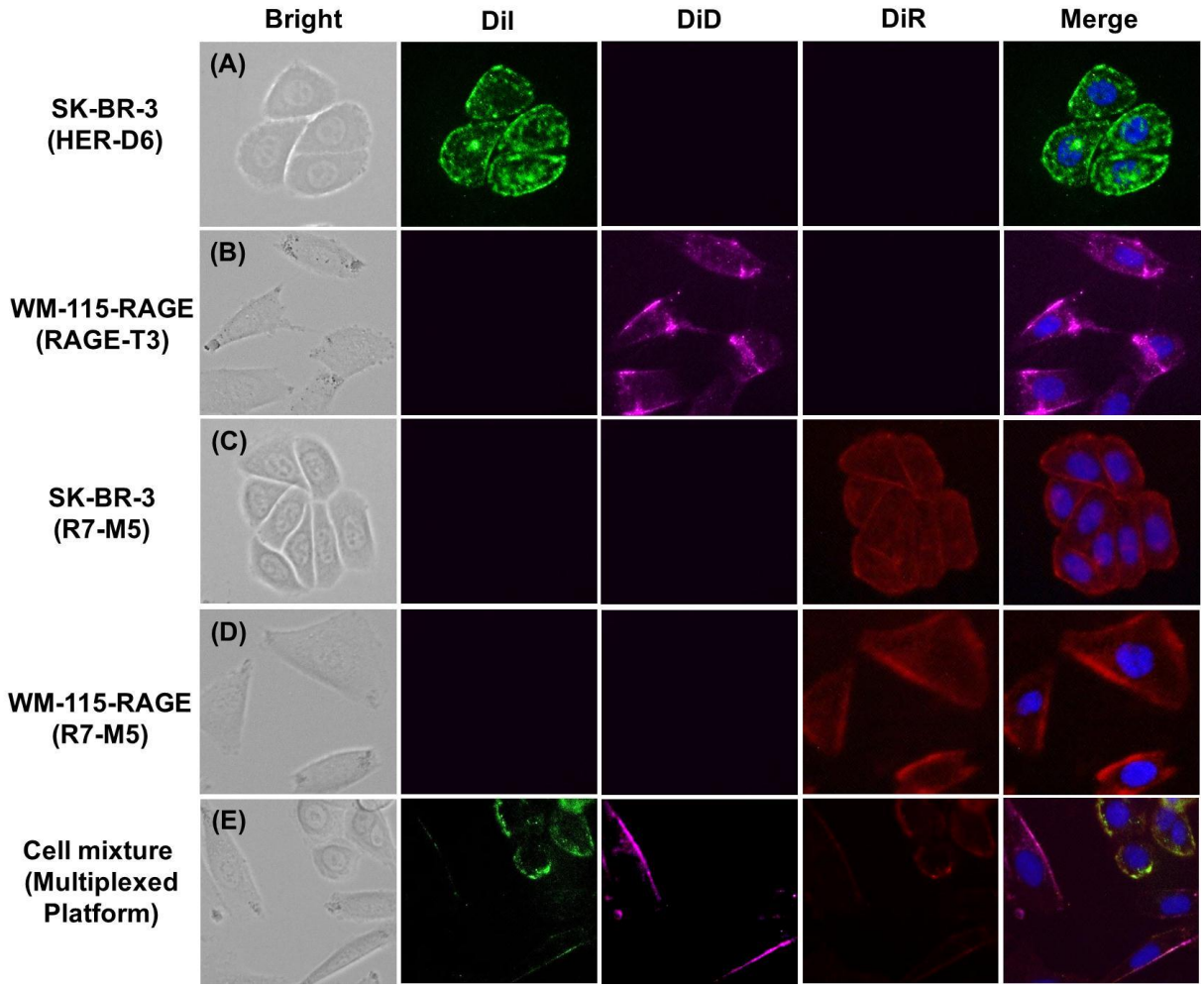

Figure 31. Multiplexed imaging. All the cells were exposed to the same number of particles (9×10^{11}/mL, 400 µL) for 15 min at 37°C. Hoechst 33342 (blue) was employed as the nuclear staining. FRET images of (A, C) SK-BR-3 and (B, D) WM-115-RAGE after the exposure of HER-D6 (green), RAGE-T3 (magenta), or R7-M5 (red). (E) The multiplexed platform i.e., a mixture of the particles could image SK-BR-3 and WM-115-RAGE simultaneously. All the FRET images were acquired with the same excitation wavelength at 485 nm and were adjusted to the same window settings at the corresponding channels (original magnification, 20X).

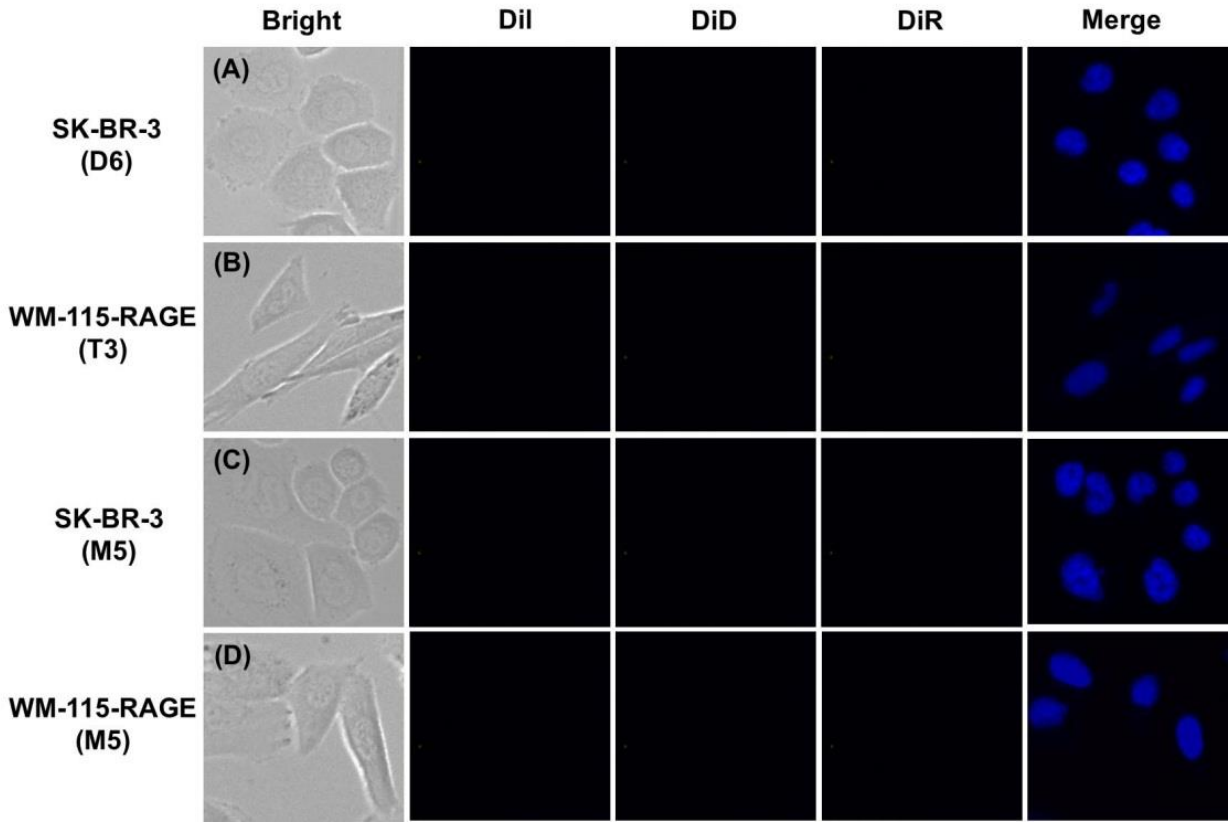

Figure 32. Control studies on the specificity of ligand-conjugated particles employed for the multiplexed imaging platform. All the cells were exposed to the same number of particles (9×10^{11}/mL, 400 μL) for 15 min at 37°C. Hoechst 33342 (blue) was employed as the nuclear stain. FRET images of (A, C) SK-BR-3 and (B, D) WM-115-RAGE after the exposures of the unconjugated D6, T3, and M5. All the FRET images were acquired with the same excitation wavelength at 485 nm and were adjusted to the same window settings at the corresponding channels as Figure 5 (original magnification, 20X).

3.4.6. *In vivo* multiplexed imaging

Next, we explored the potential of our platform for *in vivo* multiplex imaging in live animal. The imaging capability of RAGE-T3 and R7-M5 were compared with their corresponding water-soluble QDs, QDs-665 and QDs-800, respectively. For ease of comparison, the same numbers of particles were subcutaneously injected into different regions (near the abdomen) of a severe combined immunodeficiency (SCID) mouse to perform a whole-body FRET imaging [278]. The fluorescence emissions of RAGE-T3 and R7-M5 were higher than the

QDs, since our particles were 10 times brighter **(Figure 33A and B)**. The results were in good agreement with our *in vitro* data **(Figure 28)**. Here, HER-D6, RAGE-T3, and R7-M5 could be used together as a multiplexed platform for *in vivo* imaging **(Figure 33C)**. However, the calculated signal-to-noise ratios (SNR) among the particles were significantly different and increased with the following order: HER-D6<RAGE-T3<R7-M5 **(Figure 33D)**. This result could be explained by a lower autofluorescence generated from the mouse tissue at the NIR region [14].

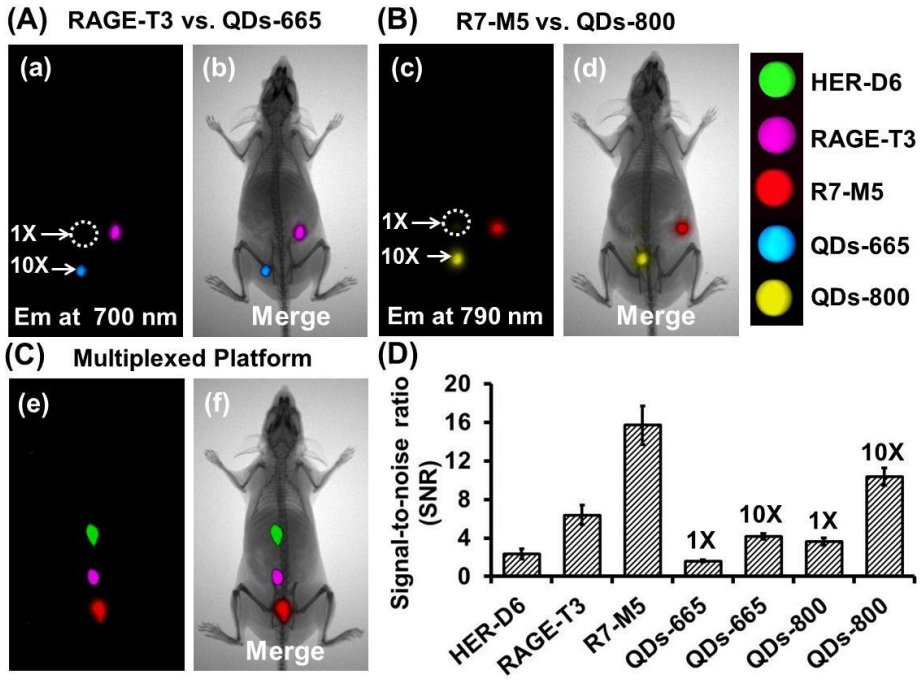

Figure 33. *In vivo* multiplexed imaging. A comparison of (A) RAGE-T3 and (B) R7-M5 with the corresponding QDs-665 and QDs-800, respectively. (C) A merged FRET image and a merge FRET and X-ray image of a SCID mouse that was subcutaneously injected with HER-D6 (green), RAGE-T3 (magenta), and R7-M5 (red) particles (3.5×10^{11}) in deionized water (10 µL) at different regions. Inset: The pseudo-color assigned for each particle. (D) A bar chart was plotted to compare the signal-to-noise ratio (SNR) of different nanoparticles and QDs, where 1X and 10X are referred to 3.5×10^{11} and 3.5×10^{12} particles, respectively.

3.5. Conclusion

In the present study, we report a series of FRET-based polymeric nanoparticles for multicolor and multiplexed imaging applications [213, 275, 303, 304]. For the first time, four complimentary carbocyanine-based fluorophores, DiO, Dil, DiD, and DiR were encapsulated inside a single particle to engender a broad range of code ranging from the visible and NIR wavelength region. Because of the hydrophobic nature of both fluorophores and the particle core, the fluorophore molecules were confined in close proximity to enable sequential resonance energy transfer [278]. Thus, by doping the different combinations, numbers, and concentrations of the fluorophores, the optical properties of the particles could be fine-tuned for multicolor imaging [305] and multiplexing imaging [214, 269]. The particles were nontoxic, 10 times brighter than QDs, and exhibited extremely low background signals, as compared to previously reported nanoparticles [204, 205]. Here, we identified an optimized particle formulation (Q7) that emitted fluorescence at multiple wavelengths upon a single excitation for multicolor imaging. We also combined three other particles (D6, T3, and M5) as a multiplexed imaging platform. By conjugating specific targeting ligands to the particle surfaces, we demonstrated that the developed platform was able to identify the target cancer cells by FRET imaging. Unlike other multiplexed systems [204, 205, 270], the emission maxima of particles composed in our platform were well resolved (≥100 nm). Therefore, minimal spectral deconvolution was required during imaging analysis [270, 306, 307]. Overall, we believe that our particle platform, when used in combination with multispectral imaging, could have far-reaching potential for identifying multiple cell types or tissue structures *in vivo* [308].

CHAPTER 4. A SHORT CIRCULATING PEPTIDE NANOFIBER AS A CARRIER FOR TUMORAL DELIVERY

** Published in Nanomedicine: Nanotechnology, Biology and Medicine, Volume 9, Issue 4, Pages 449-457, May 2013, doi:10.1016/j.nano.2012.10.009) (© 2013 Elsevier Inc.)*

4.1. Abstract

The cellular interactions and *in vivo* distribution of the nanomaterials are known to be strongly influenced by their physiochemical properties. Here, we investigated and compared the biocompatibility, pharmacokinetics, and biodistribution of previously reported peptide-based nanofiber (NFP), with commercially available nanomaterials. The NFP was a 2-dimensional (2D) structure with an extremely narrow width (4 nm) and a controllable length (50 to 400 nm). NFP was found to be non-toxic, hemocompatible, and with a minimum uptake by macrophages. *In vivo* studies further demonstrated that NFP could be delivered to the tumor site more effectively, and within a very shorter period of time, than spherical nanoparticles. Importantly, the undelivered NFP was rapidly eliminated by renal clearance and, thus, avoiding its accumulation in the spleen or liver. Overall, our data suggested a new paradigm in drug delivery *via* using a short circulating NFP, rather than a long circulating 3D nanoparticle, as a delivery cargo.

4.2. Background

Many nanomaterials have been proposed as drug carriers [309]. Particularly in cancer, because of the leaky vasculature and poor lymphatic drainage, nanomaterials tend to accumulate at the tumor site *via* enhanced permeability and retention (EPR) effect [310]. For this reason, drug delivery using nanomaterials can offer an advantage of reducing adverse effects of

chemotherapeutic agents. For example, paclitaxel, SN-38, doxorubicin, or cisplatin has been encapsulated into polymeric nanomaterials to reduce the administration dosage [160, 311-314]. In fact, several nanoparticle formulations such as liposomal doxorubicin (Doxil®) and albumin particles encapsulated with paclitaxel (Abraxane®) have been already approved by the food and drug administration (FDA) for the treatment of Kaposi's sarcoma, ovarian, and breast cancer [315, 316]. However, due to the prolonged circulating time in the body, Doxil is known to suffer from new side effects, including hand-foot syndrome and mucositis. Furthermore, the pharmacokinetic and *in vivo* distribution of a nanomaterial can be affected by many physicochemical properties [82].

Smaller nanoparticles (< 3-5 nm) are often eliminated from the body by renal clearance and thus have relatively shorter plasma half-lives [84]. On the other hand, larger particles (> 10-20 nm) are prompt to be captured by the reticuloendothelial system (RES) [85], and therefore, are more likely to be taken up by the liver and spleen [317]. Apart from size, the shape and charge of a nanomaterial can also play important roles in the pharmacokinetic property and biodistribution [318, 319]. For example, after intravenous injection, the uptake of gold nanorods by the liver was found to be lower than its spherical counterpart of same size [320]. In another study, the negatively charged liposomes were shown to have a significantly shorter plasma half-life than the neutral ones [319]. Given that no universal rule can be applied to predict the *in vivo* behavior of nanomaterials, the safety of the nanomaterials should be evaluated on a case by case basis. Besides, understanding the biocompatibility of a nanomaterial is essential to predict its future applications *in vivo*.

Peptide based nanomaterials have gained much interest because of their design flexibility and structural diversity that enabled their diverse applications [282, 321, 322]. Self-assembling peptides have been employed as a novel platform for the local delivery of hydrophilic peptides, proteins, and hydrophobic anticancer agents [323]. For example, EAK16-11 is a class of self-assembling peptide, which can stabilize hydrophobic molecules such as pyrene and ellipticine and serve as an efficient slow delivery carrier for releasing the molecules in a controlled manner [324]. Similarly, our laboratory has previously developed a new type of peptide-based nanofiber (NFP) for imaging and drug delivery [243, 282]. NFP was composed of multiple peptide constructs. Each peptide construct consisted of (a) a self-assembling peptide sequence (kldlkldlkldl) that has been used for tissue engineering [325] and (b) a hydrophilic polyethylene glycol (PEG) to prevent aggregation and possible uptake by the RES [326]. In an aqueous buffer, multiple peptides self-assembled together to form a nanofiber (NFP). Unlike the other nanofibers, NFP has a unique dimension (4 nm in width × 50-400 nm in length) and does not fuse to form the cylindrical nanotubes [327]. The presence of hydrophilic mPEG chain also prevents the formation of hydrogel network by inhibiting the possible interfibril interactions [328].

Despite of wide spread use, there are very limited studies available for exploring the biocompatibility and tissue distribution of peptide-based nanomaterials. In the present study, we investigated the biocompatibility of previously designed NFP to extend the application to *in vivo* system. We also compared the hemocompatibility and biodistribution of NFP with various commercially available nanomaterials that were different in terms of composition, size, charge, surface area, and shape (Table 1). *In vivo* studies demonstrated that the optimized NFP was more

effective as a tumoral delivery platform and, thus, has potentials as a delivery platform for cancer treatment.

4.3. Experimental procedures

4.3.1. Chemicals and materials

All solvents were purchased from Fischer Scientific (Pittsburg, PA). All amino acids were obtained from EMD4Bioscience (Gibbstown, NJ). The poly(D,L-lactic-*co*-glycolic acid) (PLGA-COOH, monomer ratio 50:50, 17 kDa) was received as a generous gift from PURAC Biomaterials (Netherland). *N*-hydroxysuccinimide activated methoxy polyethylene glycol (NHS-PEG_{2470}-OCH_3) was purchased from JenKem Technology USA, Inc. (Allen, TX). *N*,*N*-diisopropylethylamine (DIEA), fluorescein isothiocyanate (FITC), and gelatin veronal buffer were obtained from Sigma-Aldrich (St. Louis, MO). Uranyl formate and formvar/carbon coated grids (200 mesh) were obtained from Electron Microscopy Sciences (Hatfield, PA) and SPI Supplies/Structure Probe, Inc. (West Chester, PA), respectively. Trilite™ (QD-6) was purchased from Cytodiagnostics, Inc. (Burlington, Ontario). 1,1'-dioctadecyl-3,3,3',3'-tetramethylindodicarbocyanine, 4-chlorobenzenesulfonate salt (DiD), and Hoechst 33342 trihydrochloride trihydrate were purchased from Life Technologies Corporation (Grand Island, NY). Fluorophorex™ (PS-50 and PS-100) were obtained from Phosphorex, Inc. (Fall River, MA). Multi-walled carbon nanotubes (MWNT-2000) were purchased from US Research Nanomaterials, Inc. (Houston, TX). All gold nanoparticles (AU-60 and AU-80) were obtained from BioAssay Works (Ijamsville, MD). Cy5.5 monofunctional hydroxysuccinimide ester (Cy5.5-NHS) was purchased from GE Healthcare Biosciences (Piscataway, NJ). Whole blood was purchased from Biochemed Services (Winchester, VA). Human serum and antibody

sensitized sheep erythrocytes were purchased from Complement Technology, Inc. (Tyler, TX). Alexa Fluor® 488 rat anti-mouse CD31 antibody was purchased from BioLegend, Inc. (San Diego, CA). Cyanmethemoglobin reagent and hemoglobin standards were provided by Ricca Chemical (Arlington, TX) and Stanbio Laboratory (Boerne, TX), respectively.

4.3.2. Synthesis of the peptide construct

The peptide construct, $mPEG_{2470}$-BK(*FITC*)SGRSANA-kldlkldlkldl-$CONH_2$, was synthesized on an automated solid-phase peptide synthesizer (PS3™, Protein Technologies, Inc., Tucson, AZ, USA) by employing the standard Fmoc-protected amino acids on rink-amide resin as previously described [243]. After synthesis, the peptide was cleaved from the resin, precipitated, and washed in methyl *tert*-butyl ether. The crude peptide was purified by high-performance liquid chromatography (Agilent Technologies, Santa Clara, CA, USA) and characterized using MALDI-TOF mass spectrometry at Tufts Medical School (Boston, MA).

4.3.3. Synthesis of NFP-50, NFP-100, and NFP-400

The NFP was assembled in an aqueous environment as previously described [243]. Briefly, the solid peptide (1 mg) dissolved in DMSO (20 µL) was added to 50% (v/v) acetonitrile in PBS buffer (400 µL). The solution mixture was then stirred vigorously at room temperature overnight inside a fume hood to evaporate the solvent. Stock NFP (75 µM) suspended in PBS buffer (200 µL) was conjugated to Cy5.5-NHS (132 µM, 200 µL) according to the manufacturer's instruction. The resulting NFP was purified by size exclusion chromatography (Sephadex G-100, GE Healthcare Biosciences, Piscataway, NJ) and further homogenized into NFP-50, NFP-100, or NFP-400, by passing through a mini-extruder (Avanti Polar Lipids, Inc.,

Alabaster, AL, USA) using a polycarbonate membranes (GE Healthcare Biosciences, Piscataway, NJ, USA) of different pore sizes (50 nm, 100 nm, and 400 nm). The concentrations of NFP and Cy5.5 were determined by absorbance based on their molar extinction coefficients in 95% (v/v) methanol in PBS buffer, where $\varepsilon_{FITC\ at\ 485\ nm}$ = 65,000 $M^{-1}cm^{-1}$ and $\varepsilon_{Cy5.5\ at\ 675\ nm}$ = 250,000 $M^{-1}cm^{-1}$. It was calculated that the average number of Cy5.5 molecules per two peptides was one.

4.3.4. Synthesis of PLGA-100

The PLGA-PEG copolymer was synthesized by carbodiimide chemistry and the nanoparticles encapsulated with DID fluorophore (PLGA-100) were fabricated by the nanoprecipitation method as previously described [278]. Briefly, a mixture of PLGA-PEG copolymer (10 mg) and DiD fluorophore (0.1 mg) dissolved in DMF (1 mL) was added dropwise to deionized water (10 mL). The resulting particles were allowed to stir for 2 h at room temperature. The particles were then purified by ultrafiltration (3000 × *g*, 15 min) using SPIN-X UF concentrators with a 10 kDa MWCO (Corning Incorporated, Lowell, MA, USA) and washed with deionized water (2 × 5 mL). The purified nanoparticles were re-suspended in deionized water (2 mL).

4.3.5. Physical characterization of the nanomaterials

The size of the nanomaterials was determined by dynamic light scattering (Zetasizer, Malvern Instruments Ltd., Worcestershire, UK) at 25°C. The length of non-spherical nanomaterials including MWCT and NFP was determined by dynamic light scattering as previously described [329]. The intensity-weighted mean values were recorded as the average of

three independent measurements with the same particle concentration (0.1 mg/mL) in deionized water. The refractive index and viscosity of the solvent i.e. deionized water was set at 1.33 and 0.8872 cP, respectively. The zeta potentials of the nanomaterials were measured using a disposable capillary cell (Malvern Instruments, Worcestershire, UK) with the same particle concentration (0.1 mg/mL) in deionized water.

The size and morphology of NFP was confirmed by transmission electron microscope (JEOL 100CX, Jeol Ltd., Peabody, MA, USA) as previously described [328]. The NFP (5 µM) in deionized water (10 µL) was adsorbed onto formvar/carbon coated grids for 1 min and the excess samples were blotted off by filter paper. The grids were negatively stained with 0.75% (w/v) uranyl formate in deionized water (10 µL) for 1 min and then air-dried. The images were acquired using a computer controlled station.

4.3.6. MTS assay

The MTS assay was performed as previously described [282]. Both the mouse leukemic macrophage (RAW 264.7) and the human embryonic kidney (HEK-293) cell lines were obtained from American Type Culture Collection (Manassas, VA, USA). The cells were cultured in Dulbecco's Modified Eagle Medium (DMEM) supplemented with 10% (v/v) fetal bovine serum (FBS), penicillin (50,000 units/L), and streptomycin (50 mg/L) and maintained in 5% CO_2 at 37°C. The cells (5000/well) were seeded in a clear bottom 96-well plate (Corning Incorporated, Lowell, MA) for 12 h. The nanomaterials (0.4 and 4 mg/mL) in PBS buffer (50 µL) were mixed with complete DMEM medium (150 µL) and incubated with cells at 37°C. Cells incubated with PBS buffer served as a negative control. After 24 h of incubation, fresh media containing the MTS reagent (Promega Corporation, Madison, WI) was added to each well and cells were

further incubated for 1 h at 37°C. The absorbance of the reduced formazan products (A) was directly measured at 490 nm using a spectrophotometer (Spectramax, Molecular Devices, Inc., Sunnyvale, CA, USA). All the absorbance values were corrected for the blank (media only). The interference of the respective nanomaterials at 490 nm was corrected by measuring the absorbance of same amount of the nanomaterial in the complete culture media. After all corrections, the percentage cell viability was determined by using the following equation:

$(A_{sample})/(A_{control}) \times 100\%$ ..... (23)

4.3.7. Hemolysis assay

The hemolysis of the nanomaterials was tested according to new American Society for Testing and Materials (ASTM) standard E2525-08 as previously described [246]. Briefly, red blood cells (RBCs) were isolated from the blood by centrifugation (800 × *g*, 15 min), then washed and re-suspended in PBS buffer (3.5×10^8 cells/mL). The nanomaterials (0.2 and 1 mg/mL) in PBS buffer (100 µL) were added to the stock of erythrocyte dispersion (100 µL) and then incubated for 3 h at 37°C. Triton X-100 in deionized water (10% v/v) and PBS buffer were used as the positive and negative controls, respectively. The intact erythrocytes were then separated by centrifugation (800 × *g*, 15 min) and the absorbance (A) of the supernatant (100 µL) was measured at 540 nm to detect the released hemoglobin. The total hemoglobin concentration in the supernatant was quantified by the cyanmethemoglobin method [246]. The results were extrapolated from a standard curve, which was generated from a linear fit of hemoglobin standard samples over a range of concentrations (1-80 mg/mL). The results were corrected from the background absorbance of the all the corresponding nanomaterials (at 540 nm) and were expressed as percentage of hemolysis with respect to the positive control.

4.3.8. Leukocyte count

The nanomaterials (0.2 and 1 mg/mL) in PBS buffer (50 µL) were added to the citrated blood (50 µL) and incubated for 30 min at 37°C. PBS buffer was used as the negative control. The sample (20 µL) was then mixed in 3% (v/v) glacial acetic acid in deionized water (380 µL) and the total number of leukocytes was counted using a hemocytometer.

4.3.9. Platelet count

Platelet rich plasma (PRP) was obtained by centrifugation (800 × *g*, 5 min) of citrated blood. The nanomaterials (0.2 and 1 mg/mL) in PBS buffer (50 µL) were mixed to the PRP (50 µL) and incubated for 30 min at 37°C. PBS buffer was used as the negative control. A sample (20 µL) was diluted with 1% (w/v) ammonium oxalate in deionized water (380 µL) and the total number of platelets was determined by using a hemocytometer.

4.3.10. Whole blood clotting time (WBCT)

Fresh blood (50 µL) was mixed with an equal volume of either PBS buffer as a negative control or the nanomaterials (0.2 and 1 mg/mL) in PBS buffer (50 µL) and then incubated at 37°C. After 15 min of incubation, aqueous calcium chloride ($CaCl_2$) solution (50 mM, 25 µL) was added to the blood mixture (100 µL). The WBCT was determined as the time required for clot formation after the addition of $CaCl_2$.

4.3.11. Complement consumption assay

The complement consumption of the nanomaterials was determined as previously described [330]. Briefly, human serum (10 µL) was incubated with the nanomaterials (0.4 and 2

mg/mL) in gelatin veronal buffer (30 µL) for 1 h at 37°C. Zymosan (10 mg/mL) and PBS buffer were used as the positive and negative controls, respectively. The samples (40 µL) were further diluted with gelatin veronal buffer (960 µL) and incubated with an equal volume of antibody sensitized sheep erythrocytes (5×10^8 cells/mL) for 1 h at 37°C. Finally, the unlysed erythrocytes were separated by centrifugation (800 × *g*, 15 min) and the absorbance of supernatants (100 µL) was measured at 415 nm for the released hemoglobin. The intrinsic absorbance of the nanomaterials at 415 nm was corrected by measuring absorbance of equivalent of nanomaterial in gelatin veronal buffer. The percentage of complement consumption was determined using the equation:

$$(C\text{-}C_t)/C \times 100\% \quad \ldots\ldots (24)$$

where C is the total complement consumption of the negative control and C_t is the complement consumption of the test nanomaterial. The term ($C\text{-}C_t$) represents consumption of complement by the test nanomaterials.

4.3.12. *In vitro* uptake by macrophages

The rat peritoneal macrophages were freshly harvested from male Sprague Dawley rats (Charles River Laboratories International, Inc., Wilmington, MA, USA). Briefly, rats (100-125 g) were first euthanized by cervical dislocation and the skins were peeled off to expose the peritoneum. Ice cold DMEM (20 mL) was then injected into the peritoneal cavities and the macrophages were isolated by aspirating the medium. The isolated macrophages were then washed with ice-cold sterile PBS buffer (2 × 5 mL) and then re-suspended in a complete DMEM medium (1 mL) for immediate use. The nanomaterials (0.2 and 1 mg/mL) in PBS buffer (100

μL) were added to the macrophages (1×10^6/mL, 100 μL) and incubated for 3 h at 37°C. The cells were then centrifuged and washed with ice cold PBS buffer (2 × 1 mL). The intracellular contents of the cells were extracted using 10% (v/v) Triton X-100 in acetonitrile (200 μL). The amount of nanomaterials was determined by a fluorometer (Cary Eclipse, Agilent Technologies, Santa Clara, CA) according to the standard curve. The lysate obtained from PBS-treated cells were used to correct the baseline fluorescence. To generate the standard curve, same number of macrophages (1×10^6/mL, 100 μL) were mixed with different amounts of the test materials in PBS buffer (100 μL) and cellular contents were extracted as described before in this section. The uptake of gold nanoparticles was determined indirectly by analyzing the particles in the supernatant as previously described [331].

4.3.13. Pharmacokinetic studies

Three to four week old female, severe combined immunodeficiency (SCID) hairless outbred (SHO-*Prkdc*^{scid}*Hr*^{hr}) mice (approx. weight 20 g) were purchased from Charles River Laboratories (Wilmington, MA, USA). All animal experiments were performed according to the guidelines of the Institutional Animal Care and Use Committees (IACUC) at NDSU. The animals were randomly divided into six groups. Each group of animals (n=3) was administered with one type of nanomaterial (80 μg) in sterile PBS buffer (200 μL) *via* tail-vein injection. At different time points, the blood (40 μL) was collected through the submandibular vein. The plasma (20 μL) was separated from whole blood by centrifugation (5000 × *g*, 15 min) and further diluted with PBS buffer (80 μL). The fluorescence intensity of the diluted plasma was measured by a fluorometer. The amount of nanomaterials was quantified according to a standard curve, which was generated by adding different amounts of the test materials to the plasma of an

untreated mouse. The pharmacokinetic parameters were determined by fitting the percentage of injected dose per milliliter of blood (% ID/mL) versus time (h) curve into a two-compartmental pharmacokinetic model using PK Solver Microsoft Excel plug-in freeware as previously described [332].

4.3.14. *In vivo* imaging studies

For the *in vivo* study, human glioblastoma U87 cells (1×10^6) suspended in complete DMEM medium (50 µL) were injected into the chest region of SCID mice. Tumor growths were measured bi-directionally using a digital caliper and the tumor volumes were determined using the following equation:

$$0.52 \times L \times W^2 \quad \text{.....(25)}$$

Where L is the length and W^2 is the square width. When tumors reached approximately 15 mm^3, the animals were randomized into three different groups (n=3) and were treated with the same mass concentration (80 µg) of NFP-100, PLGA-100, or PS-100 in sterile PBS buffer (200 µL) *via* tail vein injections. *In vivo* imaging was performed in real-time by optical imaging using a reflectance imaging system (*In-vivo* system FX, Carestream Health, Inc., Rochester, NY, USA). The whole body fluorescence images were acquired using the Cy5.5 channel (excited at 615/645 nm and recorded at 680/720 nm) at different time points (0, 1, 4, 12, and 24 h). The images were further processed and merged with respective X-ray images using Kodak molecular imaging software.

4.3.15. Biodistribution study

For biodistribution study, mice (n=3) were euthanized after imaging. The organs were isolated, washed, and snap frozen in liquid nitrogen. The organs were defrosted, weighed (30 mg), and extracted using 1% (w/v) sodium dodecyl sulfate lysis buffer in 150 µL of Tris buffer (20 mM, pH 7.6). To ensure a complete cell lysis, samples were heated to 80°C for 10 min. The fluorescence intensity of tissue extracts (100 µL) was measured by a fluorometer and the amount of nanomaterials was quantified according to the standard curve. The results were corrected for the baseline fluorescence of the corresponding tissue extracts of an untreated mouse. The biodistribution of the nanomaterials in various organs was then calculated and normalized in unit of percentage of injected dose per gram of tissue (% ID/g).

4.3.16. Immunohistochemistry

For immunohistochemistry, the frozen tumors were sliced into thin sections (8 µm) using a cryostat (Tissue-Tek, Sakura Finetek USA, Inc., Torrance, CA, USA). The sections were washed with PBS buffer and then immunostained with Alexa Fluor® 488-conjugated rat anti-mouse CD31 antibody (10 µg/mL) in PBS buffer (500 µL) for blood vessel (CD31). The sections were washed with PBS buffer and nuclear staining was performed by incubating with Hoechst 33342 (1 µg/mL) in PBS buffer (500 µL) for 10 min at room temperature. The slides were observed under an epifluorescence microscope (IX-81, Olympus America, Inc., Melville, NY, USA). The corresponding combination of excitation and emission filters were employed for the visualization of Hoechst (330-385/420 nm), Alexa Fluor® 488 (430-480/500 nm), and Cy5.5 (635-675/716 nm). The images were recorded on a CCD camera (Hirakuchi, Hamamatsu, Japan)

interfaced with a computer and further processed using HCImage software (Hirakuchi, Hamamatsu, Japan).

4.3.17. Statistical analysis

All results were expressed as mean ± standard deviation (SD) of at least triplicate samples. The statistical analysis was performed using Student's *t*-test and analysis of variance (ANOVA) using Prism software version 5.01 (GraphPad software, Inc., La Jolla, CA, USA). The results were considered statistically significant if the *p*-values were < 0.01.

4.4. Results and discussion

4.4.1. Design, synthesis, and characterization of NFP-50, NFP-100, and NFP-400

NFP was composed of multiple peptide constructs ($mPEG_{2470}$-BK(*FITC*)SGRSANA-kldlkldlkldl-$CONH_2$, where the lower case and upper case letters represent the *D*- and *L*-configuration, respectively) [243, 328]. The self-assembling segment (kldlkldlkldl) of NFP was an ionic-complementary amino acid sequence, which was characterized by the presence of alternative hydrophobic (aspartic acid) and hydrophilic (lysine) amino acid residues. In an aqueous environment, multiple peptide constructs would self-assemble to form a single layer NFP (~4 nm in width) *via* electrostatic and hydrophobic interactions [326]. On the other hand, the functions of hydrophilic mPEG were to prevent the individual nanofibers from aggregation [325, 326, 333] and also to improve the blood circulation time *in vivo* [163]. The surface of NFP was covalently conjugated with multiple Cy5.5 fluorophores as the near-infrared (NIR) reporters, *via* the $-NH_2$ groups of the lysine residues **(Figure 34)**. The conjugation was shown to be

successful, as confirmed by the absorbance **(Figure 35A)**. It was estimated that approximately one molecule of Cy5.5 was attached to two peptide constructs.

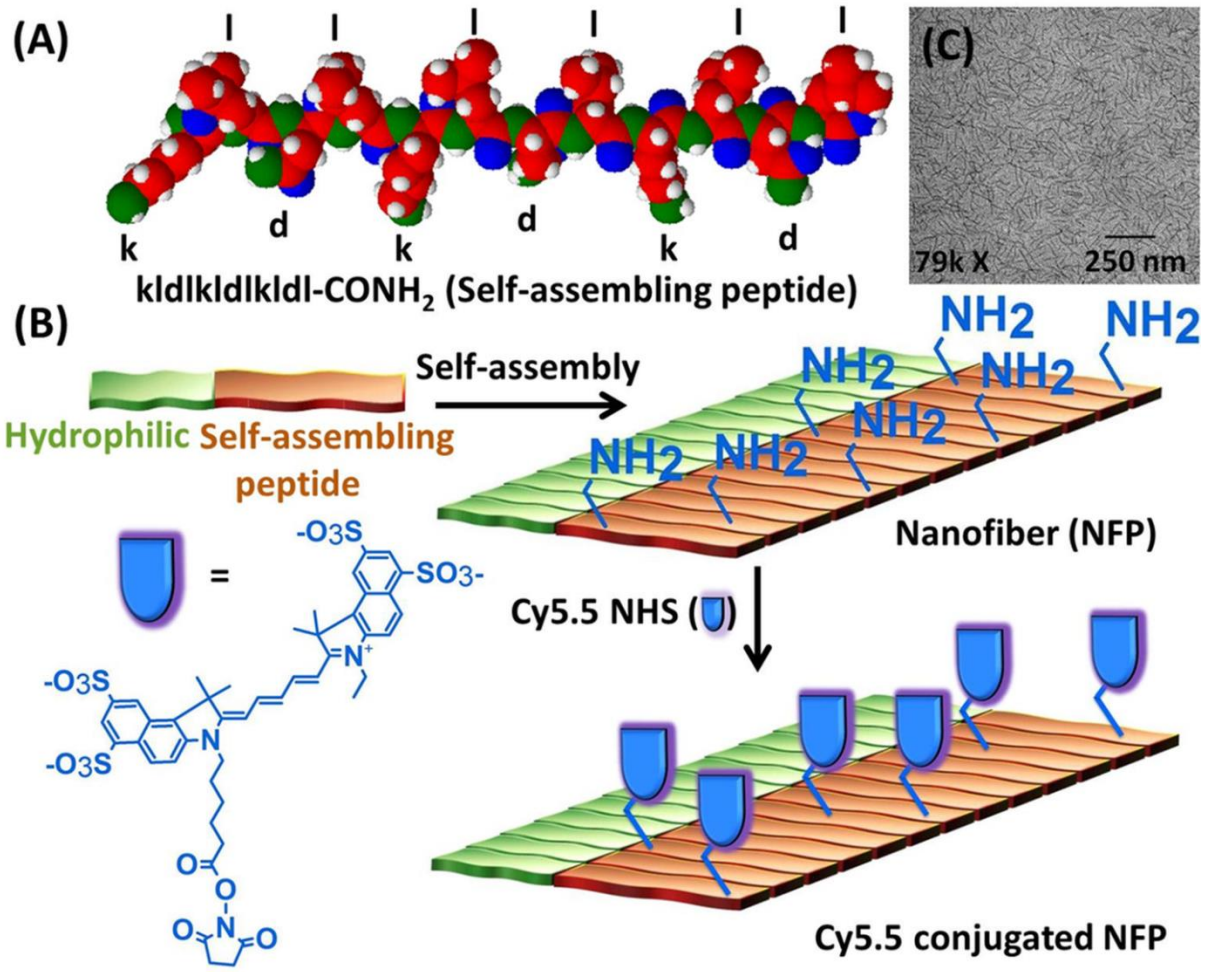

Figure 34. The design of NFP. (A) Molecular model of the self-assembling peptide. Color scheme: red (C), white (H), blue (O), and green (N). (B) Schematic representation of NFP. The basic peptide construct of NFP is composed of the self-assembling peptide (kldlkldlkldl-$CONH_2$) conjugated to a hydrophilic polyethylene glycol (2470 Da). In the aqueous environment, multiple peptide constructs assembled into a nanofiber. The surface of NFP was also conjugated with multiple Cy5.5 fluorophores as the near-infrared (NIR) reporters *via* the -NH_2 groups of the lysine residues. (C) The transmission electron microscope (TEM) image of NFP-100.The fibers were stained with 0.75% (w/w) uranyl formate.

To synthesize NFP of different lengths (50, 100, and 400 nm), the nanofibers were homogenized using a mini-extruder as previously described [243]. The resulting NFP-50, NFP-

100, and NFP-400 were characterized for the morphology and size by transmission electron microscopy [243, 326, 328]. As expected, all the NFPs were homogenous with no sign of aggregation **(Figure 34C)**. The sizes and zeta potentials of all the NFPs were also confirmed by dynamic light scattering **(Table 21)**. The NFP could also serve as a nanocarrier, since a significant amount (26% w/w) of a model drug, such as doxorubicin, could be physically adsorbed on the surface **(Figure 35B)**.

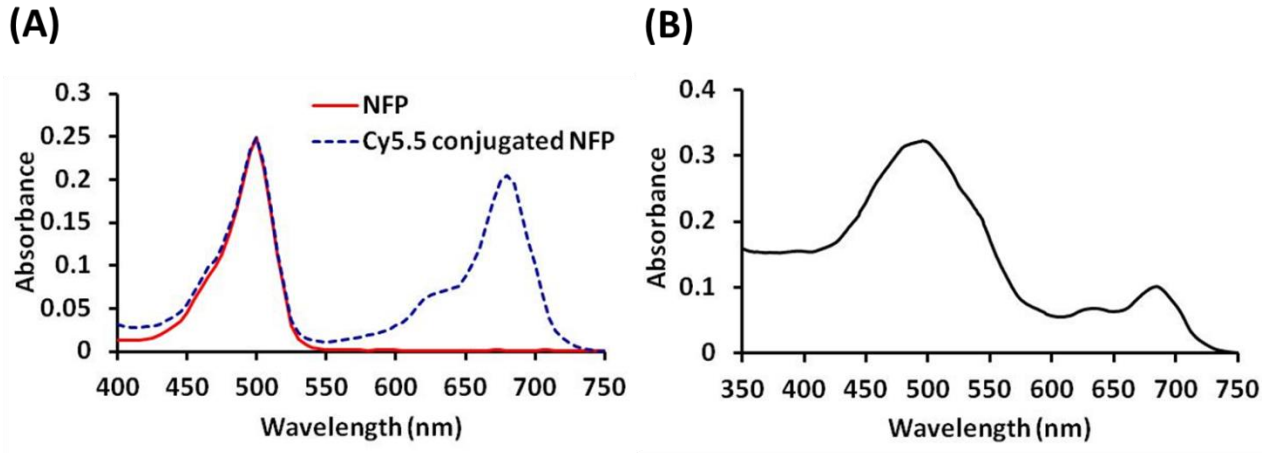

Figure 35. The absorbance spectra of (A) NFP and Cy5.5-conjugated NFP in 95% (v/v) methanol and doxorubicin loaded NFP-Cy5.5 in 70% (v/v) methanol.

Table 21. The physiochemical properties of different nanomaterials.

Nanomaterials	***Material of construction***	***Dimension & Shape***	***Size (nm)***		***Zeta Potential (mV)***
			TEM	***DLS***	
NFP-50	Amino acid	2D Fiber	4 (w) × 50 (l)	51 ± 4 (l)	-10 ± 2.0
NFP-100			4 (w) × 100 (l)	85 ± 5 (l)	-10 ± 2.0
NFP-400			4 (w) × 400 (l)	380 ± 10 (l)	-10 ± 2.0
PLGA-100	PLGA	3D Sphere	70 (d)	93 ± 7 (d)	-15 ± 3.0
AU-60	Gold	3D Sphere	60 (d)*	71 ± 1 (d)	-34 ± 2.5
AU-80			80 (d)*	90 ± 1 (d)	-33 ± 2.5
PS-50	Polystyrene	3D Sphere	50 (d)*	65 ± 2 (d)	-33 ± 2.5
PS-100			100 (d)*	110 ± 3 (d)	-54 ± 4.5
QD-6	Cadmium & Selenium	3D Sphere	6 (d)*	27 ± 2 (d)	-14 ± 1.5
MWCT-2000	Carbon	3D Rod	10 (OD) × 2000 (l)*	2580 ± 150 (l)	-38 ± 3.0

Abbreviations: Poly(D,L-lactic-*co*-glycolic acid)-polyethylene glycol (PLGA), transmission electron microscopy (TEM), dynamic light scattering (DLS), outside diameter (OD), width (w), length (l), diameter (d). * Size determination by TEM was provided by the manufacturer.

4.4.2. Cytotoxicity studies

Depending on the cell type, a nanomaterial may induce cell death through different pathways [334, 335]. To investigate the biocompatibility of NFP, we performed MTS assays in both mouse leukemic monocyte macrophage (RAW 264.7) and human embryonic kidney (HEK-293) cell lines. The nanomaterials that showed toxicity exhibited a more profound effect towards the phagocytic RAW 264.7 than the non-phagocytic HEK-293 cell lines **(Figure 36)**.

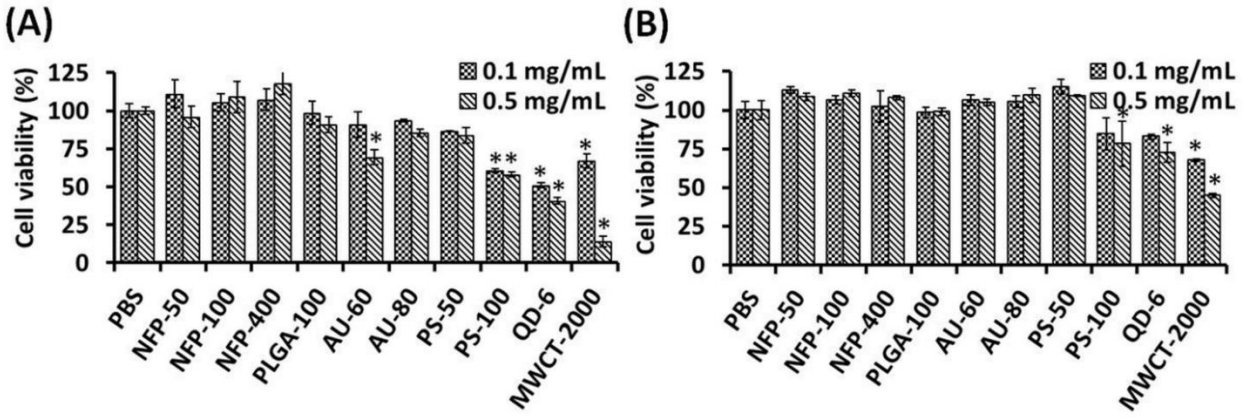

Figure 36. MTS assay. The nanomaterials were incubated with (A) RAW 264.7 and (B) HEK-293 cells for 24 h. Cell viability was measured by the MTS assay. * Significant as compared to PBS control ($P < 0.05$).

Both the quantum dots (QD) and multi-walled carbon nanotubes (MWCT) were toxic, with less than 60% of the RAW 264.7 cells remaining viable after 24 h of incubation. The results were expected, since these nanomaterials are known to induce oxidative stress and to cause damage of the cell membranes [336]. Interestingly, the toxicity of the polystyrene nanoparticles (PS) increased with their size, presumably because the larger particles were more prompt to be taken up by the cells than the smaller ones [336]. On the other hand, both the pegylated poly(D,L-lactic-*co*-glycolic acid) nanoparticles (PLGA) and the gold nanoparticles (AU) showed only marginal decreases in the cell viability (< 10%). Unlike the carbon nanotubes where the toxicity

can be affected by aspect ratio [130], all the NFPs, regardless of the length, were found to be nontoxic.

4.4.3. Hemocompatibility studies

A nanomaterial that causes damage to red blood cells (RBC) can be life-threatening [246]. Here, we performed an *in vitro* hemolysis assay to investigate whether NFP was hemocompatible [246]. Triton X-100 and phosphate buffered saline (PBS) were employed as the positive and negative controls, respectively. In all cases, the percentage of hemolysis increased with the concentration of nanomaterials **(Figure 37A)**. NFP exhibited the minimum hemolytic effect when comparing to other nanomaterials but the degree of hemolysis was inversely increased with the length, in the order of NFP-400 (1.0%) < NFP-100 (3.0%) < NFP-50 (3.8%). In contrast, AU, PS, and QD caused significant damage to the RBC (> 5%). MWCT-2000 was highly hemolytic (> 50%). This result was in agreement with the previous report that MWCT could destabilize the cell membranes and, subsequently, causing the damage to RBCs [337].

Next, we evaluated the effect of NFP on the leukocyte and platelet numbers, as certain nanomaterials can induce leukopenia or thrombus formation, mainly caused by platelet aggregation. Our results demonstrated that all the tested nanomaterials, except MWCT, did not affect the leukocyte and platelet counts **(Figure 37B and C)**. The decrease in the platelet number in the presence of MWCT-2000 (20%) was attributed to the platelet aggregation that induced by the activation of glycoprotein integrin receptor [338]. To confirm that NFP would not induce blood clotting *via* the activation of coagulation system, we investigated its effect on blood clotting time. Our result showed that NFP did not affect the whole blood clothing time (WBCT) **(Figure 37D)**. In contrast, we recorded a significant delay of the WBCT in presence of QD-6,

with a 2.4-fold increase when comparing to the PBS control ($P < 0.05$). This result was contradicted to the previous report that quantum dots could promote thrombosis [339]. This might be due to fact that the size and zeta potential of the quantum dots used in our studies were different as compared to reported studies.

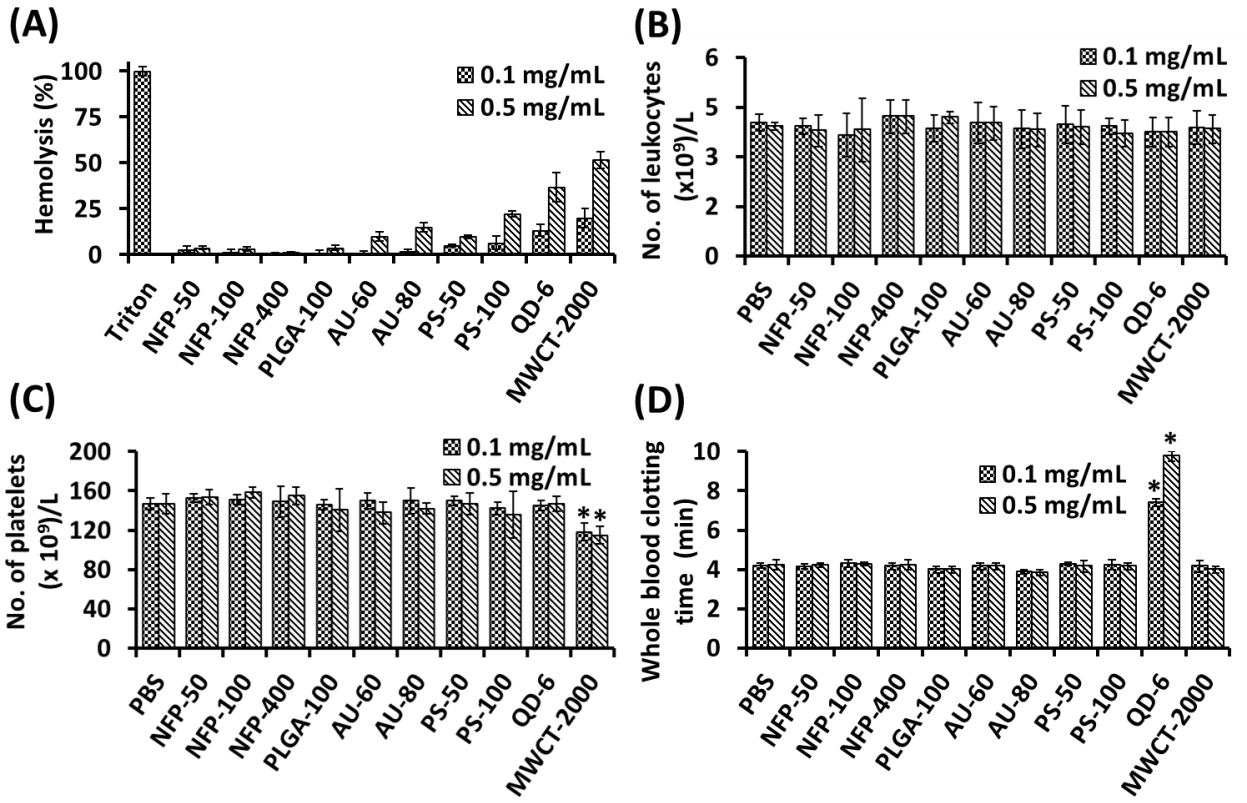

Figure 37. Hemocompatibility studies (A) Hemolysis assay. The nanomaterials were incubated with RBCs and the release of hemoglobin was quantified by the cyanmethemoglobin method. The results were expressed as the percentage of hemolysis with respect to the positive control (Triton X-100). A comparison of the effects of different nanomaterials on (B) leukocyte number, (C) platelet number, and (D) whole blood clotting time (WBCT). * Significantly higher as compared to NFP-50, NFP-100, and NFP-400 ($P < 0.05$).

Based on the new "Standard Test Method for Analysis of Hemolytic Properties of Nanoparticles" from the American Society for Testing and Materials (ASTM) E 2524-08 [246], we concluded that NFP was hemocompatible, since it was non-hemolytic (< 5% hemolysis) and show no significant effect on the leukocyte and platelet numbers and the WBCT.

4.4.4. Complement consumption assay

After intravenous injection, a circulating nanomaterial that binds to complement proteins may induce hypersensitivity reactions such as complement-mediated anaphylaxis. Here, we determined the consumption of complement proteins by NFP using a CH50 assay [330]. Zymosan, a well-known complement system activator, was used as a positive control. Among all the nanomaterials, NFP showed the minimum complement consumption (< 11%). This was attributed to the presence of hydrophilic PEG chains that might prevent the absorption of proteins onto the nanofiber surfaces. On the other hand, both the PS and MWCT significantly consumed 25-40% of the CH50 units **(Figure 38A)** [340, 341]. Overall, these results suggested that NFP were unlikely to trigger the complement cascade as compared to other nanomaterials.

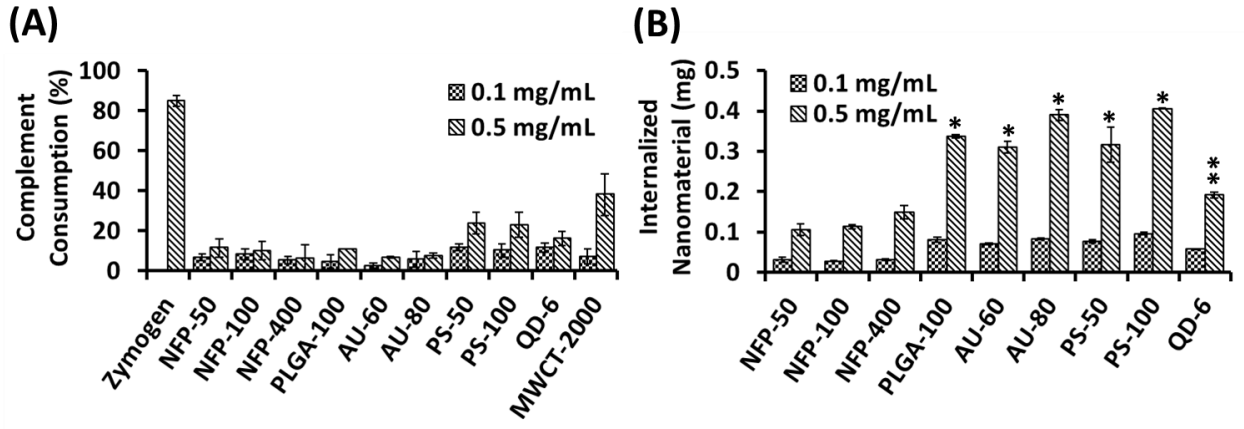

Figure 38. (A) Complement consumption assay. A bar chart showing the percentage of complement consumption by different nanomaterials. (B) *In vitro* macrophage uptake assay. The same number of freshly isolated rat peritoneal macrophages (1×10^6/mL) was incubated with the nanomaterials in complete DMEM medium for 3 h at 37°C. The intracellular contents of cells were extracted and quantified by a fluorometer. # Significant as compared to the PBS control ($P < 0.05$). * Significantly higher as compared to NFP-50, NFP-100, and NFP-400 ($P < 0.05$). ** Significantly higher as compared to NFP-50 and NFP-100 ($P < 0.05$).

4.4.5. *In vitro* uptake by macrophages

A nanomaterial that is taken up by circulating macrophages normally has a lesser chance of reaching the target sites [82]. To predict the uptake of NFP *via* phagocytosis, we performed an *in vitro* uptake assay using freshly isolated rat peritoneal macrophages **(Figure 38B)**. We observed that significant ($P < 0.05$) amounts of AU and PS were taken up by the macrophages (>70%), presumably because these nanoparticles were extremely hydrophobic [342, 343]. Among all the nanomaterials, NFPs demonstrated the least uptake by the macrophages (< 30%), whereas a significant ($P < 0.05$) amount of spherical PLGA nanoparticles were taken up by the macrophages (67%). The observed differences in phagocytic uptakes could be due to differences in the total PEG content. As the NFP contains relatively higher PEG content (50 vs. 13% w/w) and thus providing better protection against macrophage uptake when compared with the PLGA nanoparticles [344]. In addition, since the NFP is a single layer fiber like structure **(Figure 34B)**, nearly all the PEG chains could expose toward the nanofiber surface and, thus, creating a uniform and dense PEG shield. Whereas, in case of the PLGA nanoparticles, some of the hydrophilic PEG chains could be buried inside the core of nanoparticles during nanoprecipitation [345]. Given that the shape of the nanomaterial can also play a crucial role in the phagocytosis, a relatively lower uptake of NFP suggested that the macrophages required a longer membrane wrapping time for NFP than the spherical nanomaterials [320, 346].

4.4.6. Pharmacokinetic studies

It is well known that immune cells in the blood (such as leukocytes, platelets, and monocytes) and in tissues (such as macrophages) have a tendency to engulf and eliminate the nanomaterials from the systemic circulation. Here, we investigated the pharmacokinetic of NFP. The physical pharmacokinetic parameters were obtained by fitting our data into a two-compartment model **(Table 22)**. All the NFPs, regardless of the length, showed a biphasic plasma clearance profile ($R^2 > 0.99$) **(Figure 39A)**. The elimination half-life ($t_{1/2\beta}$) of NFP-100 was short (3.9 h) but was longer than both NFP-50 (1.3 h) and NFP-400 (2.6 h), possibly because of the shorter NFP-50 was rapidly eliminated by renal clearance and the longer NFP-400 was more likely to be removed by circulating macrophages **(Figure 39B)** and the RES organs.

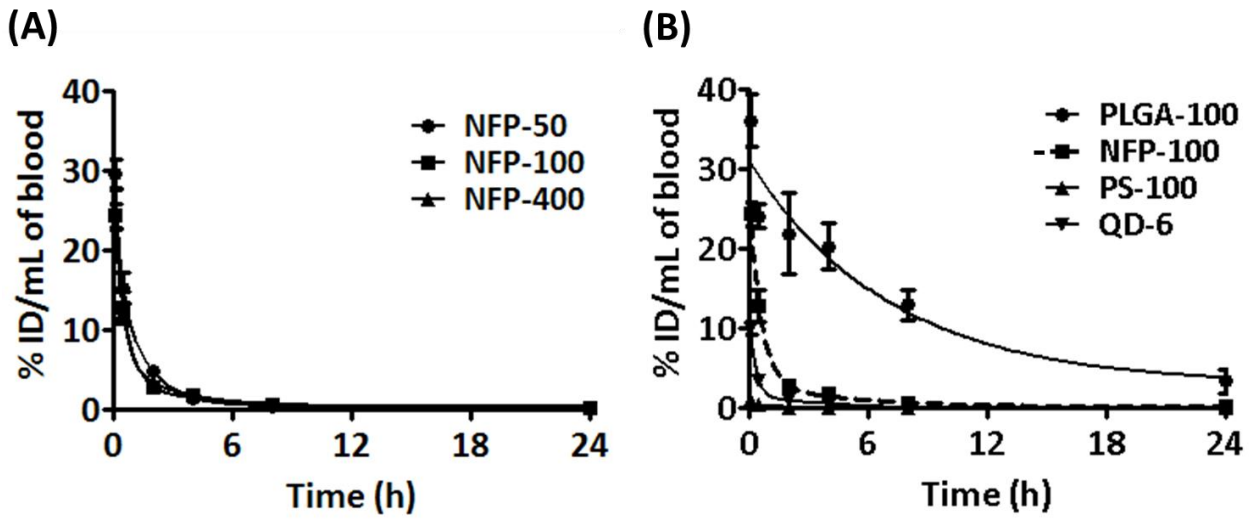

Figure 39. Pharmacokinetic study. (A) A plot of the pharmacokinetic profile of NFPs. (B) A comparison of the pharmacokinetic profile among NFP-100, PLGA-100, PS-100, and QD-6. All the nanomaterials (80 µg) in sterile PBS buffer (200 µL) were intravenously administered into SCID mice (n=3 for each group of animals). The data were plotted as a percentage of injected dose in blood (% ID/mL) versus time.

We then compared the pharmacokinetic profile of NFP-100 to other 3D nanoparticles of similar size (100 nm). As expected, the pegylated PLGA-100 showed a longer $t_{1/2\beta}$ (8.7 h) as compared to the non-pegylated PS-100 (1.4 h), since coating a hydrophilic PEG on the nanoparticle surface might minimize the plasma clearance. As expected, the area under the curve (AUC) and mean residence time (MRT) were also significantly higher in the case of PLGA-100 **(Table 22)**. It is important to note that despite of higher PEG content, NFP-100 showed a relatively shorter $t_{1/2\beta}$ than PLGA-100. This could be attributed to the fact that NFP had a narrow width (4 nm) and therefore eliminated rapidly by renal clearance [347].

Table 22. The pharmacokinetic parameters of the nanomaterials.

Nanomaterials	***$t_{1/2\,(\alpha)}$ (h)***	***$t_{1/2\,(\beta)}$ (h)***	***$AUC_{0\text{-}24\,h}$ (h. μg/mL)***	***MRT (h)***	***CL (mL/h)***	***V_d (mL)***
NFP-50	0.26	1.3	26.2	1.6	2.5	1.7
NFP-100	0.41	3.9	24.6	3.4	2.5	7.1
NFP-400	0.32	2.6	24.2	2.6	3.3	5.2
PLGA-100	0.03	8.7	254	12.5	0.3	2.3
PS-100	0.15	1.4	0.70	1.5	158.7	95.9
QD-6	0.21	1.9	6.50	1.9	11.9	13.5

Abbreviations: Distribution half-life ($t_{1/2\alpha}$), elimination half-life ($t_{1/2\beta}$), area under the curve (AUC), mean residence time (MRT), clearance (*CL*), and volume of distribution (V_d).

4.4.7. *In vivo* imaging and biodistribution studies

It is possible that, after intravenous injection, a nanomaterial can be taken up by a circulating macrophage or captured in the liver [82]. Therefore, we investigated the tissue distribution of NFP in a human glioblastoma U87-implanted SCID mouse model by fluorescence imaging **(Figure 40)**. NFP-100 was chosen as an optimized formulation in this study, since it had the lower macrophage uptake **(Figure 38B)** as well as possessed the longest elimination plasma half-life ($t_{1/2\beta}$ =3.9 h) among all the NFPs and, thus, considered more suitable for *in vivo* applications. We also compared NFP-100 with the spherical nanomaterials i.e. PLGA-100 and

PS-100 of similar size (100 nm). For a fair comparison, the same amounts of nanomaterials were injected into the animals and the distribution in the major organs including liver, spleen, bladder, and tumor were monitored non-invasively by fluorescence imaging.

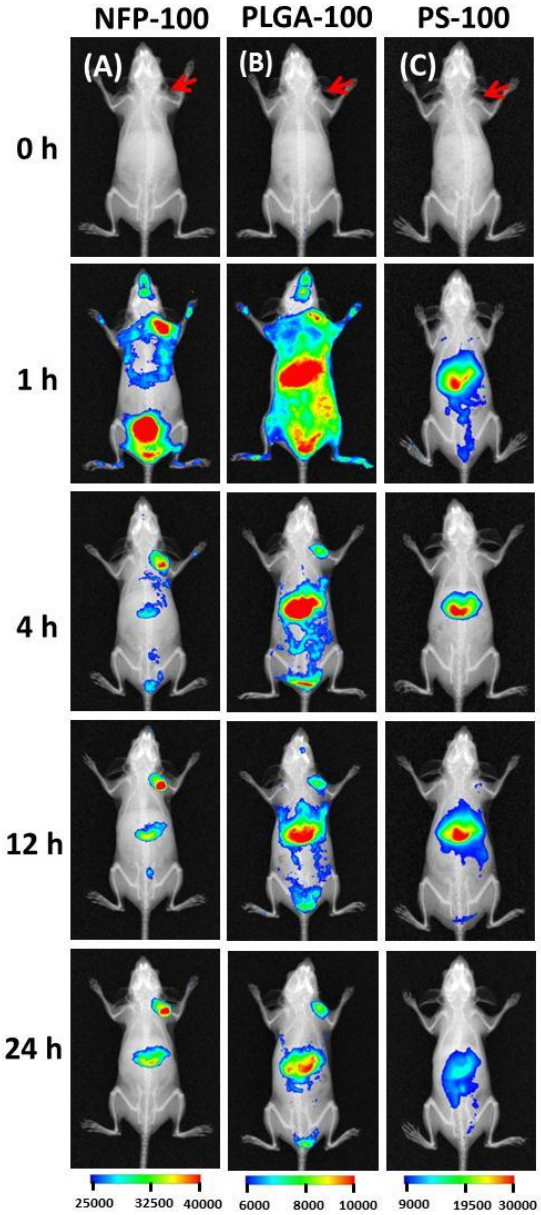

Figure 40. Biodistribution study. The merged fluorescence and X-ray images of U87-implanted SCID mice (n=3 for each group of animals) at different time points after intravenous administration of the same amount (80 μg) of (a-d) NFP-100, (e-h) PLGA-100, and (i-l) PS-100 in sterile PBS buffer (200 μL).

Both the PLGA-100 and PS-100 were found predominantly accumulated in the liver within 1 h of injection. On the other hand, NFP-100 was efficiently delivered to the tumor site **(Figure 40)**, despite the fact that a substantial amount was present in the bladder which suggest that NFP-100 was also rapidly eliminating by renal clearance [84]. This strongly suggested that a rapid translocation of NFPs from the vascular compartment to the urine compartment through glomerular filtration [347]. Interestingly, NFP-100 remained in the tumor at a considerably high level with time **(Figure 40)**. Overall, our imaging data confirmed the results from the pharmacokinetic study that NFP-100 has a short distribution half-life (< 1 h).

To further quantify the amount of nanomaterial in each organ, all the animals were then euthanized at 24 h after injection. The whole organs were removed, homogenized, and further quantified for the amount of nanomaterials in the tissue extracts **(Figure 41A and B)**. As expected, > 30% of the injected dose (ID/g of tissue) was found in the livers of the animals injected with PLGA-100 and PS-100 ($P < 0.05$). On the other hand, there was a higher percentage of NFP-100 accumulated in the tumors (5%) when compared to PLGA-100 (2.5%) and PS-100 (0.4%).

In order to have a better understanding of the overall distribution, the percentage of injected nanomaterials remaining in the animals was calculated. After taking account for the tissue mass and blood volume (assuming the weight of the blood was 6% of the total body weight), the percentage of NFP-100 remaining (22%) at 24 h after injection was considerably lower than both the PLGA-100 (50%) and PS-100 (70%). Our results suggested that NFP-100 could deliver to the tumor more effectively but at the same time was less likely to accumulate in the body when compared to other spherical nanoparticles.

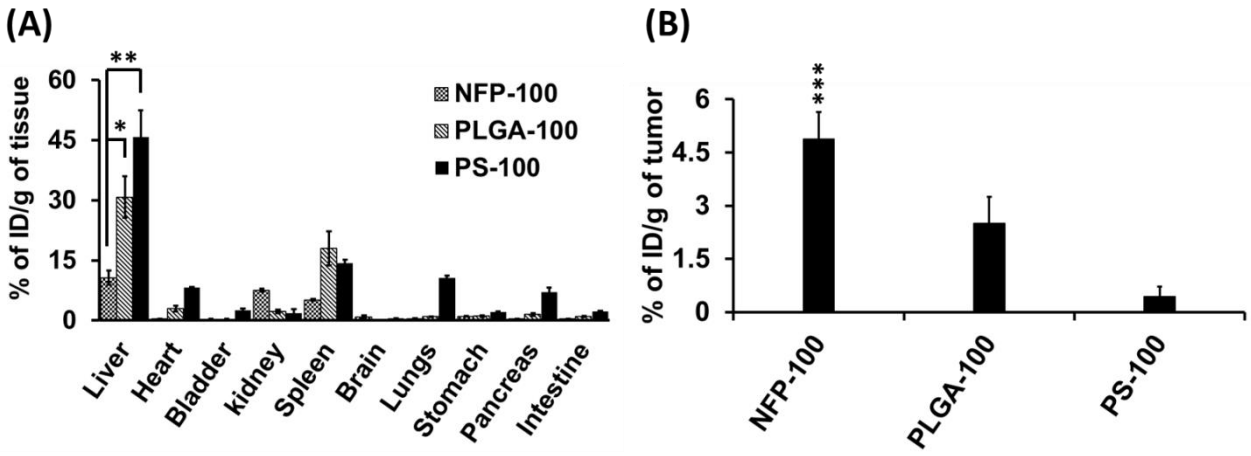

Figure 41. Quantitative tissue distribution of nanomaterials. (A) A bar chart shows the percentage of injected dose (% ID/g of tissue) in (A) different organs and (B) tumors. The nanomaterials were extracted from the organs and quantified by a fluorometer. * Significantly higher as compared to NFP-100 ($P < 0.05$). ** Significantly higher as compared to NFP-100 ($P < 0.01$). *** Significantly higher as compared to PLGA-100 and PS-100 ($P < 0.05$).

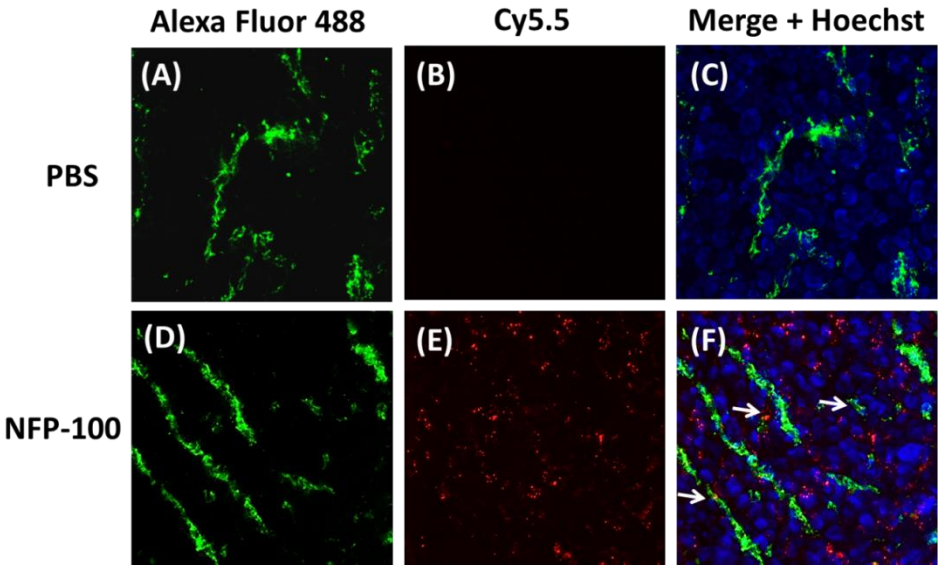

Figure 42. Fluorescence microscopy. Fluorescence images showing the excised tumors of U87-implanted SCID mice at 24 h after injection with (A-C) PBS buffer and (D-F) NFP-100. The tumor sections (8 μm) were immunostained with Alexa Fluor® 488-conjugated rat anti-mouse CD31 antibody (green) and Hoechst 33342 (blue) for visualization of the blood vessel and nucleus, respectively. The NFP-100 (red) was found located at the blood vessels and the surrounding tumor.

Finally, fluorescence microscopy was performed on the excised tumors to confirm the presence of NFP-100 in the tumor **(Figure 42)**. The NFP-100 (red fluorescence) appeared to localize in the tumor blood vessels (green fluorescence) and extravasated into the surrounding tumor tissue. Our results suggested that NFP could penetrate deeply inside the tumor. This indicates that NFP could be potentially useful as a vector in poorly permeable tumors, where nanoparticles entry is mainly restricted due to their hypovascular and hypopermeable characteristics [348].

4.5. Conclusion

Using long circulating nanoparticles may be a promising approach to enhance the therapeutic efficacy of chemotherapeutic agents [160, 311-314] but at the same time it may also give rise to long-term toxicity because of the extended circulation time. Furthermore, the delivery of the particles from the systemic circulation to tumor interstitium can be slow, depending on the size of the particles [348]. Here, we reported a NFP that could be delivered to the tumor after intravenously injection in a short period of time and also eliminated rapidly by renal clearance. Our *in vitro* studies confirmed that the NFPs were nontoxic and biocompatible. Most importantly, the NFPs showed a higher tumor accumulation than some spherical nanoparticles with the same size and thus they may offer a safer and more effective drug delivery approach [160]. Given the unique pharmacokinetic and biodistribution, we believe that these NFPs could be also a useful carrier for contrast agents, since a rapid clearance may offer a lower signal-to-background ratio in imaging [349]. In the future, specific ligands such as antibodies, proteins, and aptamers could be immobilized on the nanofiber surfaces for targeting delivery. Overall, we believe that the developed NFPs form a versatile theranostic platform, which

promises a more efficient delivery of the payload to the tumor. This study also may provide useful information for the design of nanomaterials in the future.

CHAPTER 5. SUMMARY AND FUTURE DIRECTIONS

The application of nanotechnology for the delivery of diagnostic and therapeutic agents has exerted considerable impact on medicine in the past few decades [350]. The unique physiochemical properties of nanomaterials open the possibility of interaction with biological tissues, spurring the emergence of the field of bionanotechnology and the creation of nanoparticle-based therapeutics, *in vitro* diagnostics, and *in vivo* contrast agents. Using nanotechnology, one can prolong the circulation of hydrophobic small molecules or macromolecules in blood plasma, tailor their delivery to specific tissues or intracellular locations, and even visualize sites of delivery by combining therapeutic agents with imaging modalities and many other applications. Over 20 nanoparticle-based therapeutics are already approved by the FDA for clinical use, and numerous others are at various stages of preclinical and clinical development. Among all, polymer-based nanomaterials have been studied extensively and imparted huge success in clinical use in delivering the different therapeutic agents. However, the nanomedicine field still lacks the use of nanomaterials for the diagnostic applications particularly for optical imaging. This dissertation employs several polymeric based nanomaterial formulations for the delivery of diagnostic agents for medical imaging. All the nanomaterials were synthesized in house by using either polymeric construct or peptide/polymer construct. As desired, the nanomaterials were then modified with different targeting ligands to achieve the specificity.

In chapter 2, FRET based polymeric nanoparticles were designed and successfully employed for *in vivo* NIR and FRET imaging. The preliminary experiments with a single fluorophore-doped nanoparticles were the starting point for determining the optimal conditions such as fluorophore loading, particle size, and zeta potential for the encapsulation of the

fluorophores. After initial experimentations, two fluorophores-doped nanoparticles were shown to demonstrate FRET using DiD as a donor fluorophore and DiR as a acceptor fluorophore. With the encapsulation of hundreds to thousands of fluorophore molecules, these nanoparticles showed efficient energy transfer which could be further fine-tuned by changing total fluorophore loading. When compared with DiR-doped nanoparticles, optimized FRET-NPs (2.10% w/w) have shown no advantages in terms of the detection sensitivity and the ability to increase the contrast between the tested sample and the animal. Therefore, the raw FRET images were further processed by using a mathematical model. The experimental results showed a significant improvement of the signal-to-phantom background ratio (from 1:11 to 1:39) post processing. It was hypothesized that this marked improvement in signal-to-noise was due to removal of the fractional cross-talk of the fluorophores and reduced the background contributed by the phantom. This will open up many possibilities for in vivo optical imaging especially for deep tissues, as current optical imaging techniques are unable to reach sufficient penetration depth. The next step would be to employ these nanoparticles for the detection of human tumor in preclinical mouse xenograft model (such as subcutaneous and orthotropic). The delivery of nanoparticles can be achieved by both passive and active targeting approaches. For achieving the targeting specificity, the surface of nanoparticles may be modified with different targeting ligands such as monoclonal antibody, peptide, or aptamers. This should be a relatively simple task as we already demonstrated the successful conjugation of IgG antibodies on the particle surfaces. The potential drawbacks of the present system may include the following: 1) long term instability under *in vivo* conditions, 2) uptake by circulating macrophages and then clearance by excretory organs such as liver and spleen, and 3) *in vivo* biocompatibility. If required, the composition of nanoparticles

such as length of PEG chains, terminal functional groups, and composition of PLGA polymer should be optimized to achieve the desired effect.

In chapter 3, after successfully demonstrating the use of FRET-based nanoparticles for *in vivo* imaging, we further extended the study toward the rational development of multiple fluorophores doped nanoparticles for multicolor imaging and multiplexing imaging. In this design, we incorporated up to four different fluorophores inside a single nanoparticle to create a library of color coded nanoparticles with a single excitation wavelength. It was observed that there was involvement of both sequential and multiple FRET cascade inside the nanoparticles. We further demonstrated that by using the different combinations, numbers, and concentrations of the fluorophores, the optical properties of the particles could be fine-tuned for multicolor imaging and multiplexing imaging. We further examined the ability of distinguish different cell types by using color coded nanoparticles that contained various types of targeting ligands. To allow fair comparison, all the nanoparticles shared a near constant targeting ligand density (~ 30-40 per particle). With multiple copies of targeting ligands, these nanoparticles can bind to surface receptors overexpressed on cancer cells at a much higher affinity than the unmodified nanoparticles counterpart. Importantly, in complex mixture of cells, nanoparticles can only bind and internalize into target cancer cells in significant amount to allow identification of specific cell type using a single excitation wavelength. Preliminary animal studies showed that after subcutaneous injection the particles can be easily applied in *in vivo* multiplexing applications. The next step would be to apply these particles for identifying multiple cell types or tissue structures *in vivo* in multiplexing format.

A major challenge in multi-color FRET is the involvement of large number of donor to acceptor photon pathways present in multicomponent system. As the number of fluorophores increases, the number of possible donor to acceptor pathway increases. For examples, in case of three-fluorophores doped nanoparticles (T1-T5) in our system, following six different pathways might be possible after a single excitation at 485 nm: 1) DiO excitation and emission, 2) Dil excitation and emission, 3) DiD excitation and emission, 4) DiO excitation-Dil emission, 5) DiO excitation-DiD emission, and 6) Dil excitation-DiD emission. Each of these photon transfer pathways represent different routes of energy migration and therefore in-detail mechanistic studies will be required to elucidate the contribution of each energy pathway. The future studies should include fluorescence lifetime studies, donor and acceptor based FRET efficiency, and FRET ratio determination in case of three and four fluorophores doped nanoparticles.

Another future study should include the possible role of the PLGA-PEG polymeric chains in assisting the long-range energy transfer. As our results indicated with the nanoparticles entrapped with DiO and DiR fluorophores, there was a long range energy transfer from DiO to DiR fluorophores. Since, the overlap between the emission spectra of DiO and absorption spectra of DiR was very small (<7%), therefore only small amount of emitted light from DiO fluorophores was sufficient to excite the DiR molecules. There was also the possibility of electron transfer through polymeric chains. Therefore, the possible role of PLGA-PEG polymeric chains in assisting the long-range energy transfer should be evaluated.

The chapter 4 describe the evaluation of peptide-based nanofiber (NFP) as a cargo for tumoral delivery. Here, systematic *in vitro* studies were carried out to evaluate the biocompatibility of NFP. The preliminary *in vitro* results suggested that the NFP is non-toxic and

compatible with most of the blood components. Although significant progress has been made toward understanding the system, other areas of research should be addressed before successful implementation of the developed NFP in the imaging and drug delivery field. The future studies should address in-detail *in vitro* studies for sterility testing (i.e. detection of endotoxin, microbial, and mycoplasma contamination), immunological testing (i.e. leukocyte proliferation assay, chemotaxis assay, granulocyte macrophage colony-forming unit assay, induction of leukocyte procoagulant activity), and toxicity studies (i.e. oxidative stress, cytotoxicity (necrosis and apoptosis), and autophagy). In addition, the *in vivo* compatibility in animals cannot be underestimated. Therefore, the acute, sub-acute, and chronic toxicity studies must be carried out to investigate the *in vivo* biocompatibility of NFP in future. These studies should include determination of maximum tolerated dose (MTD) in animals, single or repeat-dose toxicity, blood sample examinations (serological, hematological, and histopathological), and histological examination of mouse tissues after NFP injection.

The *in vivo* tissue distribution studies in mouse xenograft model showed that NFP could be delivered to the tumor site more effectively within a very shorter period of time and the undelivered NFP was rapidly eliminated by renal clearance. This property of NFP could be beneficial for drug delivery applications because it may avoid the undesirable uptake inside the body, and the dose dependent adverse effect could be circumvented. Therefore, future studies should investigate the utility of NFP as a delivery cargo for the therapeutic agent such as doxorubicin. Given the unique properties of NFP, we believe that nanofibers could improve the efficacy and safety of doxorubicin.

The avoidance of the reticuloendothelial system (RES) uptake has long been a key consideration in designing nanoparticles to achieve prolonged circulation. Biodistribution studies have shown that there was very minimal uptake of NFP by the reticuloendothelial system including liver and spleen. It is well known that beside the size, the geometry of nanomaterials can dictate the uptake of micro- and nanosized objects by macrophages *in vitro*. In animal model, PEGylated gold nanorods demonstrate more effective evasion of uptake by the liver and spleen than PEGylated gold nanoparticles. Therefore, careful elucidation of the effect of particle geometry on RES clearance of NFP should be evaluated.

Lastly, our preliminary studies showed that doxorubicin can be physically adsorbed on surface of NFP **(Figure 35)**. The potential limitations associated with this NFP-DOX complex could be stability of in blood stream after intravenous injection. Therefore, long term stability studies including changes in physical characteristics (such as size, shape, zeta potential), interaction with plasma proteins, and stability in whole blood should be carried out. If required, the doxorubicin can be immobilized on the NFP surface *via* covalent bonding. After *in vitro* studies, the results can be extended to examine the pharmacological behavior of NFP-based therapeutics in disease animal models (e.g., cancer).

REFERENCES

[1] Lowik CW, Kaijzel E, Que I, Vahrmeijer A, Kuppen P, Mieog J, et al. Whole body optical imaging in small animals and its translation to the clinic: intra-operative optical imaging guided surgery. European journal of cancer. 2009;45 Suppl 1:391-3.

[2] Schulz RB, Semmler W. Fundamentals of optical imaging. Handbook of experimental pharmacology. 2008:3-22.

[3] van de Ven SM, Mincu N, Brunette J, Ma G, Khayat M, Ikeda DM, et al. Molecular imaging using light-absorbing imaging agents and a clinical optical breast imaging system--a phantom study. Molecular imaging and biology : MIB : the official publication of the Academy of Molecular Imaging. 2011;13:232-8.

[4] Johnson LJ, Chung W, Hanley DF, Thakor NV. Optical scatter imaging detects mitochondrial swelling in living tissue slices. NeuroImage. 2002;17:1649-57.

[5] Yang M, Baranov E, Jiang P, Sun F-X, Li X-M, Li L, et al. Whole-body optical imaging of green fluorescent protein-expressing tumors and metastases. Proc Natl Acad Sci U S A. 2000;97:1206-11.

[6] Richards-Kortum R, Sevick-Muraca E. Quantitative optical spectroscopy for tissue diagnosis. Annu Rev Phys Chem. 1996;47:555-606.

[7] Ke S, Zhang F, Wang W, Qiu X, Lin J, Cameron AG, et al. Multiple target-specific molecular imaging agents detect liver cancer in a preclinical model. Current molecular medicine. 2012;12:944-51.

[8] Bremer C, Ntziachristos V, Weissleder R. Optical-based molecular imaging: contrast agents and potential medical applications. European radiology. 2003;13:231-43.

[9] Zhang Y, Hong H, Engle JW, Yang Y, Theuer CP, Barnhart TE, et al. Positron emission tomography and optical imaging of tumor CD105 expression with a dual-labeled monoclonal antibody. Mol Pharm. 2012;9:645-53.

[10] Briat A, Wenk CHF, Ahmadi M, Claron M, Boturyn D, Josserand V, et al. Reduction of renal uptake of 111In-DOTA-labeled and A700-labeled RAFT-RGD during integrin αvβ3 targeting using single photon emission computed tomography and optical imaging. Cancer Sci. 2012;103:1105-10.

[11] Melancon MP, Wang Y, Wen X, Bankson JA, Stephens LC, Jasser S, et al. Development of a macromolecular dual-modality MR-optical imaging for sentinel lymph node mapping. Investigative radiology. 2007;42:569-78.

[12] Koyama Y, Talanov VS, Bernardo M, Hama Y, Regino CA, Brechbiel MW, et al. A dendrimer-based nanosized contrast agent dual-labeled for magnetic resonance and optical fluorescence imaging to localize the sentinel lymph node in mice. Journal of magnetic resonance imaging : JMRI. 2007;25:866-71.

[13] Weissleder R, Ntziachristos V. Shedding light onto live molecular targets. Nature medicine. 2003;9:123-8.

[14] Hilderbrand SA, Weissleder R. Near-infrared fluorescence: application to in vivo molecular imaging. Current opinion in chemical biology. 2010;14:71-9.

[15] Luo S, Zhang E, Su Y, Cheng T, Shi C. A review of NIR dyes in cancer targeting and imaging. Biomaterials. 2011;32:7127-38.

[16] Georgakoudi I, Quinn KP. Optical Imaging Using Endogenous Contrast to Assess Metabolic State. Annu Rev Biomed Eng. 2012;14:351-67.

[17] Georgakoudi I, Jacobson BC, Muller MG, Sheets EE, Badizadegan K, Carr-Locke DL, et al. NAD(P)H and collagen as in vivo quantitative fluorescent biomarkers of epithelial precancerous changes. Cancer Res. 2002;62:682-7.

[18] Ghadially FN. Red fluoescence of experimentally induced and human tumours. The Journal of pathology and bacteriology. 1960;80:345-51.

[19] Ghadially FN, Neish WJ. Porphyrin fluorescence of experimentally produced squamous cell carcinoma. Nature. 1960;188:1124.

[20] Ko AC, Ridsdale A, Smith MS, Mostaco-Guidolin LB, Hewko MD, Pegoraro AF, et al. Multimodal nonlinear optical imaging of atherosclerotic plaque development in myocardial infarction-prone rabbits. Journal of biomedical optics. 2010;15:020501.

[21] Provenzano PP, Inman DR, Eliceiri KW, Knittel JG, Yan L, Rueden CT, et al. Collagen density promotes mammary tumor initiation and progression. BMC medicine. 2008;6:11.

[22] Le TT, Rehrer CW, Huff TB, Nichols MB, Camarillo IG, Cheng JX. Nonlinear optical imaging to evaluate the impact of obesity on mammary gland and tumor stroma. Molecular imaging. 2007;6:205-11.

[23] Poulsom R, Pignatelli M, Stetler-Stevenson WG, Liotta LA, Wright PA, Jeffery RE, et al. Stromal expression of 72 kda type IV collagenase (MMP-2) and TIMP-2 mRNAs in colorectal neoplasia. The American journal of pathology. 1992;141:389-96.

[24] Clark GW, Ireland AP, DeMeester TR. Dysplasia in Barrett's esophagus: diagnosis, surveillance and treatment. Digestive diseases. 1996;14:213-27.

[25] Shimasaki H, Ueta N, Privett OS. Isolation and analysis of age-related fluorescent substances in rat testes. Lipids. 1980;15:236-41.

[26] Eldred GE, Miller GV, Stark WS, Feeney-Burns L. Lipofuscin: resolution of discrepant fluorescence data. Science. 1982;216:757-9.

[27] Ramanujam N. Fluorescence spectroscopy of neoplastic and non-neoplastic tissues. Neoplasia (New York, NY). 2000;2:89-117.

[28] Sanjay Kala CP, Asha Agarwal, Asima Pradhan, Sudeep Thakur. Optical Spectroscopy: A Promising Diagnostic Tool for Breast Lesions. J Clin Diagn Res. 2011;5:1574-7.

[29] Joshi BP, Wang TD. Exogenous Molecular Probes for Targeted Imaging in Cancer: Focus on Multi-modal Imaging. Cancers. 2010;2:1251-87.

[30] Dan AG, Saha S, Monson KM, Wiese D, Schochet E, Barber KR, et al. 1% lymphazurin vs 10% fluorescein for sentinel node mapping in colorectal tumors. Archives of surgery. 2004;139:1180-4.

[31] Meyer A, Cheng C, Antonescu C, Pezzetta E, Bischof-Delaloye A, Ris HB. Successful migration of three tracers without identification of sentinel nodes during intraoperative lymphatic mapping for non-small cell lung cancer. Interactive cardiovascular and thoracic surgery. 2007;6:214-8.

[32] Sheng QS, Lang R, He Q, Yang YJ, Zhao DF, Chen DZ. Indocyanine green clearance test and model for end-stage liver disease score of patients with liver cirrhosis. Hepatobiliary & pancreatic diseases international : HBPD INT. 2009;8:46-9.

[33] Zipprich A, Kuss O, Rogowski S, Kleber G, Lotterer E, Seufferlein T, et al. Incorporating indocyanin green clearance into the Model for End Stage Liver Disease (MELD-ICG) improves prognostic accuracy in intermediate to advanced cirrhosis. Gut. 2010;59:963-8.

[34] Lane PM, Lam S, McWilliams A, Leriche JC, Anderson MW, Macaulay CE. Confocal fluorescence microendoscopy of bronchial epithelium. Journal of biomedical optics. 2009;14:024008.

[35] Albayrak Y, Oren D, Gundogdu C, Kurt A. Intraoperative sentinel lymph node mapping in patients with colon cancer: study of 38 cases. The Turkish journal of gastroenterology : the official journal of Turkish Society of Gastroenterology. 2011;22:286-92.

[36] Nour A. Efficacy of methylene blue dye in localization of sentinel lymph node in breast cancer patients. The breast journal. 2004;10:388-91.

[37] Varghese P, Abdel-Rahman AT, Akberali S, Mostafa A, Gattuso JM, Carpenter R. Methylene blue dye--a safe and effective alternative for sentinel lymph node localization. The breast journal. 2008;14:61-7.

[38] Lovell JF, Jin CS, Huynh E, Jin H, Kim C, Rubinstein JL, et al. Porphysome nanovesicles generated by porphyrin bilayers for use as multimodal biophotonic contrast agents. Nature materials. 2011;10:324-32.

[39] Jing Z, Ou S, Ban Y, Tong Z, Wang Y. Intraoperative assessment of anterior circulation aneurysms using the indocyanine green video angiography technique. Journal of clinical neuroscience : official journal of the Neurosurgical Society of Australasia. 2010;17:26-8.

[40] Imizu S, Kato Y, Sangli A, Oguri D, Sano H. Assessment of incomplete clipping of aneurysms intraoperatively by a near-infrared indocyanine green-video angiography (Niicg-Va) integrated microscope. Minimally invasive neurosurgery : MIN. 2008;51:199-203.

[41] Detter C, Russ D, Iffland A, Wipper S, Schurr MO, Reichenspurner H, et al. Near-infrared fluorescence coronary angiography: a new noninvasive technology for intraoperative graft patency control. The heart surgery forum. 2002;5:364-9.

[42] Balacumaraswami L, Taggart DP. Intraoperative imaging techniques to assess coronary artery bypass graft patency. The Annals of thoracic surgery. 2007;83:2251-7.

[43] Kang Y, Choi M, Lee J, Koh GY, Kwon K, Choi C. Quantitative analysis of peripheral tissue perfusion using spatiotemporal molecular dynamics. PloS one. 2009;4:e4275.

[44] Kim C, Song KH, Gao F, Wang LV. Sentinel Lymph Nodes and Lymphatic Vessels: Noninvasive Dual-Modality in Vivo Mapping by Using Indocyanine Green in Rats—Volumetric Spectroscopic Photoacoustic Imaging and Planar Fluorescence Imaging 1. Radiology. 2010;255:442-50.

[45] Tanaka E, Choi HS, Fujii H, Bawendi MG, Frangioni JV. Image-guided oncologic surgery using invisible light: completed pre-clinical development for sentinel lymph node mapping. Annals of surgical oncology. 2006;13:1671-81.

[46] Unno N, Inuzuka K, Suzuki M, Yamamoto N, Sagara D, Nishiyama M, et al. Preliminary experience with a novel fluorescence lymphography using indocyanine green in patients with secondary lymphedema. Journal of vascular surgery. 2007;45:1016-21.

[47] Jiao LR, El-Desoky AA, Seifalian AM, Habib N, Davidson BR. Effect of liver blood flow and function on hepatic indocyanine green clearance measured directly in a cirrhotic animal model. The British journal of surgery. 2000;87:568-74.

[48] El-Desoky A, Seifalian AM, Cope M, Delpy DT, Davidson BR. Experimental study of liver dysfunction evaluated by direct indocyanine green clearance using near infrared spectroscopy. The British journal of surgery. 1999;86:1005-11.

[49] Ishizawa T, Bandai Y, Ijichi M, Kaneko J, Hasegawa K, Kokudo N. Fluorescent cholangiography illuminating the biliary tree during laparoscopic cholecystectomy. The British journal of surgery. 2010;97:1369-77.

[50] Mothes H, Donicke T, Friedel R, Simon M, Markgraf E, Bach O. Indocyanine-green fluorescence video angiography used clinically to evaluate tissue perfusion in microsurgery. The Journal of trauma. 2004;57:1018-24.

[51] Habazettl H, Athanasopoulos D, Kuebler WM, Wagner H, Roussos C, Wagner PD, et al. Near-infrared spectroscopy and indocyanine green derived blood flow index for noninvasive measurement of muscle perfusion during exercise. Journal of applied physiology. 2010;108:962-7.

[52] Fischer T, Ebert B, Voigt J, Macdonald R, Schneider U, Thomas A, et al. Detection of rheumatoid arthritis using non-specific contrast enhanced fluorescence imaging. Academic radiology. 2010;17:375-81.

[53] Matsui A, Tanaka E, Choi HS, Kianzad V, Gioux S, Lomnes SJ, et al. Real-time, near-infrared, fluorescence-guided identification of the ureters using methylene blue. Surgery. 2010;148:78-86.

[54] Matsui A, Tanaka E, Choi HS, Winer JH, Kianzad V, Gioux S, et al. Real-time intra-operative near-infrared fluorescence identification of the extrahepatic bile ducts using clinically available contrast agents. Surgery. 2010;148:87-95.

[55] Tanaka E, Chen FY, Flaumenhaft R, Graham GJ, Laurence RG, Frangioni JV. Real-time assessment of cardiac perfusion, coronary angiography, and acute intravascular thrombi using dual-channel near-infrared fluorescence imaging. The Journal of thoracic and cardiovascular surgery. 2009;138:133-40.

[56] Winer JH, Choi HS, Gibbs-Strauss SL, Ashitate Y, Colson YL, Frangioni JV. Intraoperative localization of insulinoma and normal pancreas using invisible near-infrared fluorescent light. Annals of surgical oncology. 2010;17:1094-100.

[57] Velia P, Antonio B, Patrizia P, Carmen G, Anna M, Fernando M, et al. Fluorescein angiography and retinal vascular development in premature infants. The journal of maternal-fetal & neonatal medicine : the official journal of the European Association of Perinatal Medicine, the Federation of Asia and Oceania Perinatal Societies, the International Society of Perinatal Obstet. 2012;25 Suppl 3:53-6.

[58] Schutt F, Fischer J, Kopitz J, Holz FG. Indocyanine green angiography in the presence of subretinal or intraretinal haemorrhages: clinical and experimental investigations. Clin Experiment Ophthalmol. 2002;30:110-4.

[59] Herbort CP, LeHoang P, Guex-Crosier Y. Schematic interpretation of indocyanine green angiography in posterior uveitis using a standard angiographic protocol. Ophthalmology. 1998;105:432-40.

[60] Watanabe Y, Kumon K. Assessment by pulse dye-densitometry indocyanine green (ICG) clearance test of hepatic function of patients before cardiac surgery: its value as a predictor of serious postoperative liver dysfunction. J Cardiothorac Vasc Anesth. 1999;13:299-303.

[61] Janssen MW, Druckrey-Fiskaaen KT, Omidi L, Sliwinski G, Thiele C, Donaubauer B, et al. Indocyanine green R15 ratio depends directly on liver perfusion flow rate. J Hepatobiliary Pancreat Surg. 2009.

[62] Schad H, Brechtelsbauer H, Kramer K. Studies on the suitability of a cyanine dye (Viher-Test) for indicator dilution technique and its application to the measurement of pulmonary artery and aortic flow. Pflugers Arch. 1977;370:139-44.

[63] Troyan SL, Kianzad V, Gibbs-Strauss SL, Gioux S, Matsui A, Oketokoun R, et al. The FLARE intraoperative near-infrared fluorescence imaging system: a first-in-human clinical trial in breast cancer sentinel lymph node mapping. Annals of surgical oncology. 2009;16:2943-52.

[64] Alford R, Simpson HM, Duberman J, Hill GC, Ogawa M, Regino C, et al. Toxicity of organic fluorophores used in molecular imaging: literature review. Molecular imaging. 2009;8:341-54.

[65] Kirchherr AK, Briel A, Mader K. Stabilization of indocyanine green by encapsulation within micellar systems. Mol Pharm. 2009;6:480-91.

[66] Faybik P, Hetz H. Plasma disappearance rate of indocyanine green in liver dysfunction. Transplant Proc. 2006;38:801-2.

[67] Wu X, Liu H, Liu J, Haley KN, Treadway JA, Larson JP, et al. Immunofluorescent labeling of cancer marker Her2 and other cellular targets with semiconductor quantum dots. Nat Biotech. 2003;21:41-6.

[68] Saxena V, Sadoqi M, Shao J. Degradation kinetics of indocyanine green in aqueous solution. J Pharm Sci. 2003;92:2090-7.

[69] Sano K, Mitsunaga M, Nakajima T, Choyke PL, Kobayashi H. In vivo breast cancer characterization imaging using two monoclonal antibodies activatably labeled with near infrared fluorophores. Breast cancer research : BCR. 2012;14:R61.

[70] Folli S, Westermann P, Braichotte D, Pelegrin A, Wagnieres G, van den Bergh H, et al. Antibody-indocyanin conjugates for immunophotodetection of human squamous cell carcinoma in nude mice. Cancer Res. 1994;54:2643-9.

[71] Goldsmith SJ. Receptor imaging: competitive or complementary to antibody imaging? Seminars in nuclear medicine. 1997;27:85-93.

[72] Gong H, Kovar J, Little G, Chen H, Olive DM. In vivo imaging of xenograft tumors using an epidermal growth factor receptor-specific affibody molecule labeled with a near-infrared fluorophore. Neoplasia. 2010;12:139-49.

[73] Becker A, Hessenius C, Licha K, Ebert B, Sukowski U, Semmler W, et al. Receptor-targeted optical imaging of tumors with near-infrared fluorescent ligands. Nature biotechnology. 2001;19:327-31.

[74] Shi H, Tang Z, Kim Y, Nie H, Huang YF, He X, et al. In vivo fluorescence imaging of tumors using molecular aptamers generated by cell-SELEX. Chemistry, an Asian journal. 2010;5:2209-13.

[75] Berlier JE, Rothe A, Buller G, Bradford J, Gray DR, Filanoski BJ, et al. Quantitative comparison of long-wavelength Alexa Fluor dyes to Cy dyes: fluorescence of the dyes and their bioconjugates. The journal of histochemistry and cytochemistry : official journal of the Histochemistry Society. 2003;51:1699-712.

[76] Vira S, Mekhedov E, Humphrey G, Blank PS. Fluorescent-labeled antibodies: Balancing functionality and degree of labeling. Anal Biochem. 2010;402:146-50.

[77] Shrestha D, Bagosi A, Szollosi J, Jenei A. Comparative study of the three different fluorophore antibody conjugation strategies. Analytical and bioanalytical chemistry. 2012;404:1449-63.

[78] Nel AE, Madler L, Velegol D, Xia T, Hoek EM, Somasundaran P, et al. Understanding biophysicochemical interactions at the nano-bio interface. Nature materials. 2009;8:543-57.

[79] Albanese A, Tang PS, Chan WC. The effect of nanoparticle size, shape, and surface chemistry on biological systems. Annual review of biomedical engineering. 2012;14:1-16.

[80] Pelaz B, Charron G, Pfeiffer C, Zhao Y, de la Fuente JM, Liang XJ, et al. Interfacing Engineered Nanoparticles with Biological Systems: Anticipating Adverse Nano-Bio Interactions. Small. 2012.

[81] Li S-D, Huang L. Pharmacokinetics and Biodistribution of Nanoparticles. Mol Pharm. 2008;5:496-504.

[82] Alexis F, Pridgen E, Molnar LK, Farokhzad OC. Factors affecting the clearance and biodistribution of polymeric nanoparticles. Mol Pharm. 2008;5:505-15.

[83] Zhou C, Long M, Qin Y, Sun X, Zheng J. Luminescent gold nanoparticles with efficient renal clearance. Angewandte Chemie. 2011;50:3168-72.

[84] Choi HS, Liu W, Misra P, Tanaka E, Zimmer JP, Itty Ipe B, et al. Renal clearance of quantum dots. Nature biotechnology. 2007;25:1165-70.

[85] Burns AA, Vider J, Ow H, Herz E, Penate-Medina O, Baumgart M, et al. Fluorescent silica nanoparticles with efficient urinary excretion for nanomedicine. Nano Lett. 2009;9:442-8.

[86] Maeda H, Wu J, Sawa T, Matsumura Y, Hori K. Tumor vascular permeability and the EPR effect in macromolecular therapeutics: a review. Journal of controlled release : official journal of the Controlled Release Society. 2000;65:271-84.

[87] Moulton KS, Olsen BR, Sonn S, Fukai N, Zurakowski D, Zeng X. Loss of collagen XVIII enhances neovascularization and vascular permeability in atherosclerosis. Circulation. 2004;110:1330-6.

[88] Meding J, Urich M, Licha K, Reinhardt M, Misselwitz B, Fayad ZA, et al. Magnetic resonance imaging of atherosclerosis by targeting extracellular matrix deposition with Gadofluorine M. Contrast Media Mol Imaging. 2007;2:120-9.

[89] Levick JR. Permeability of rheumatoid and normal human synovium to specific plasma proteins. Arthritis Rheum. 1981;24:1550-60.

[90] Greish K. Enhanced permeability and retention effect for selective targeting of anticancer nanomedicine: are we there yet? Drug Discov Today: Technologies. 2012;9:e161-e6.

[91] Kamaly N, Xiao Z, Valencia PM, Radovic-Moreno AF, Farokhzad OC. Targeted polymeric therapeutic nanoparticles: design, development and clinical translation. Chem Soc Rev. 2012;41:2971-3010.

[92] Bae SW, Tan W, Hong JI. Fluorescent dye-doped silica nanoparticles: new tools for bioapplications. Chemical communications. 2012;48:2270-82.

[93] Jiang S, Gnanasammandhan MK, Zhang Y. Optical imaging-guided cancer therapy with fluorescent nanoparticles. Journal of the Royal Society, Interface / the Royal Society. 2010;7:3-18.

[94] Montalti M, Prodi L, Zaccheroni N, Battistini G, Marcuz S, Mancin F, et al. Size effect on the fluorescence properties of dansyl-doped silica nanoparticles. Langmuir. 2006;22:5877-81.

[95] Wang X, Xu S, Xu W. Luminescent properties of dye-PMMA composite nanospheres. Physical chemistry chemical physics : PCCP. 2011;13:1560-7.

[96] Lian W, Litherland SA, Badrane H, Tan W, Wu D, Baker HV, et al. Ultrasensitive detection of biomolecules with fluorescent dye-doped nanoparticles. Anal Biochem. 2004;334:135-44.

[97] Bringley JF, Penner TL, Wang R, Harder JF, Harrison WJ, Buonemani L. Silica nanoparticles encapsulating near-infrared emissive cyanine dyes. J Colloid Interface Sci. 2008;320:132-9.

[98] Saxena V, Sadoqi M, Shao J. Enhanced photo-stability, thermal-stability and aqueous-stability of indocyanine green in polymeric nanoparticulate systems. Journal of photochemistry and photobiology B, Biology. 2004;74:29-38.

[99] Yan J, Estévez MC, Smith JE, Wang K, He X, Wang L, et al. Dye-doped nanoparticles for bioanalysis. Nano Today. 2007;2:44-50.

[100] Wang L, Wang K, Santra S, Zhao X, Hilliard LR, Smith JE, et al. Watching Silica Nanoparticles Glow in the Biological World. Anal Chem. 2006;78:646-54.

[101] Rahman IA, Padavettan V. Synthesis of Silica Nanoparticles by Sol-Gel: Size-Dependent Properties, Surface Modification, and Applications in Silica-Polymer Nanocomposites—A Review. J Nanomater. 2012;2012:15.

[102] Sivakumar S, Diamente PR, Veggel FCJMv. Silica-Coated Ln3+-Doped LaF3 Nanoparticles as Robust Down- and Upconverting Biolabels. Chemistry. 2006;12:5878-84.

[103] Jain TK, Roy I, De TK, Maitra A. Nanometer Silica Particles Encapsulating Active Compounds: A Novel Ceramic Drug Carrier. J Am Chem Soc. 1998;120:11092-5.

[104] Tsagkogeorgas F, Ochsenkühn-Petropoulou M, Niessner R, Knopp D. Encapsulation of biomolecules for bioanalytical purposes: Preparation of diclofenac antibody-doped nanometer-sized silica particles by reverse micelle and sol-gel processing. Analytica Chimica Acta. 2006;573-574:133-7.

[105] An Y, Chen M, Xue Q, Liu W. Preparation and self-assembly of carboxylic acid-functionalized silica. J Colloid Interface Sci. 2007;311:507-13.

[106] Kumar R, Roy I, Ohulchanskyy TY, Goswami LN, Bonoiu AC, Bergey EJ, et al. Covalently dye-linked, surface-controlled, and bioconjugated organically modified silica nanoparticles as targeted probes for optical imaging. ACS Nano. 2008;2:449-56.

[107] He X, Nie H, Wang K, Tan W, Wu X, Zhang P. In vivo study of biodistribution and urinary excretion of surface-modified silica nanoparticles. Analytical chemistry. 2008;80:9597-603.

[108] Singh AK, Hahn MA, Gutwein LG, Rule MC, Knapik JA, Moudgil BM, et al. Multi-dye theranostic nanoparticle platform for bioimaging and cancer therapy. International journal of nanomedicine. 2012;7:2739-50.

[109] Santra S, Zhang P, Wang K, Tapec R, Tan W. Conjugation of Biomolecules with Luminophore-Doped Silica Nanoparticles for Photostable Biomarkers. Anal Chem. 2001;73:4988-93.

[110] Masuzaki R, Karp SJ, Omata M. New serum markers of hepatocellular carcinoma. Seminars in oncology. 2012;39:434-9.

[111] Deng T, Li JS, Jiang JH, Shen GL, Yu RQ. Preparation of Near-IR Fluorescent Nanoparticles for Fluorescence-Anisotropy-Based Immunoagglutination Assay in Whole Blood. Adv Funct Mater. 2006;16:2147-55.

[112] Fubini B, Hubbard A. Reactive oxygen species (ROS) and reactive nitrogen species (RNS) generation by silica in inflammation and fibrosis. Free Radic Biol Med. 2003;34:1507-16.

[113] Altinoglu EI, Adair JH. Near infrared imaging with nanoparticles. Wiley Interdiscip Rev Nanomed Nanobiotechnol.

[114] Pridgen EM, Langer R, Farokhzad OC. Biodegradable, polymeric nanoparticle delivery systems for cancer therapy. Nanomedicine (Lond). 2007;2:669-80.

[115] Lu JM, Wang X, Marin-Muller C, Wang H, Lin PH, Yao Q, et al. Current advances in research and clinical applications of PLGA-based nanotechnology. Expert Rev Mol Diagn. 2009;9:325-41.

[116] Wang X, Xu S, Liang C, Li H, Sun F, Xu W. Enriching PMMA nanospheres with adjustable charges as novel templates for multicolored dye@PMMA nanocomposites. Nanotechnology. 2011;22:275608.

[117] Tong R, Coyle VJ, Tang L, Barger AM, Fan TM, Cheng J. Polylactide nanoparticles containing stably incorporated cyanine dyes for in vitro and in vivo imaging applications. Microscopy research and technique. 2010;73:901-9.

[118] Wittmershaus BP, Skibicki JJ, McLafferty JB, Zhang Y-Z, Swan S. Spectral Properties of Single BODIPY Dyes in Polystyrene Microspheres and in Solutions. J Fluoresc. 2001;11:119-28.

[119] Zheng C, Zheng M, Gong P, Jia D, Zhang P, Shi B, et al. Indocyanine green-loaded biodegradable tumor targeting nanoprobes for in vitro and in vivo imaging. Biomaterials. 2012;33:5603-9.

[120] Ananth AN, Daniel SC, Sironmani TA, Umapathi S. PVA and BSA stabilized silver nanoparticles based surface-enhanced plasmon resonance probes for protein detection. Colloids and surfaces B, Biointerfaces. 2011;85:138-44.

[121] Choi JS, MacKay JA, Szoka FC, Jr. Low-pH-sensitive PEG-stabilized plasmid-lipid nanoparticles: preparation and characterization. Bioconjugate chemistry. 2003;14:420-9.

[122] He Y, Li Y, Hun X. Polymer nanoparticles as fluorescent labels in a fluoroimmunoassay for human chorionic gonadotropin. Microchimica Acta. 2010;171:393-8.

[123] Yang Z, Zheng S, Harrison WJ, Harder J, Wen X, Gelovani JG, et al. Long-Circulating Near-Infrared Fluorescence Core-Cross-Linked Polymeric Micelles: Synthesis, Characterization, and Dual Nuclear/Optical Imaging. Biomacromolecules. 2007;8:3422-8.

[124] Makarova OV, Ostafin AE, Miyoshi H, Norris JR, Meisel D. Adsorption and Encapsulation of Fluorescent Probes in Nanoparticles. J Phys Chem B. 1999;103:9080-4.

[125] Imhof A, Megens M, Engelberts JJ, de Lang DTN, Sprik R, Vos WL. Spectroscopy of Fluorescein (FITC) Dyed Colloidal Silica Spheres. J Phys Chem B. 1999;103:1408-15.

[126] Jain TK, Roy I, De TK, Maitra A. Nanometer Silica Particles Encapsulating Active Compounds: A Novel Ceramic Drug Carrier. J Am Chem Soc. 1998;120:11092-5.

[127] Ow H, Larson DR, Srivastava M, Baird BA, Webb WW, Wiesner U. Bright and stable core-shell fluorescent silica nanoparticles. Nano Lett. 2005;5:113-7.

[128] Zhao XJ, Bagwe RP, Tan WH. Development of organic-dye-doped silica nanoparticles in a reverse microemulsion. Adv Mater. 2004;16:173-+.

[129] Sokolov I, Kievsky YY, Kaszpurenko JM. Self-assembly of ultrabright fluorescent silica particles. Small. 2007;3:419-23.

[130] Jeon YH, Kim YH, Choi K, Piao JY, Quan B, Lee YS, et al. In vivo imaging of sentinel nodes using fluorescent silica nanoparticles in living mice. Molecular imaging and biology : MIB : the official publication of the Academy of Molecular Imaging. 2010;12:155-62.

[131] He X, Wu X, Wang K, Shi B, Hai L. Methylene blue-encapsulated phosphonate-terminated silica nanoparticles for simultaneous in vivo imaging and photodynamic therapy. Biomaterials. 2009;30:5601-9.

[132] Lee CH, Cheng SH, Wang YJ, Chen YC, Chen NT, Souris J, et al. Near-Infrared Mesoporous Silica Nanoparticles for Optical Imaging: Characterization and In Vivo Biodistribution. Adv Funct Mater. 2009;19:215-22.

[133] Kumar R, Roy I, Ohulchanskky TY, Vathy LA, Bergey EJ, Sajjad M, et al. In vivo biodistribution and clearance studies using multimodal organically modified silica nanoparticles. ACS Nano. 2010;4:699-708.

[134] Burns AA, Vider J, Ow H, Herz E, Penate-Medina O, Baumgart M, et al. Fluorescent Silica Nanoparticles with Efficient Urinary Excretion for Nanomedicine. Nano Lett. 2008;9:442-8.

[135] Rossi LM, Shi L, Rosenzweig N, Rosenzweig Z. Fluorescent silica nanospheres for digital counting bioassay of the breast cancer marker HER2/neu [correction of HER2/nue]. Biosensors & bioelectronics. 2006;21:1900-6.

[136] Josephson L, Kircher MF, Mahmood U, Tang Y, Weissleder R. Near-Infrared Fluorescent Nanoparticles as Combined MR/Optical Imaging Probes. Bioconjugate chemistry. 2002;13:554-60.

[137] Moore A, Medarova Z, Potthast A, Dai G. In Vivo Targeting of Underglycosylated MUC-1 Tumor Antigen Using a Multimodal Imaging Probe. Cancer Res. 2004;64:1821-7.

[138] Clark HA, Hoyer M, Philbert MA, Kopelman R. Optical Nanosensors for Chemical Analysis inside Single Living Cells. 1. Fabrication, Characterization, and Methods for Intracellular Delivery of PEBBLE Sensors. Anal Chem. 1999;71:4831-6.

[139] Sumner JP, Kopelman R. Alexa Fluor 488 as an iron sensing molecule and its application in PEBBLE nanosensors. The Analyst. 2005;130:528-33.

[140] Yu J, Yaseen MA, Anvari B, Wong MS. Synthesis of Near-Infrared-Absorbing Nanoparticle-Assembled Capsules. Chem Mater. 2007;19:1277-84.

[141] Rigler P, Meier W. Encapsulation of Fluorescent Molecules by Functionalized Polymeric Nanocontainers: Investigation by Confocal Fluorescence Imaging and Fluorescence Correlation Spectroscopy. J Am Chem Soc. 2005;128:367-73.

[142] Bosma G, Pathmamanoharan C, de Hoog EHA, Kegel WK, van Blaaderen A, Lekkerkerker HNW. Preparation of Monodisperse, Fluorescent PMMA–Latex Colloids by Dispersion Polymerization. J Colloid Interface Sci. 2002;245:292-300.

[143] Mok H, Jeong H, Kim S-J, Chung BH. Indocyanine green encapsulated nanogels for hyaluronidase activatable and selective near infrared imaging of tumors and lymph nodes. Chemical communications. 2012;48:8628-30.

[144] Morgan TT, Muddana HS, Altinoğlu EI, Rouse SM, Tabaković A, Tabouillot T, et al. Encapsulation of Organic Molecules in Calcium Phosphate Nanocomposite Particles for Intracellular Imaging and Drug Delivery. Nano Lett. 2008;8:4108-15.

[145] Muddana HS, Morgan TT, Adair JH, Butler PJ. Photophysics of Cy3-Encapsulated Calcium Phosphate Nanoparticles. Nano Lett. 2009;9:1559-66.

[146] Altinoglu EI, Russin TJ, Kaiser JM, Barth BM, Eklund PC, Kester M, et al. Near-infrared emitting fluorophore-doped calcium phosphate nanoparticles for in vivo imaging of human breast cancer. ACS Nano. 2008;2:2075-84.

[147] Barth BM, Sharma R, Altinoglu EI, Morgan TT, Shanmugavelandy SS, Kaiser JM, et al. Bioconjugation of calcium phosphosilicate composite nanoparticles for selective targeting of human breast and pancreatic cancers in vivo. ACS Nano. 2010;4:1279-87.

[148] Ghoroghchian PP, Frail PR, Susumu K, Blessington D, Brannan AK, Bates FS, et al. Near-infrared-emissive polymersomes: self-assembled soft matter for in vivo optical imaging. Proc Natl Acad Sci U S A. 2005;102:2922-7.

[149] Navarro FP, Berger M, Guillermet S, Josserand V, Guyon L, Neumann E, et al. Lipid nanoparticle vectorization of indocyanine green improves fluorescence imaging for tumor diagnosis and lymph node resection. Journal of biomedical nanotechnology. 2012;8:730-41.

[150] Texier I, Goutayer M, Da Silva A, Guyon L, Djaker N, Josserand V, et al. Cyanine-loaded lipid nanoparticles for improved in vivo fluorescence imaging. Journal of biomedical optics. 2009;14:054005.

[151] Kester M, Heakal Y, Fox T, Sharma A, Robertson GP, Morgan TT, et al. Calcium phosphate nanocomposite particles for in vitro imaging and encapsulated chemotherapeutic drug delivery to cancer cells. Nano Lett. 2008;8:4116-21.

[152] Morgan TT, Muddana HS, Altinoglu EI, Rouse SM, Tabakovic A, Tabouillot T, et al. Encapsulation of organic molecules in calcium phosphate nanocomposite particles for intracellular imaging and drug delivery. Nano Lett. 2008;8:4108-15.

[153] Dorozhkin SV, Epple M. Biological and Medical Significance of Calcium Phosphates. Angewandte Chemie. 2002;41:3130-46.

[154] Mooguee M, Omidi Y, Davaran S. Synthesis and in vitro release of adriamycin from star-shaped poly(lactide-co-glycolide) nano- and microparticles. J Pharm Sci. 2010;99:3389-97.

[155] Dechy-Cabaret O, Martin-Vaca B, Bourissou D. Controlled ring-opening polymerization of lactide and glycolide. Chemical reviews. 2004;104:6147-76.

[156] Zange R, Li Y, Kissel T. Biocompatibility testing of ABA triblock copolymers consisting of poly(L-lactic-co-glycolic acid) A blocks attached to a central poly(ethylene oxide) B block under in vitro conditions using different L929 mouse fibroblasts cell culture models. Journal of controlled release : official journal of the Controlled Release Society. 1998;56:249-58.

[157] Zhou S, Deng X, Li X, Jia W, Liu L. Synthesis and characterization of biodegradable low molecular weight aliphatic polyesters and their use in protein-delivery systems. J Appl Polym Sci. 2004;91:1848-56.

[158] Danhier F, Ansorena E, Silva JM, Coco R, Le Breton A, Preat V. PLGA-based nanoparticles: an overview of biomedical applications. Journal of controlled release : official journal of the Controlled Release Society. 2012;161:505-22.

[159] Acharya S, Sahoo SK. PLGA nanoparticles containing various anticancer agents and tumour delivery by EPR effect. Advanced drug delivery reviews. 2011;63:170-83.

[160] Dhar S, Kolishetti N, Lippard SJ, Farokhzad OC. Targeted delivery of a cisplatin prodrug for safer and more effective prostate cancer therapy in vivo. Proc Natl Acad Sci U S A. 2011;108:1850-5.

[161] Dhar S, Gu FX, Langer R, Farokhzad OC, Lippard SJ. Targeted delivery of cisplatin to prostate cancer cells by aptamer functionalized Pt(IV) prodrug-PLGA-PEG nanoparticles. Proc Natl Acad Sci U S A. 2008;105:17356-61.

[162] Jeong B, Bae YH, Kim SW. In situ gelation of PEG-PLGA-PEG triblock copolymer aqueous solutions and degradation thereof. Journal of biomedical materials research. 2000;50:171-7.

[163] Jokerst JV, Lobovkina T, Zare RN, Gambhir SS. Nanoparticle PEGylation for imaging and therapy. Nanomedicine (Lond). 2011;6:715-28.

[164] Cheng J, Teply BA, Sherifi I, Sung J, Luther G, Gu FX, et al. Formulation of functionalized PLGA-PEG nanoparticles for in vivo targeted drug delivery. Biomaterials. 2007;28:869-76.

[165] Betancourt T, Brown B, Brannon-Peppas L. Doxorubicin-loaded PLGA nanoparticles by nanoprecipitation: preparation, characterization and in vitro evaluation. Nanomedicine (Lond). 2007;2:219-32.

[166] Farokhzad OC, Cheng J, Teply BA, Sherifi I, Jon S, Kantoff PW, et al. Targeted nanoparticle-aptamer bioconjugates for cancer chemotherapy in vivo. Proc Natl Acad Sci U S A. 2006;103:6315-20.

[167] Marrache S, Dhar S. Engineering of blended nanoparticle platform for delivery of mitochondria-acting therapeutics. Proc Natl Acad Sci U S A 2012.

[168] Kolishetti N, Dhar S, Valencia PM, Lin LQ, Karnik R, Lippard SJ, et al. Engineering of self-assembled nanoparticle platform for precisely controlled combination drug therapy. Proc Natl Acad Sci U S A 2010;107:17939-44.

[169] McCarron PA, Marouf WM, Quinn DJ, Fay F, Burden RE, Olwill SA, et al. Antibody Targeting of Camptothecin-Loaded PLGA Nanoparticles to Tumor Cells. Bioconjugate chemistry. 2008;19:1561-9.

[170] Sengupta S, Eavarone D, Capila I, Zhao G, Watson N, Kiziltepe T, et al. Temporal targeting of tumour cells and neovasculature with a nanoscale delivery system. Nature. 2005;436:568-72.

[171] Sanna V, Pintus G, Roggio AM, Punzoni S, Posadino AM, Arca A, et al. Targeted Biocompatible Nanoparticles for the Delivery of (−)-Epigallocatechin 3-Gallate to Prostate Cancer Cells. J Med Chem. 2011;54:1321-32.

[172] Tosi G, Fano RA, Bondioli L, Badiali L, Benassi R, Rivasi F, et al. Investigation on mechanisms of glycopeptide nanoparticles for drug delivery across the blood-brain barrier. Nanomedicine (Lond). 2011;6:423-36.

[173] Zhang N, Chittasupho C, Duangrat C, Siahaan TJ, Berkland C. PLGA Nanoparticle−Peptide Conjugate Effectively Targets Intercellular Cell-Adhesion Molecule-1. Bioconjugate chemistry. 2007;19:145-52.

[174] Mieszawska AJ, Gianella A, Cormode DP, Zhao Y, Meijerink A, Langer R, et al. Engineering of lipid-coated PLGA nanoparticles with a tunable payload of diagnostically active nanocrystals for medical imaging. Chemical communications. 2012;48:5835-7.

[175] Jia Y, Yuan M, Yuan H, Huang X, Sui X, Cui X, et al. Co-encapsulation of magnetic Fe3O4 nanoparticles and doxorubicin into biodegradable PLGA nanocarriers for intratumoral drug delivery. International journal of nanomedicine. 2012;7:1697-708.

[176] Yang J, Lee C-H, Park J, Seo S, Lim E-K, Song YJ, et al. Antibody conjugated magnetic PLGA nanoparticles for diagnosis and treatment of breast cancer. J Mater Chem. 2007;17:2695-9.

[177] Qiao M, Chen D, Ma X, Liu Y. Injectable biodegradable temperature-responsive PLGA-PEG-PLGA copolymers: synthesis and effect of copolymer composition on the drug release from the copolymer-based hydrogels. International journal of pharmaceutics. 2005;294:103-12.

[178] Vauthier C, Bouchemal K. Methods for the preparation and manufacture of polymeric nanoparticles. Pharm Res. 2009;26:1025-58.

[179] Cohen-Sela E, Teitlboim S, Chorny M, Koroukhov N, Danenberg HD, Gao J, et al. Single and double emulsion manufacturing techniques of an amphiphilic drug in PLGA nanoparticles: formulations of mithramycin and bioactivity. J Pharm Sci. 2009;98:1452-62.

[180] Karnik R, Gu F, Basto P, Cannizzaro C, Dean L, Kyei-Manu W, et al. Microfluidic platform for controlled synthesis of polymeric nanoparticles. Nano letters. 2008;8:2906-12.

[181] Valencia PM, Farokhzad OC, Karnik R, Langer R. Microfluidic technologies for accelerating the clinical translation of nanoparticles. Nat Nanotechnol. 2012;7:623-9.

[182] Lee S, Ryu JH, Park K, Lee A, Lee SY, Youn IC, et al. Polymeric nanoparticle-based activatable near-infrared nanosensor for protease determination in vivo. Nano Lett. 2009;9:4412-6.

[183] He X, Wang Y, Wang K, Chen M, Chen S. Fluorescence resonance energy transfer mediated large stokes shifting near-infrared fluorescent silica nanoparticles for in vivo small-animal imaging. Analytical chemistry. 2012;84:9056-64.

[184] Kelleher MT, Fruhwirth G, Patel G, Ofo E, Festy F, Barber PR, et al. The potential of optical proteomic technologies to individualize prognosis and guide rational treatment for cancer patients. Targeted oncology. 2009;4:235-52.

[185] Romoser VA, Hinkle PM, Persechini A. Detection in living cells of Ca2+-dependent changes in the fluorescence emission of an indicator composed of two green fluorescent protein variants linked by a calmodulin-binding sequence. A new class of fluorescent indicators. J Biol Chem. 1997;272:13270-4.

[186] Miyawaki A, Griesbeck O, Heim R, Tsien RY. Dynamic and quantitative Ca2+ measurements using improved cameleons. Proc Natl Acad Sci U S A. 1999;96:2135-40.

[187] Xu X, Gerard AL, Huang BC, Anderson DC, Payan DG, Luo Y. Detection of programmed cell death using fluorescence energy transfer. Nucleic Acids Res. 1998;26:2034-5.

[188] Luo KQ, Yu VC, Pu Y, Chang DC. Application of the fluorescence resonance energy transfer method for studying the dynamics of caspase-3 activation during UV-induced apoptosis in living HeLa cells. Biochem Biophys Res Commun. 2001;283:1054-60.

[189] Russell RJ, Pishko MV, Gefrides CC, McShane MJ, Cote GL. A fluorescence-based glucose biosensor using concanavalin A and dextran encapsulated in a poly(ethylene glycol) hydrogel. Anal Chem. 1999;71:3126-32.

[190] Godwin HA, Berg JM. A Fluorescent Zinc Probe Based on Metal-Induced Peptide Folding. J Am Chem Soc. 1996;118:6514-5.

[191] Ueda H, Kubota K, Wang Y, Tsumoto K, Mahoney W, Kumagai I, et al. Homogeneous noncompetitive immunoassay based on the energy transfer between fluorolabeled antibody variable domains (open sandwich fluoroimmunoassay). Biotechniques. 1999;27:738-42.

[192] Song X, Shi J, Nolan J, Swanson B. Detection of multivalent interactions through two-tiered energy transfer. Anal Biochem. 2001;291:133-41.

[193] Lu S, Wang Y. Fluorescence resonance energy transfer biosensors for cancer detection and evaluation of drug efficacy. Clin Cancer Res. 2010;16:3822-4.

[194] Shiraishi Y, Miyamoto R, Zhang X, Hirai T. Rhodamine-based fluorescent thermometer exhibiting selective emission enhancement at a specific temperature range. Organic letters. 2007;9:3921-4.

[195] Medintz IL, Clapp AR, Mattoussi H, Goldman ER, Fisher B, Mauro JM. Self-assembled nanoscale biosensors based on quantum dot FRET donors. Nature materials. 2003;2:630-8.

[196] Bagalkot V, Zhang L, Levy-Nissenbaum E, Jon S, Kantoff PW, Langer R, et al. Quantum Dot−Aptamer Conjugates for Synchronous Cancer Imaging, Therapy, and Sensing of Drug Delivery Based on Bi-Fluorescence Resonance Energy Transfer. Nano Lett. 2007;7:3065-70.

[197] Law B, Tung CH. Proteolysis: a biological process adapted in drug delivery, therapy, and imaging. Bioconjugate chemistry. 2009;20:1683-95.

[198] Lee S, Park K, Lee SY, Ryu JH, Park JW, Ahn HJ, et al. Dark quenched matrix metalloproteinase fluorogenic probe for imaging osteoarthritis development in vivo. Bioconjugate chemistry. 2008;19:1743-7.

[199] Kim S, Lim YT, Soltesz EG, De Grand AM, Lee J, Nakayama A, et al. Near-infrared fluorescent type II quantum dots for sentinel lymph node mapping. Nat Biotechnol. 2004;22:93-7.

[200] Rzigalinski BA, Strobl JS. Cadmium-containing nanoparticles: perspectives on pharmacology and toxicology of quantum dots. Toxicol Appl Pharmacol. 2009;238:280-8.

[201] Fan J, Hu M, Zhan P, Peng X. Energy transfer cassettes based on organic fluorophores: construction and applications in ratiometric sensing. Chem Soc Rev. 2013.

[202] Ueno Y, Jose J, Loudet A, Perez-Bolivar C, Anzenbacher P, Jr., Burgess K. Encapsulated energy-transfer cassettes with extremely well resolved fluorescent outputs. Journal of the American Chemical Society. 2011;133:51-5.

[203] Jose J, Loudet A, Ueno Y, Wu L, Chen HY, Son DH, et al. Energy transfer cassettes in silica nanoparticles target intracellular organelles. Organic & biomolecular chemistry. 2011;9:3871-7.

[204] Wang L, Yang C, Tan W. Dual-luminophore-doped silica nanoparticles for multiplexed signaling. Nano Lett. 2005;5:37-43.

[205] Wang L, Tan W. Multicolor FRET silica nanoparticles by single wavelength excitation. Nano Lett. 2006;6:84-8.

[206] Chen J, Cheng Y. Far-field superresolution imaging with dual-dye-doped nanoparticles. Optics letters. 2009;34:1831-3.

[207] Fein M, Unkeless J, Chuang FY, Sassaroli M, da Costa R, Vaananen H, et al. Lateral mobility of lipid analogues and GPI-anchored proteins in supported bilayers determined by fluorescent bead tracking. The Journal of membrane biology. 1993;135:83-92.

[208] Persson HG, Gatzinsky KP. Distribution of retrogradely transported fluorescent latex microspheres in rat lumbosacral ventral root axons following peripheral crush injury: a light and electron microscopic study. Brain Research. 1993;630:115-24.

[209] Fredrickson AG, Hatzis C, Srienc F. A statistical analysis of flow cytometric determinations of phagocytosis rates. Cytometry. 1992;13:423-31.

[210] Wu W-B, Wang M-L, Sun Y-M, Huang W, Cui Y-P, Xu C-X. Fluorescent polystyrene microspheres with large Stokes shift by fluorescence resonance energy transfer. J Phys Chem Solids. 2008;69:76-82.

[211] Zong C, Wu J, Wang C, Ju H, Yan F. Chemiluminescence imaging immunoassay of multiple tumor markers for cancer screening. Anal Chem. 2012;84:2410-5.

[212] Chen AA, Underhill GH, Bhatia SN. Multiplexed, high-throughput analysis of 3D microtissue suspensions. Integrative biology : quantitative biosciences from nano to macro. 2010;2:517-27.

[213] Wang L, Zhao W, O'Donoghue MB, Tan W. Fluorescent nanoparticles for multiplexed bacteria monitoring. Bioconjugate chemistry. 2007;18:297-301.

[214] Chen X, Estevez MC, Zhu Z, Huang YF, Chen Y, Wang L, et al. Using aptamer-conjugated fluorescence resonance energy transfer nanoparticles for multiplexed cancer cell monitoring. Anal Chem. 2009;81:7009-14.

[215] Kurner JM, Klimant I, Krause C, Pringsheim E, Wolfbeis OS. A new type of phosphorescent nanospheres for use in advanced time-resolved multiplexed bioassays. Anal Biochem. 2001;297:32-41.

[216] Ntziachristos V, Bremer C, Weissleder R. Fluorescence imaging with near-infrared light: new technological advances that enable in vivo molecular imaging. European radiology. 2003;13:195-208.

[217] Peng X, Song F, Lu E, Wang Y, Zhou W, Fan J, et al. Heptamethine cyanine dyes with a large stokes shift and strong fluorescence: a paradigm for excited-state intramolecular charge transfer. Journal of the American Chemical Society. 2005;127:4170-1.

[218] Bertolino CA, Caputo G, Barolo C, Viscardi G, Coluccia S. Novel heptamethine cyanine dyes with large Stoke's shift for biological applications in the near infrared. J Fluoresc. 2006;16:221-5.

[219] Altinoglu EI, Adair JH. Near infrared imaging with nanoparticles. Wiley Interdiscip Rev Nanomed Nanobiotechnol. 2010;2:461-77.

[220] He X, Wang K, Cheng Z. In vivo near-infrared fluorescence imaging of cancer with nanoparticle-based probes. Wiley Interdiscip Rev Nanomed Nanobiotechnol. 2010;2:349-66.

[221] Koo H, Huh MS, Ryu JH, Lee D-E, Sun I-C, Choi K, et al. Nanoprobes for biomedical imaging in living systems. Nano Today. 2011;6:204-20.

[222] Day RN, Periasamy A, Schaufele F. Fluorescence resonance energy transfer microscopy of localized protein interactions in the living cell nucleus. Methods. 2001;25:4-18.

[223] Zhang S, Metelev V, Tabatadze D, Zamecnik PC, Bogdanov A, Jr. Fluorescence resonance energy transfer in near-infrared fluorescent oligonucleotide probes for detecting protein-DNA interactions. Proc Natl Acad Sci U S A. 2008;105:4156-61.

[224] Lakowicz JR. Principle of fluorescence spectroscopy. second edition ed. New york: Kluwer Academic/Plenum publishers; 1999.

[225] Chen H, Kim S, He W, Wang H, Low PS, Park K, et al. Fast release of lipophilic agents from circulating PEG-PDLLA micelles revealed by in vivo forster resonance energy transfer imaging. Langmuir. 2008;24:5213-7.

[226] Lu J, Owen SC, Shoichet MS. Stability of Self-Assembled Polymeric Micelles in Serum. Macromolecules. 2011;44:6002-8.

[227] Chen H, Kim S, Li L, Wang S, Park K, Cheng JX. Release of hydrophobic molecules from polymer micelles into cell membranes revealed by Forster resonance energy transfer imaging. Proceedings of the National Academy of Sciences of the United States of America. 2008;105:6596-601.

[228] Gref R, Minamitake Y, Peracchia MT, Trubetskoy V, Torchilin V, Langer R. Biodegradable long-circulating polymeric nanospheres. Science. 1994;263:1600-3.

[229] Townsend SA, Evrony GD, Gu FX, Schulz MP, Brown RH, Jr., Langer R. Tetanus toxin C fragment-conjugated nanoparticles for targeted drug delivery to neurons. Biomaterials. 2007;28:5176-84.

[230] Fessi H, Puisieux F, Devissaguet JP, Ammoury N, Benita S. Nanocapsule formation by interfacial polymer deposition following solvent displacement. International journal of pharmaceutics. 1989;55:R1-R4.

[231] Panyam J, Sahoo SK, Prabha S, Bargar T, Labhasetwar V. Fluorescence and electron microscopy probes for cellular and tissue uptake of poly(D,L-lactide-co-glycolide) nanoparticles. International journal of pharmaceutics. 2003;262:1-11.

[232] Vauthier C, Schmidt C, Couvreur P. Measurement of the Density of Polymeric Nanoparticulate Drug Carriers by Isopycnic Centrifugation. J Nanopart Res. 1999;1:411-8.

[233] Chen Y, Wang F, Benson HA. Effect of formulation factors on incorporation of the hydrophilic peptide dalargin into PLGA and mPEG-PLGA nanoparticles. Biopolymers. 2008;90:644-50.

[234] Mujumdar RB, Ernst LA, Mujumdar SR, Lewis CJ, Waggoner AS. Cyanine dye labeling reagents: sulfoindocyanine succinimidyl esters. Bioconjugate chemistry. 1993;4:105-11.

[235] Yu WW, Qu L, Guo W, Peng X. Experimental Determination of the Extinction Coefficient of CdTe, CdSe, and CdS Nanocrystals. Chem Mater. 2003;15:2854-60.

[236] Russin TJ, Altinoglu EI, Adair JH, Eklund PC. Measuring the fluorescent quantum efficiency of indocyanine green encapsulated in nanocomposite particulates. J Phys Condens Matter. 2010;22:334217.

[237] Herz E, Marchincin T, Connelly L, Bonner D, Burns A, Switalski S, et al. Relative quantum yield measurements of coumarin encapsulated in core-shell silica nanoparticles. J Fluoresc.20:67-72.

[238] Xia Z, Liu Y. Reliable and global measurement of fluorescence resonance energy transfer using fluorescence microscopes. Biophysical journal. 2001;81:2395-402.

[239] Kaufmann AM, Goldman SD, Krise JP. A fluorescence resonance energy transfer-based approach for investigating late endosome-lysosome retrograde fusion events. Anal Biochem. 2009;386:91-7.

[240] Feinstein TN, Wehbi VL, Ardura JA, Wheeler DS, Ferrandon S, Gardella TJ, et al. Retromer terminates the generation of cAMP by internalized PTH receptors. Nat Chem Biol. 2011;7:278-84.

[241] Grunberg R, Ferrar TS, van der Sloot AM, Constante M, Serrano L. Building blocks for protein interaction devices. Nucleic Acids Res.38:2645-62.

[242] Teo YN, Kool ET. Polyfluorophore excimers and exciplexes as FRET donors in DNA. Bioconjugate chemistry. 2009;20:2371-80.

[243] Law B, Weissleder R, Tung CH. Protease-sensitive fluorescent nanofibers. Bioconjugate chemistry. 2007;18:1701-4.

[244] Ji S, Zhu Z, Hoye TR, Macosko CW. Maleimide Functionalized Poly(ε-caprolactone)-block-poly(ethylene glycol) (PCL-PEG-MAL): Synthesis, Nanoparticle Formation, and Thiol Conjugation. Macromol Chem Phys. 2009;210:823-31.

[245] Law B, Quinti L, Choi Y, Weissleder R, Tung CH. A mitochondrial targeted fusion peptide exhibits remarkable cytotoxicity. Mol Cancer Ther. 2006;5:1944-9.

[246] Dobrovolskaia MA, Clogston JD, Neun BW, Hall JB, Patri AK, McNeil SE. Method for analysis of nanoparticle hemolytic properties in vitro. Nano Lett. 2008;8:2180-7.

[247] Fang RH, Aryal S, Hu CM, Zhang L. Quick synthesis of lipid-polymer hybrid nanoparticles with low polydispersity using a single-step sonication method. Langmuir. 2010;26:16958-62.

[248] Feige JN, Sage D, Wahli W, Desvergne B, Gelman L. PixFRET, an ImageJ plug-in for FRET calculation that can accommodate variations in spectral bleed-throughs. Microsc Res Tech. 2005;68:51-8.

[249] Toti US, Guru BR, Grill AE, Panyam J. Interfacial activity assisted surface functionalization: a novel approach to incorporate maleimide functional groups and cRGD peptide on polymeric nanoparticles for targeted drug delivery. Mol Pharm. 2010;7:1108-17.

[250] Bilati U, Allemann E, Doelker E. Nanoprecipitation versus emulsion-based techniques for the encapsulation of proteins into biodegradable nanoparticles and process-related stability issues. AAPS PharmSciTech. 2005;6:E594-604.

[251] Galindo-Rodriguez S, Allemann E, Fessi H, Doelker E. Physicochemical parameters associated with nanoparticle formation in the salting-out, emulsification-diffusion, and nanoprecipitation methods. Pharm Res. 2004;21:1428-39.

[252] Garcia-Saez AJ, Chiantia S, Schwille P. Effect of line tension on the lateral organization of lipid membranes. J Biol Chem. 2007;282:33537-44.

[253] Han J, Goldstein LA, Gastman BR, Rabinowich H. Interrelated roles for Mcl-1 and BIM in regulation of TRAIL-mediated mitochondrial apoptosis. J Biol Chem. 2006;281:10153-63.

[254] Law B, Curino A, Bugge TH, Weissleder R, Tung CH. Design, synthesis, and characterization of urokinase plasminogen-activator-sensitive near-infrared reporter. Chem Biol. 2004;11:99-106.

[255] Lin Y, Weissleder R, Tung CH. Novel near-infrared cyanine fluorochromes: synthesis, properties, and bioconjugation. Bioconjugate chemistry. 2002;13:605-10.

[256] Schadlich A, Rose C, Kuntsche J, Caysa H, Mueller T, Gopferich A, et al. How stealthy are PEG-PLA nanoparticles? An NIR in vivo study combined with detailed size measurements. Pharm Res. 2011;28:1995-2007.

[257] Gu F, Zhang L, Teply BA, Mann N, Wang A, Radovic-Moreno AF, et al. Precise engineering of targeted nanoparticles by using self-assembled biointegrated block copolymers. Proc Natl Acad Sci U S A. 2008;105:2586-91.

[258] Akers W, Lesage F, Holten D, Achilefu S. In vivo resolution of multiexponential decays of multiple near-infrared molecular probes by fluorescence lifetime-gated whole-body time-resolved diffuse optical imaging. Mol Imaging. 2007;6:237-46.

[259] Cubeddu R, Pifferi A, Taroni P, Torricelli A, Valentini G. A solid tissue phantom for photon migration studies. Phys Med Biol. 1997;42:1971-9.

[260] Bouzigues C, Gacoin T, Alexandrou A. Biological applications of rare-earth based nanoparticles. ACS Nano. 2011;5:8488-505.

[261] Wu X, He X, Wang K, Xie C, Zhou B, Qing Z. Ultrasmall near-infrared gold nanoclusters for tumor fluorescence imaging in vivo. Nanoscale. 2010;2:2244-9.

[262] Hsiao JK, Law B, Weissleder R, Tung CH. In-vivo imaging of tumor associated urokinase-type plasminogen activator activity. Journal of biomedical optics. 2006;11:34013.

[263] Shcherbo D, Merzlyak EM, Chepurnykh TV, Fradkov AF, Ermakova GV, Solovieva EA, et al. Bright far-red fluorescent protein for whole-body imaging. Nat Methods. 2007;4:741-6.

[264] Han M, Gao X, Su JZ, Nie S. Quantum-dot-tagged microbeads for multiplexed optical coding of biomolecules. Nat Biotechnol. 2001;19:631-5.

[265] Hu M, Yan J, He Y, Lu H, Weng L, Song S, et al. Ultrasensitive, multiplexed detection of cancer biomarkers directly in serum by using a quantum dot-based microfluidic protein chip. ACS Nano. 2010;4:488-94.

[266] Cheng L, Yang K, Zhang S, Shao M, Lee S, Liu Z. Highly-sensitive multiplexed in vivo imaging using PEGylated upconversion nanoparticles. Nano Research. 2010;3:722-32.

[267] Gao X, Cui Y, Levenson RM, Chung LW, Nie S. In vivo cancer targeting and imaging with semiconductor quantum dots. Nat Biotechnol. 2004;22:969-76.

[268] Zhang Q, Atay T, Tischler JR, Bradley MS, Bulovic V, Nurmikko AV. Highly efficient resonant coupling of optical excitations in hybrid organic/inorganic semiconductor nanostructures. Nat Nanotechnol. 2007;2:555-9.

[269] Kang WJ, Chae JR, Cho YL, Lee JD, Kim S. Multiplex imaging of single tumor cells using quantum-dot-conjugated aptamers. Small. 2009;5:2519-22.

[270] Delehanty JB, Bradburne CE, Susumu K, Boeneman K, Mei BC, Farrell D, et al. Spatiotemporal multicolor labeling of individual cells using peptide-functionalized quantum dots and mixed delivery techniques. J Am Chem Soc. 2011;133:10482-9.

[271] Kosaka N, Ogawa M, Sato N, Choyke PL, Kobayashi H. In vivo real-time, multicolor, quantum dot lymphatic imaging. The Journal of investigative dermatology. 2009;129:2818-22.

[272] Lin S, Xie X, Patel MR, Yang YH, Li Z, Cao F, et al. Quantum dot imaging for embryonic stem cells. BMC biotechnology. 2007;7:67.

[273] Chen N, He Y, Su Y, Li X, Huang Q, Wang H, et al. The cytotoxicity of cadmium-based quantum dots. Biomaterials. 2012;33:1238-44.

[274] Lee SF, Osborne MA. Brightening, blinking, bluing and bleaching in the life of a quantum dot: friend or foe? Chemphyschem : a European journal of chemical physics and physical chemistry. 2009;10:2174-91.

[275] Zhang J, Wang L, Zhang H, Boey F, Song S, Fan C. Aptamer-based multicolor fluorescent gold nanoprobes for multiplex detection in homogeneous solution. Small. 2010;6:201-4.

[276] Lacoste TD, Michalet X, Pinaud F, Chemla DS, Alivisatos AP, Weiss S. Ultrahigh-resolution multicolor colocalization of single fluorescent probes. Proc Natl Acad Sci U S A. 2000;97:9461-6.

[277] Jin Y, Ye F, Zeigler M, Wu C, Chiu DT. Near-infrared fluorescent dye-doped semiconducting polymer dots. ACS Nano. 2011;5:1468-75.

[278] Wagh A, Qian SY, Law B. Development of Biocompatible Polymeric Nanoparticles for in Vivo NIR and FRET Imaging. Bioconjugate chemistry. 2012;23:981-92.

[279] Alexis F, Basto P, Levy-Nissenbaum E, Radovic-Moreno AF, Zhang L, Pridgen E, et al. HER-2-targeted nanoparticle-affibody bioconjugates for cancer therapy. ChemMedChem. 2008;3:1839-43.

[280] Graf N, Bielenberg DR, Kolishetti N, Muus C, Banyard J, Farokhzad OC, et al. alpha(V)beta(3) Integrin-Targeted PLGA-PEG Nanoparticles for Enhanced Anti-tumor Efficacy of a Pt(IV) Prodrug. ACS Nano. 2012;6:4530-9.

[281] Erickson HP. Size and shape of protein molecules at the nanometer level determined by sedimentation, gel filtration, and electron microscopy. Biological procedures online. 2009;11:32-51.

[282] Law B, Weissleder R, Tung CH. Peptide-based biomaterials for protease-enhanced drug delivery. Biomacromolecules. 2006;7:1261-5.

[283] Liu Y, Li K, Liu B, Feng SS. A strategy for precision engineering of nanoparticles of biodegradable copolymers for quantitative control of targeted drug delivery. Biomaterials. 2010;31:9145-55.

[284] Subhash HM, Xie H, Smith JW, McCarty OJ. Optical detection of indocyanine green encapsulated biocompatible poly (lactic-co-glycolic) acid nanoparticles with photothermal optical coherence tomography. Optics letters. 2012;37:981-3.

[285] Bouteiller C, Clavé G, Bernardin A, Chipon B, Massonneau M, Renard P-Y, et al. Novel Water-Soluble Near-Infrared Cyanine Dyes: Synthesis, Spectral Properties, and Use in the Preparation of Internally Quenched Fluorescent Probes. Bioconjugate chemistry. 2007;18:1303-17.

[286] Saini S, Srinivas G, Bagchi B. Distance and orientation dependence of excitation energy transfer: from molecular systems to metal nanoparticles. J Phys Chem B. 2009;113:1817-32.

[287] Misra R, Sahoo SK. Intracellular trafficking of nuclear localization signal conjugated nanoparticles for cancer therapy. Eur J Pharm Sci. 2010;39:152-63.

[288] Zhu L, Wu W, Zhu M-Q, Han JJ, Hurst JK, Li ADQ. Reversibly Photoswitchable Dual-Color Fluorescent Nanoparticles as New Tools for Live-Cell Imaging. J Am Chem Soc. 2007;129:3524-6.

[289] Chen J, Zhang P, Fang G, Yi P, Zeng F, Wu S. Design and Synthesis of FRET-Mediated Multicolor and Photoswitchable Fluorescent Polymer Nanoparticles with Tunable Emission Properties. J Phys Chem B. 2012;116:4354-62.

[290] Rampazzo E, Boschi F, Bonacchi S, Juris R, Montalti M, Zaccheroni N, et al. Multicolor core/shell silica nanoparticles for in vivo and ex vivo imaging. Nanoscale. 2012;4:824-30.

[291] Yukawa H, Kagami Y, Watanabe M, Oishi K, Miyamoto Y, Okamoto Y, et al. Quantum dots labeling using octa-arginine peptides for imaging of adipose tissue-derived stem cells. Biomaterials. 2010;31:4094-103.

[292] Ostendorp T, Leclerc E, Galichet A, Koch M, Demling N, Weigle B, et al. Structural and functional insights into RAGE activation by multimeric S100B. The EMBO journal. 2007;26:3868-78.

[293] Corsi F, Fiandra L, De Palma C, Colombo M, Mazzucchelli S, Verderio P, et al. HER2 expression in breast cancer cells is downregulated upon active targeting by antibody-engineered multifunctional nanoparticles in mice. ACS Nano. 2011;5:6383-93.

[294] Leclerc E, Heizmann CW, Vetter SW. RAGE and S100 protein transcription levels are highly variable in human melanoma tumors and cells. General physiology and biophysics. 2009;28 Spec No Focus:F65-75.

[295] Jiang W, KimBetty YS, Rutka JT, ChanWarren CW. Nanoparticle-mediated cellular response is size-dependent. Nat Nanotechnol. 2008;3:145-50.

[296] Liu BR, Huang YW, Winiarz JG, Chiang HJ, Lee HJ. Intracellular delivery of quantum dots mediated by a histidine- and arginine-rich HR9 cell-penetrating peptide through the direct membrane translocation mechanism. Biomaterials. 2011;32:3520-37.

[297] Liu BR, Li JF, Lu SW, Leel HJ, Huang YW, Shannon KB, et al. Cellular internalization of quantum dots noncovalently conjugated with arginine-rich cell-penetrating peptides. J Nanosci Nanotechnol. 2010;10:6534-43.

[298] Silva H, Frezard F, Peterson EJ, Kabolizadeh P, Ryan JJ, Farrell NP. Heparan sulfate proteoglycan-mediated entry pathway for charged tri-platinum compounds: differential cellular accumulation mechanisms for platinum. Mol Pharm. 2012;9:1795-802.

[299] Koshkaryev A, Piroyan A, Torchilin VP. Bleomycin in octaarginine-modified fusogenic liposomes results in improved tumor growth inhibition. Cancer Lett. 2012.

[300] Liu J, Lau SK, Varma VA, Kairdolf BA, Nie S. Multiplexed detection and characterization of rare tumor cells in Hodgkin's lymphoma with multicolor quantum dots. Anal Chem. 2010;82:6237-43.

[301] Liu J, Lau SK, Varma VA, Moffitt RA, Caldwell M, Liu T, et al. Molecular mapping of tumor heterogeneity on clinical tissue specimens with multiplexed quantum dots. ACS Nano. 2010;4:2755-65.

[302] Yezhelyev MV, Al-Hajj A, Morris C, Marcus AI, Liu T, Lewis M, et al. In situ molecular profiling of breast cancer biomarkers with multicolor quantum dots. Adv Mater. 2007;19:3146-+.

[303] Xu J, Liang J, Li J, Yang W. Multicolor dye-doped silica nanoparticles independent of FRET. Langmuir. 2010;26:15722-5.

[304] Lu D, Lei J, Wang L, Zhang J. Multifluorescently traceable nanoparticle by a single-wavelength excitation with color-related drug release performance. J Am Chem Soc. 2012;134:8746-9.

[305] Wu C, Bull B, Szymanski C, Christensen K, McNeill J. Multicolor conjugated polymer dots for biological fluorescence imaging. ACS Nano. 2008;2:2415-23.

[306] Liu Z, Li X, Tabakman SM, Jiang K, Fan S, Dai H. Multiplexed multicolor Raman imaging of live cells with isotopically modified single walled carbon nanotubes. J Am Chem Soc. 2008;130:13540-1.

[307] Zavaleta CL, Smith BR, Walton I, Doering W, Davis G, Shojaei B, et al. Multiplexed imaging of surface enhanced Raman scattering nanotags in living mice using noninvasive Raman spectroscopy. Proc Natl Acad Sci U S A. 2009;106:13511-6.

[308] Jennings TL, Triulzi RC, Tao G, St Louis ZE, Becker-Catania SG. Simplistic attachment and multispectral imaging with semiconductor nanocrystals. Sensors. 2011;11:10557-70.

[309] Jain RK, Stylianopoulos T. Delivering nanomedicine to solid tumors. Nature reviews Clinical oncology. 2010;7:653-64.

[310] Matsumura Y, Maeda H. A new concept for macromolecular therapeutics in cancer chemotherapy: mechanism of tumoritropic accumulation of proteins and the antitumor agent smancs. Cancer research. 1986;46:6387-92.

[311] Matsumura Y, Kataoka K. Preclinical and clinical studies of anticancer agent-incorporating polymer micelles. Cancer Sci. 2009;100:572-9.

[312] Matsumura Y. Preclinical and clinical studies of NK012, an SN-38-incorporating polymeric micelles, which is designed based on EPR effect. Advanced drug delivery reviews. 2011;63:184-92.

[313] Matsumura Y, Hamaguchi T, Ura T, Muro K, Yamada Y, Shimada Y, et al. Phase I clinical trial and pharmacokinetic evaluation of NK911, a micelle-encapsulated doxorubicin. Br J Cancer. 2004;91:1775-81.

[314] Plummer R, Wilson RH, Calvert H, Boddy AV, Griffin M, Sludden J, et al. A Phase I clinical study of cisplatin-incorporated polymeric micelles (NC-6004) in patients with solid tumours. Br J Cancer. 2011;104:593-8.

[315] Northfelt DW, Dezube BJ, Thommes JA, Miller BJ, Fischl MA, Friedman-Kien A, et al. Pegylated-liposomal doxorubicin versus doxorubicin, bleomycin, and vincristine in the treatment of AIDS-related Kaposi's sarcoma: results of a randomized phase III clinical trial. J Clin Oncol. 1998;16:2445-51.

[316] Gradishar WJ, Tjulandin S, Davidson N, Shaw H, Desai N, Bhar P, et al. Phase III trial of nanoparticle albumin-bound paclitaxel compared with polyethylated castor oil-based paclitaxel in women with breast cancer. J Clin Oncol. 2005;23:7794-803.

[317] Li SD, Huang L. Pharmacokinetics and biodistribution of nanoparticles. Mol Pharm. 2008;5:496-504.

[318] Geng Y, Dalhaimer P, Cai S, Tsai R, Tewari M, Minko T, et al. Shape effects of filaments versus spherical particles in flow and drug delivery. Nat Nanotechnol. 2007;2:249-55.

[319] Levchenko TS, Rammohan R, Lukyanov AN, Whiteman KR, Torchilin VP. Liposome clearance in mice: the effect of a separate and combined presence of surface charge and polymer coating. International journal of pharmaceutics. 2002;240:95-102.

[320] Arnida, Janat-Amsbury MM, Ray A, Peterson CM, Ghandehari H. Geometry and surface characteristics of gold nanoparticles influence their biodistribution and uptake by macrophages. Eur J Pharm Biopharm. 2011;77:417-23.

[321] Yokoi H, Kinoshita T, Zhang S. Dynamic reassembly of peptide RADA16 nanofiber scaffold. Proc Natl Acad Sci U S A. 2005;102:8414-9.

[322] Koutsopoulos S, Unsworth LD, Nagai Y, Zhang S. Controlled release of functional proteins through designer self-assembling peptide nanofiber hydrogel scaffold. Proc Natl Acad Sci U S A. 2009;106:4623-8.

[323] Ramachandran S, Yu YB. Peptide-based viscoelastic matrices for drug delivery and tissue repair. BioDrugs. 2006;20:263-9.

[324] Wu M, Ye Z, Liu Y, Liu B, Zhao X. Release of hydrophobic anticancer drug from a newly designed self-assembling peptide. Mol Biosyst. 2011;7:2040-7.

[325] Kisiday J, Jin M, Kurz B, Hung H, Semino C, Zhang S, et al. Self-assembling peptide hydrogel fosters chondrocyte extracellular matrix production and cell division: implications for cartilage tissue repair. Proc Natl Acad Sci U S A. 2002;99:9996-10001.

[326] Malik R, Qian S, Law B. Design and synthesis of a near-infrared fluorescent nanofiber precursor for detecting cell-secreted urokinase activity. Anal Biochem. 2011;412:26-33.

[327] Lu K, Jacob J, Thiyagarajan P, Conticello VP, Lynn DG. Exploiting amyloid fibril lamination for nanotube self-assembly. J Am Chem Soc. 2003;125:6391-3.

[328] Law B, Tung CH. Structural modification of protease inducible preprogrammed nanofiber precursor. Biomacromolecules. 2008;9:421-5.

[329] Lee JY, Kim JS, An KH, Lee K, Kim DY, Bae DJ, et al. Electrophoretic and dynamic light scattering in evaluating dispersion and size distribution of single-walled carbon nanotubes. J Nanosci Nanotechnol. 2005;5:1045-9.

[330] Cenni E, Granchi D, Avnet S, Fotia C, Salerno M, Micieli D, et al. Biocompatibility of poly(D,L-lactide-co-glycolide) nanoparticles conjugated with alendronate. Biomaterials. 2008;29:1400-11.

[331] Aggarwal P, Dobrovolskaia MA. Gold nanoparticle quantitation via fluorescence in solution and cell culture. Methods Mol Biol. 2011;697:137-43.

[332] Zhang Y, Huo M, Zhou J, Xie S. PKSolver: An add-in program for pharmacokinetic and pharmacodynamic data analysis in Microsoft Excel. Computer methods and programs in biomedicine. 2010;99:306-14.

[333] Zhang S. Fabrication of novel biomaterials through molecular self-assembly. Nat Biotechnol. 2003;21:1171-8.

[334] Xia T, Kovochich M, Brant J, Hotze M, Sempf J, Oberley T, et al. Comparison of the abilities of ambient and manufactured nanoparticles to induce cellular toxicity according to an oxidative stress paradigm. Nano Lett. 2006;6:1794-807.

[335] Frohlich E, Samberger C, Kueznik T, Absenger M, Roblegg E, Zimmer A, et al. Cytotoxicity of nanoparticles independent from oxidative stress. The Journal of toxicological sciences. 2009;34:363-75.

[336] Liu Y, Li W, Lao F, Wang L, Bai R, Zhao Y, et al. Intracellular dynamics of cationic and anionic polystyrene nanoparticles without direct interaction with mitotic spindle and chromosomes. Biomaterials. 2011;32:8291-303.

[337] Crouzier T, Nimmagadda A, Nollert MU, McFetridge PS. Modification of single walled carbon nanotube surface chemistry to improve aqueous solubility and enhance cellular interactions. Langmuir. 2008;24:13173-81.

[338] Radomski A, Jurasz P, Alonso-Escolano D, Drews M, Morandi M, Malinski T, et al. Nanoparticle-induced platelet aggregation and vascular thrombosis. Br J Pharmacol. 2005;146:882-93.

[339] Geys J, Nemmar A, Verbeken E, Smolders E, Ratoi M, Hoylaerts MF, et al. Acute toxicity and prothrombotic effects of quantum dots: impact of surface charge. Environ Health Perspect. 2008;116:1607-13.

[340] Rybak-Smith MJ, Sim RB. Complement activation by carbon nanotubes. Advanced drug delivery reviews. 2011;63:1031-41.

[341] Meng F, Engbers GH, Gessner A, Muller RH, Feijen J. Pegylated polystyrene particles as a model system for artificial cells. Journal of biomedical materials research Part A. 2004;70:97-106.

[342] Walkey CD, Olsen JB, Guo H, Emili A, Chan WC. A Combination of Nanoparticle Size and Surface Chemistry Determines Serum Protein Adsorption and Macrophage Uptake. J Am Chem Soc. 2011.

[343] Lunov O, Syrovets T, Loos C, Beil J, Delacher M, Tron K, et al. Differential uptake of functionalized polystyrene nanoparticles by human macrophages and a monocytic cell line. ACS Nano. 2011;5:1657-69.

[344] Zahr AS, Davis CA, Pishko MV. Macrophage uptake of core-shell nanoparticles surface modified with poly(ethylene glycol). Langmuir. 2006;22:8178-85.

[345] Riley T, Stolnik S, Heald CR, Xiong CD, Garnett MC, Illum L, et al. Physicochemical Evaluation of Nanoparticles Assembled from Poly(lactic acid)−Poly(ethylene glycol) (PLA−PEG) Block Copolymers as Drug Delivery Vehicles. Langmuir. 2001;17:3168-74.

[346] Verma A, Stellacci F. Effect of surface properties on nanoparticle-cell interactions. Small. 2010;6:12-21.

[347] Ruggiero A, Villa CH, Bander E, Rey DA, Bergkvist M, Batt CA, et al. Paradoxical glomerular filtration of carbon nanotubes. Proc Natl Acad Sci U S A. 2010;107:12369-74.

[348] Cabral H, Matsumoto Y, Mizuno K, Chen Q, Murakami M, Kimura M, et al. Accumulation of sub-100 nm polymeric micelles in poorly permeable tumours depends on size. Nat Nanotechnol 2011;6:815-23.

[349] Weissleder R, Pittet MJ. Imaging in the era of molecular oncology. Nature. 2008;452:580-9.

[350] Farokhzad OC, Langer R. Impact of nanotechnology on drug delivery. ACS Nano. 2009;3:16-20.

COPYRIGHT LICENSES

RightsLink®

Home | Account Info | Help

Logged in as:
Anil Wagh
LOGOUT

Title: Development of Biocompatible Polymeric Nanoparticles for in Vivo NIR and FRET Imaging

Author: Anil Wagh, Steven Y. Qian, and Benedict Law

Publication: Bioconjugate Chemistry

Publisher: American Chemical Society

Date: May 1, 2012

Copyright © 2012, American Chemical Society

PERMISSION/LICENSE IS GRANTED FOR YOUR ORDER AT NO CHARGE

This type of permission/license, instead of the standard Terms & Conditions, is sent to you because no fee is being charged for your order. Please note the following:

- Permission is granted for your request in both print and electronic formats, and translations.
- If figures and/or tables were requested, they may be adapted or used in part.
- Please print this page for your records and send a copy of it to your publisher/graduate school.
- Appropriate credit for the requested material should be given as follows: "Reprinted (adapted) with permission from (COMPLETE REFERENCE CITATION). Copyright (YEAR) American Chemical Society." Insert appropriate information in place of the capitalized words.
- One-time permission is granted only for the use specified in your request. No additional uses are granted (such as derivative works or other editions). For any other uses, please submit a new request.

BACK | CLOSE WINDOW

Copyright © 2013 Copyright Clearance Center, Inc. All Rights Reserved. Privacy statement.
Comments? We would like to hear from you. E-mail us at customercare@copyright.com

ELSEVIER LICENSE
TERMS AND CONDITIONS

Dec 11, 2013

This is a License Agreement between Anil Wagh ("You") and Elsevier ("Elsevier") provided by Copyright Clearance Center ("CCC"). The license consists of your order details, the terms and conditions provided by Elsevier, and the payment terms and conditions.

All payments must be made in full to CCC. For payment instructions, please see information listed at the bottom of this form.

Supplier	Elsevier Limited The Boulevard,Langford Lane Kidlington,Oxford,OX5 1GB,UK
Registered Company Number	1982084
Customer name	Anil Wagh
Customer address	2608 Kenzie Terrace Apt 217 MINNEAPOLIS, MN 55418
License number	3285970685755
License date	Dec 11, 2013
Licensed content publisher	Elsevier
Licensed content publication	Nanomedicine: Nanotechnology, Biology and Medicine
Licensed content title	A short circulating peptide nanofiber as a carrier for tumoral delivery
Licensed content author	Anil Wagh,Jagdish Singh,Steven Qian,Benedict Law
Licensed content date	May 2013
Licensed content volume number	9
Licensed content issue number	4
Number of pages	9
Start Page	449
End Page	457
Type of Use	reuse in a thesis/dissertation
Portion	full article
Format	both print and electronic
Are you the author of this Elsevier article?	Yes
Will you be translating?	No
Title of your thesis/dissertation	DESIGN AND EVALUATION OF POLYMERIC NANOMATERIALS FOR IN VITRO AND IN VIVO IMAGING APPLICATIONS
Expected completion date	Feb 2014
Estimated size (number of pages)	210
Elsevier VAT number	GB 494 6272 12

JOHN WILEY AND SONS LICENSE TERMS AND CONDITIONS

Dec 11, 2013

This is a License Agreement between Anil Wagh ("You") and John Wiley and Sons ("John Wiley and Sons") provided by Copyright Clearance Center ("CCC"). The license consists of your order details, the terms and conditions provided by John Wiley and Sons, and the payment terms and conditions.

All payments must be made in full to CCC. For payment instructions, please see information listed at the bottom of this form.

License Number	3285970476755
License date	Dec 11, 2013
Licensed content publisher	John Wiley and Sons
Licensed content publication	Small
Licensed content title	Polymeric Nanoparticles with Sequential and Multiple FRET Cascade Mechanisms for Multicolor and Multiplexed Imaging
Licensed copyright line	Copyright © 2013 WILEY-VCH Verlag GmbH & Co. KGaA, Weinheim
Licensed content author	Anil Wagh,Faidat Jyoti,Sanku Mallik,Steven Qian,Estelle Leclerc,Benedict Law
Licensed content date	Jan 29, 2013
Start page	2129
End page	2139
Type of use	Dissertation/Thesis
Requestor type	Author of this Wiley article
Format	Print and electronic
Portion	Full article
Will you be translating?	No
Total	**0.00 USD**
Terms and Conditions	

TERMS AND CONDITIONS

This copyrighted material is owned by or exclusively licensed to John Wiley & Sons, Inc. or one of its group companies (each a "Wiley Company") or a society for whom a Wiley Company has exclusive publishing rights in relation to a particular journal (collectively "WILEY"). By clicking "accept" in connection with completing this licensing transaction, you agree that the following terms and conditions apply to this transaction (along with the billing and payment terms and conditions established by the Copyright Clearance Center Inc., ("CCC's Billing and Payment terms and conditions"), at the time that you opened your RightsLink account (these are available at any time at http://myaccount.copyright.com).

Terms and Conditions

1. The materials you have requested permission to reproduce (the "Materials") are protected by copyright.
2.You are hereby granted a personal, non-exclusive, non-sublicensable, non-transferable, worldwide, limited license to reproduce the Materials for the purpose specified in the licensing process. This license is for a one-time use only with a maximum distribution equal to the number that you identified in the licensing process. Any form of republication granted by this license must be completed within two years of the date of the grant of this license (although copies prepared before may be distributed thereafter). The Materials shall not be used in any other manner or for any other purpose. Permission is granted subject to an appropriate acknowledgement given to the author, title of the material/book/journal and the publisher. You shall also duplicate the copyright notice that appears in the Wiley publication in your use of the